

1

2 Analysis report on the  $ep \rightarrow e' p' \pi^+ \pi^-$  reaction in the CLAS  
3 detector with a 2.039 GeV beam for  $0.4 \text{ GeV}^2 < Q^2 < 1.0 \text{ GeV}^2$   
4 and  $1.3 \text{ GeV} < W < 1.825 \text{ GeV}$

5 **G. Fedotov<sup>a,b</sup>, V. Burkert<sup>c</sup>, R. Gothe<sup>b</sup>, V. Mokeev<sup>a,c</sup>, Iu. Skorodumina<sup>a,b</sup>**

6 <sup>a</sup>*Moscow State University,  
7 Vorob'evy gory, 119899 Moscow, Russia*

8 <sup>b</sup>*University of South Carolina,  
9 712 Main Street, Columbia, South Carolina, 29208*

10 <sup>c</sup>*Thomas Jefferson National Accelerator Facility,  
11 12000 Jefferson Avenue, Newport News, Virginia, 23606*

# <sup>12</sup> Contents

<sup>13</sup> 1	Physics motivation	<sup>4</sup>
<sup>14</sup> 2	Event selection	<sup>8</sup>
<sup>15</sup> 2.1	Particles identification . . . . .	<sup>9</sup>
<sup>16</sup> 2.1.1	Electron identification . . . . .	<sup>9</sup>
<sup>17</sup> 2.1.2	Hadron identification . . . . .	<sup>16</sup>
<sup>18</sup> 2.1.3	Timing correction . . . . .	<sup>17</sup>
<sup>19</sup> 2.2	Momentum corrections . . . . .	<sup>22</sup>
<sup>20</sup> 2.2.1	Electron momentum correction . . . . .	<sup>22</sup>
<sup>21</sup> 2.2.2	Proton momentum correction (Energy loss) . . . . .	<sup>23</sup>
<sup>22</sup> 3	Other cuts and corrections	<sup>26</sup>
<sup>23</sup> 3.1	Fiducial cuts . . . . .	<sup>26</sup>
<sup>24</sup> 3.1.1	Fiducial cuts for negatively charged particles . . . . .	<sup>26</sup>
<sup>25</sup> 3.1.2	Fiducial cuts for positively charged particles . . . . .	<sup>27</sup>
<sup>26</sup> 3.2	Data quality check . . . . .	<sup>29</sup>
<sup>27</sup> 3.3	Vertex cut . . . . .	<sup>31</sup>
<sup>28</sup> 3.4	Exclusivity cut . . . . .	<sup>35</sup>
<sup>29</sup> 3.5	Missing energy cut . . . . .	<sup>39</sup>
<sup>30</sup> 3.6	Binning and kinematical coverage . . . . .	<sup>39</sup>
<sup>31</sup> 4	Cross section calculation	<sup>42</sup>
<sup>32</sup> 4.1	Kinematical variables . . . . .	<sup>42</sup>

33	4.2	Cross section formula . . . . .	49
34	4.3	Radiative corrections . . . . .	52
35	4.4	Efficiency evaluation . . . . .	53
36	4.5	Filling kinematical cells with zero acceptance . . . . .	55
37	4.6	Combination of various topologies . . . . .	58
38	<b>5</b>	<b>Correction for binning effects</b>	<b>60</b>
39	<b>6</b>	<b>Systematical errors</b>	<b>63</b>
40	6.1	Errors due to normalization, electron identification, and electron detection efficiency . . . . .	63
41	6.2	Errors due to the different ways of combining topologies . . . . .	64
42	6.3	Errors due to the integration over different final hadron variables . . . . .	64
43	6.4	Systematical error summary . . . . .	65
44	<b>7</b>	<b>Conclusions</b>	<b>67</b>
45	<b>Appendix A: Measured cross sections</b>		<b>69</b>
46	<b>Bibliography</b>		<b>118</b>

<sup>48</sup> **Chapter 1**

<sup>49</sup> **Physics motivation**

<sup>50</sup> In this analysis note new set of differential and fully integrated cross sections for the exclusive  
<sup>51</sup> reaction  $ep \rightarrow e'p'\pi^+\pi^-$  from data of the e1e run collected with the CLAS detector in  
<sup>52</sup> the kinematic area of  $1.3 \text{ GeV} < W < 1.825 \text{ GeV}$  and  $0.4 \text{ GeV}^2 < Q^2 < 1.0 \text{ GeV}^2$  is  
<sup>53</sup> presented. In each bin of  $W$  and  $Q^2$  nine single-differential cross sections are obtained.  
<sup>54</sup> They consist of: a) three distributions over invariant masses of the final hadron pairs; b)  
<sup>55</sup> three CM-angular distributions over polar angles  $\theta$  of the final  $\pi^+$ ,  $\pi^-$ , and  $p'$ , and c) three  
<sup>56</sup> CM-angular distributions over the angles  $\alpha$  between two planes. One plain is defined by  
<sup>57</sup> the three-momenta of all final hadrons. Another plane is defined by the three-momenta  
<sup>58</sup> of virtual photon and one of the final hadrons for the three different choices of this final  
<sup>59</sup> hadron. More detailed information about kinematical variables is in Sect. 4.1. These data  
<sup>60</sup> were obtained for the first time in the kinematic area  $Q^2 < 0.6 \text{ GeV}^2$  and  $W > 1.55 \text{ GeV}$ .  
<sup>61</sup> At  $0.6 \text{ GeV}^2 < Q^2 < 1.0 \text{ GeV}^2$  similar  $\pi^+\pi^-p$  single-differential cross sections have already  
<sup>62</sup> been measured with CLAS [1]. However, in this data set these cross sections are obtained  
<sup>63</sup> in  $Q^2$ -bins of bin sizes, which are roughly a factor of six smaller than those achieved in [1].

<sup>64</sup> The studies of exclusive  $\pi^+\pi^-$  electroproduction off protons represent an important avenue  
<sup>65</sup> in the investigation of the  $N^*$  spectrum and structure via analyses of experimental data  
<sup>66</sup> on exclusive meson electroproduction with CLAS. The CLAS detector has provided the dominant  
<sup>67</sup> portion of all data on meson electroproduction in the resonance excitation region. The  
<sup>68</sup> studies of transition helicity amplitudes from the proton ground state to its excited states  
<sup>69</sup> represent a key aspect of the  $N^*$  program with CLAS [2, 3]. Data on meson electroproduction  
<sup>70</sup> off nucleons in the  $N^*$  region obtained with CLAS open an opportunity to determine  
<sup>71</sup> the  $Q^2$  evolution of the  $\gamma_v N \rightarrow N^*$  electrocouplings both in comparative and combined  
<sup>72</sup> analyses of various meson electroproduction channels. The electroexcitation amplitudes for  
<sup>73</sup> the low-lying resonances  $\Delta(1232)3/2^+$ ,  $N(1440)1/2^+$ ,  $N(1520)3/2^-$ , and  $N(1535)1/2^-$  have  
<sup>74</sup> been determined over a wide range of  $Q^2$  in a comprehensive analysis of JLab-CLAS data  
<sup>75</sup> on differential cross sections, longitudinally polarized beam asymmetries, and beam-target  
<sup>76</sup> asymmetries for single pion electroproduction off protons [4]. Recently  $\gamma_v N \rightarrow N^*$  elec-

77 electrocouplings of several higher-lying nucleon resonances:  $N(1675)5/2^-$ ,  $N(1680)5/2^+$ , and  
 78  $N(1710)1/2^+$  have become available for the first time for  $1.5 \text{ GeV}^2 < Q^2 < 4.5 \text{ GeV}^2$  from  
 79 the analysis of exclusive  $\pi^+$  electroproduction off the proton [5]. Electrocouplings for the  
 80  $N(1440)1/2^+$  and  $N(1520)3/2^-$  resonances for  $Q^2 < 0.6 \text{ GeV}^2$  have been determined from  
 81 the data [6] on exclusive  $\pi^+\pi^-$  electroproduction off the proton [7]. The recent analysis [8] of  
 82 the CLAS data on  $\pi^+\pi^-$  electroproduction off protons [1] provided the results on electrocou-  
 83 plings of these states in a wider  $Q^2$ -range up to  $1.5 \text{ GeV}^2$ . Furthermore, electrocouplings of  
 84 the  $\Delta(1620)3/2^-$  resonance that decays preferentially to the  $N\pi\pi$  final states have become  
 85 available from this analysis for the first time. Consistent results for the  $\gamma_vp \rightarrow N^*$  elec-  
 86 trocouplings of the  $N(1440)1/2^+$  and  $N(1520)3/2^-$  resonances, that have been determined  
 87 in independent analyses of the dominant meson electroproduction channels  $N\pi$  and  $\pi^+\pi^-p$   
 88 with completely different non-resonant contributions, demonstrated the reliable extraction  
 89 of these fundamental quantities. This success also supports the capability of the reaction  
 90 models, that have been developed for the extraction of the resonance parameters from the  
 91 analyses of data on single- [4] and double-pion [9] electroproduction off protons, to provide  
 92 reliable information on the  $N^*$  parameters from independent studies of either of these major  
 93 exclusive channels.

94 The CLAS results on the  $\gamma_vp \rightarrow N^*$  electrocouplings [2, 4, 5, 7, 8, 10] have had a stimulat-  
 95 ing impact on the theory of the excited nucleon state structure, in particular, on QCD-based  
 96 approaches. The light cone sum rule (LCSR) approach [11, 12] for the first time provided  
 97 access to the quark distribution amplitudes (DAs) inside the  $N(1535)1/2^-$  resonance from  
 98 analysis of the CLAS results on the  $\gamma_vp \rightarrow N^*$  electrocouplings of this state [4]. Confronting  
 99 the quark DAs of excited nucleon states determined from the experimental results on the  
 100  $\gamma_vp \rightarrow N^*$  electrocouplings to the LQCD expectations, makes it possible to explore the  
 101 emergence of the resonance structure starting from the QCD Lagrangian. The moments of  
 102 the  $N(1535)1/2^-$  quark DAs derived from the CLAS data are consistent with the LQCD  
 103 expectations [12]. The Dyson-Schwinger Equations of QCD (DSEQCD) provide a concep-  
 104 tually different avenue for relating the  $\gamma_vp \rightarrow N^*$  electrocouplings to the fundamental QCD  
 105 Lagrangian [13–15]. The DSEQCD approach allows to evaluate the contribution of the three  
 106 bound dressed quarks, the so-called quark core, to the structure of excited nucleon states  
 107 starting from the QCD Lagrangian. A successful description of the nucleon elastic form  
 108 factors and the CLAS results on the  $N \rightarrow \Delta$ ,  $N \rightarrow N(1440)1/2^+$  electromagnetic transition  
 109 form factors [2, 4, 7, 10] at photon virtualities  $Q^2 > 2.0 \text{ GeV}^2$  has been recently achieved  
 110 within the DSEQCD framework [13, 15, 16]. This successful description of the form factors  
 111 that correspond to distinctively different structures achieved with the same dressed quark  
 112 mass function strongly underlines:

- 113 • the relevance of dynamical dressed quarks with the properties predicted by the DSE-  
 114 QCD approach [17] as constituents of the quark cores for the structure of the ground  
 115 and excited nucleon states;
- 116 • the capability of the DSEQCD approach [13, 15] to map out the dressed quark mass

117 function from the experimental results on the  $Q^2$  evolution of the nucleon elastic and  
118  $p \rightarrow N^*$  transition form factors ( $\gamma_v p \rightarrow N^*$  electrocouplings) from a combined analysis.

119 Physics analyses of the CLAS results [4, 7, 10] on the  $\gamma_v p \rightarrow N^*$  electrocouplings revealed  
120 the structure of excited nucleon states at photon virtualities  $Q^2 < 5.0$  GeV $^2$  as a complex  
121 interplay between meson-baryon and quark degrees of freedom. The relative contributions  
122 from the meson-baryon cloud and the quark core are strongly dependent on the quantum  
123 numbers of the excited nucleons. Analyses of the  $A_{1/2}$  electrocouplings of the  $N(1520)3/2^-$   
124 resonance [18, 19] demonstrated that this amplitude is dominated by quark core contributions  
125 in the entire range of  $Q^2 < 5.0$  GeV $^2$  measured by CLAS. However, the recent analysis [20]  
126 of the first CLAS results [5] on the  $N(1675)5/2^-$   $\gamma_v p \rightarrow N^*$  electrocouplings suggested a  
127 dominance of the meson-baryon cloud. Pronounce differences in the structure of the  $N^*$  states  
128 of different quantum numbers demonstrate different manifestations of the non-perturbative  
129 strong interaction in generation of excited nucleons as the bound systems of an infinite  
130 amount of quarks and gluons. The studies of  $\gamma_v p \rightarrow N^*$  electrocouplings for all prominent  
131 nucleon resonances offer unique information on many facets of the non-perturbative strong  
132 interaction and motivate the extension of the studies of  $\gamma_v p \rightarrow N^*$  electrocouplings over full  
133 spectrum of excited nucleons.

134 Currently the results on resonance electrocouplings in mass range above 1.6 GeV are  
135 rather limited. The recent studies of single pion electroproduction [5] delivered the results on  
136 electrocouplings of only those high mass states, which have a substantial branching fraction  
137 for decays to the  $N\pi$  final states. Several high-lying nucleon excitations, as  $\Delta(1620)1/2^-$ ,  
138  $\Delta(1700)3/2^-$ , and  $N(1720)3/2^+$ , decay preferentially to  $N\pi\pi$  final states making the channel  
139 of  $\pi^+\pi^-$  electroproduction off the proton the major source of information on electrocouplings  
140 of these states. In the future these electrocouplings can be checked in independent analyses  
141 of  $KY$  exclusive electroproduction channels [21]. The data on electrocouplings of high-lying  
142 resonances, which decay both to the  $N\pi$  and the  $N\pi\pi$  final states, in  $\pi^+\pi^-$  electroproduction  
143 channel will make it possible to test the consistency of these results with those from inde-  
144 pendent analyses of single pion electroproduction, offering a sensitive check of the reliability  
145 of the resonance parameter extraction.

146 The experimental data on  $\pi^+\pi^-$  electroproduction off protons presented in this analysis  
147 note will be analyzed within the framework of the meson-baryon reaction model JM [7–  
148 9], which is currently the only available approach worldwide for the extraction of resonance  
149 electrocouplings from this exclusive channel. The aforementioned approach already provided  
150 reliable results on electrocouplings of all resonances in mass range below 1.65 GeV with  
151 sizable decays to the  $N\pi\pi$  final states. The analysis of experimental data presented in this  
152 note eventually will allow us to:

- 153 • determine the evolution of the electrocouplings of most nucleon resonances in mass  
154 range up to 1.825 GeV with photon virtualities  $Q^2$  up to 1.0 GeV $^2$  with bin sizes in  $Q^2$   
155 much smaller than previously achieved in any experiments. For high-lying resonances

156       that decay preferentially to the  $N\pi\pi$  final states this information will be obtained for  
157       the first time;

- 158       • explore electrocouplings of all orbital excitations ( $L=1$ ) of the  $[70,1^-]$  spin-flavor  $SU(6)$ -  
159       supermultiplet in a combined analysis of the results from both  $N\pi$  and  $N\pi\pi$  channels.

160       Studies of the combined CLAS preliminary results on  $\pi^+\pi^-$  photo- and electroproduction  
161       [1] within the framework of the JM meson-baryon reaction model have provided further  
162       convincing evidences for the existence of the new baryon state  $N'(1720)3/2^+$  [22]. So far,  
163       it is the only candidate state, for which information on the internal structure has become  
164       available from results on  $\gamma_vp \rightarrow N^*$  electrocouplings at  $Q^2 < 1.5$  GeV $^2$ . However, right now,  
165       only four data points for this new state's electrocouplings are available. From the data of  
166       this analysis note, the  $N'(1720)3/2^+$  electrocoupling values will become available at the set  
167       of additional  $Q^2$  bins of bin size at least a factor of six smaller than available from the old  
168       CLAS experiment [1]. The expected results will for the first time offer a deep insight to the  
169       structure of the new baryon state  $N'(1720)3/2^+$ .

170       The expected results will extend considerably the available information on the interplay  
171       between meson-baryon cloud and quark core contributions to the structure of excited nucleon  
172       states in particular in mass range from 1.6 to 1.8 GeV.

<sup>173</sup> **Chapter 2**

<sup>174</sup> **Event selection**

<sup>175</sup> The data reported in this analysis were taken during the e1e run periods in the Hall B during  
<sup>176</sup> November 2002 - January 2003 that included several configurations (hydrogen and deuterium  
<sup>177</sup> targets as well as two different beam energies of 1 GeV and 2.039 GeV). The torus current  
<sup>178</sup> was 2250 A and the mini torus current 5995 A. This particular analysis is concentrated on  
<sup>179</sup> the data obtained with the 2 cm long liquid hydrogen target located at -0.2 cm along z-axis,  
<sup>180</sup> a 2.039 GeV polarized electron beam, and the CLAS detector. The run numbers' range of  
<sup>181</sup> this experimental setup is 36118 - 36512. There is a gap in the run numbering between runs  
<sup>182</sup> 36160 and 36387, which coincides with Christmas and New Year of 2002-2003 and is most  
<sup>183</sup> likely connected to a database server glitch (there are no entries in the database nor files  
<sup>184</sup> on the silo associated with run numbers in this gap). Totally about 1.5 billion triggers over  
<sup>185</sup> a month of a beamtime were accumulated. The list of full and empty target runs that are  
<sup>186</sup> used in the analysis is presented in Tab. 2.1.

Full target runs	Empty target runs
36117–36122, 36125–36129, 36133–36142	35124
36144, 36145, 36147–36150, 36152–36154	36428
36156, 36158–36160, 36429–36434	36495
36437, 36441–36447, 36449, 36450	
36452–36454, 36458–36467, 36469	
36473–36478, 36480–36482, 36484–36492	
36497–36503, 36505–36511	

Table 2.1: List of the runs that are used in the analysis.

## <sup>187</sup> 2.1 Particles identification

<sup>188</sup> In this analysis the first in time particle that gives signals in all four parts of the CLAS  
<sup>189</sup> detector is chosen as electron candidate for each event. To identify hadrons only signals in  
<sup>190</sup> drift chambers and time-of-flight system are required.

<sup>191</sup> All data accumulated during the run is stored in BOS [23] files. For all events selected  
<sup>192</sup> for analysis the number of geometrically reconstructed particles (*gpart*) was required to be  
<sup>193</sup> greater than zero. The *gpart* variable is extracted from variable *NPGP* in HEVT bank  
<sup>194</sup> according to 2.1.1.

$$NPGP = (\text{Number of final reconstructed particles}) \times 100 + gpart \quad (2.1.1)$$

<sup>195</sup> One more requirement is that the status word (*stat*) is greater than zero (variable *Status*  
<sup>196</sup> in EVNT bank).

<sup>197</sup> Then, as mentioned above, for electron candidates signals in all four detectors are required  
<sup>198</sup> (all variables *DCStat*, *CCStat*, *SCStat*, *ECStat* from EVNT bank must be greater than  
<sup>199</sup> zero). For hadrons only the variables *DCStat* and *SCStat* from EVNT bank are required  
<sup>200</sup> to be greater than zero.

<sup>201</sup> Finally the corresponding charge for all particle candidates (variable *Charge* from EVNT  
<sup>202</sup> bank) is required to be plus or minus one depending on the particle candidate's type.

### <sup>203</sup> 2.1.1 Electron identification

<sup>204</sup> Firstly electromagnetic calorimeter (EC) and Čerenkov counter (CC) responses need to be  
<sup>205</sup> checked, to select good electrons from the electron candidates.

#### <sup>206</sup> EC cuts

<sup>207</sup> On the hardware level the calorimeter threshold was set to cut off events as close as possible  
<sup>208</sup> to the kinematic edges of the  $W$  and  $Q^2$  domain covered by the measurement, but far enough  
<sup>209</sup> to keep the low energy contamination within reasonable limits. To select good electrons more  
<sup>210</sup> precisely an additional calorimeter threshold cut on the software level is applied. This cut  
<sup>211</sup> accounts for the minimal momentum of the scattered electron that can be reconstructed  
<sup>212</sup> ( $P_{e'} > 0.461$  GeV) and is chosen according to [24].

<sup>213</sup> Then an additional cut (the so-called sampling fraction cut) was applied to eliminate in  
<sup>214</sup> part pion contamination. To develop this cut the fact that electrons and pions have differ-  
<sup>215</sup> ent energy deposition patterns in EC was used. An electron produces an electromagnetic  
<sup>216</sup> shower, where the deposited energy is proportional to the electron momentum, while a  $\pi^-$

as minimum ionizing particle loses a constant amount of energy per scintillator (2 MeV/cm) independently of its momentum. In Fig. 2.1 total energy deposited in EC divided by the particle momentum is shown as function of particle momentum. The six plots represent six CLAS sectors. Events between the red curves are selected as good electron candidates for further analysis. The vertical red line at  $P_{e'} = 0.461$  GeV shows EC threshold cut. The upper and lower red curves are obtained in the following way: x-slices of 2D histograms are fit by Gaussians. In this way points that correspond to the positions of the fit maxima  $\pm 3\sigma$  are obtained. These points determine the upper and lower boundaries for the cut. Finally, to obtain smooth curves, all points are fit by a second order polynom.

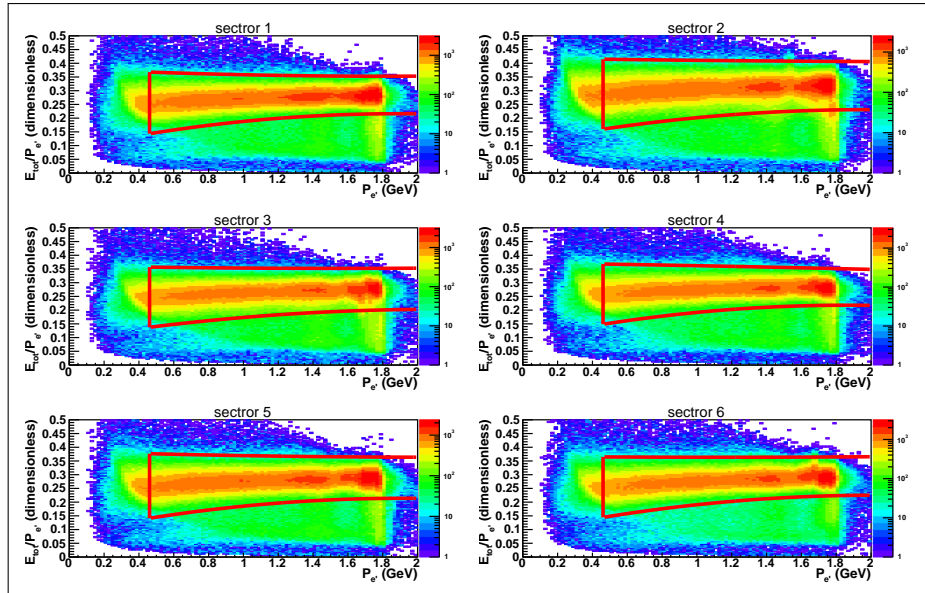


Figure 2.1: Sampling fraction distributions for the data. Six plots correspond to six CLAS sectors. Events between red curves are selected for further analysis.

Both cuts on minimal electron energy and on sampling fraction are applied both to experimental and Monte Carlo events. Since the Monte Carlo simulation does not reproduce electromagnetic showers good enough, the sampling fraction cuts for the simulation, obtained using the same procedure as for the data, look slightly different (see Fig. 2.2).

In Fig. 2.3 the energy deposited in the outer part of EC versus the energy deposited in the inner part of EC is shown before (left plot) and after (right plot) final electron identification. As it is seen in this plot the spot in the left bottom corner that corresponds to the pion contamination disappears that verifies the reliability of the electron selection.

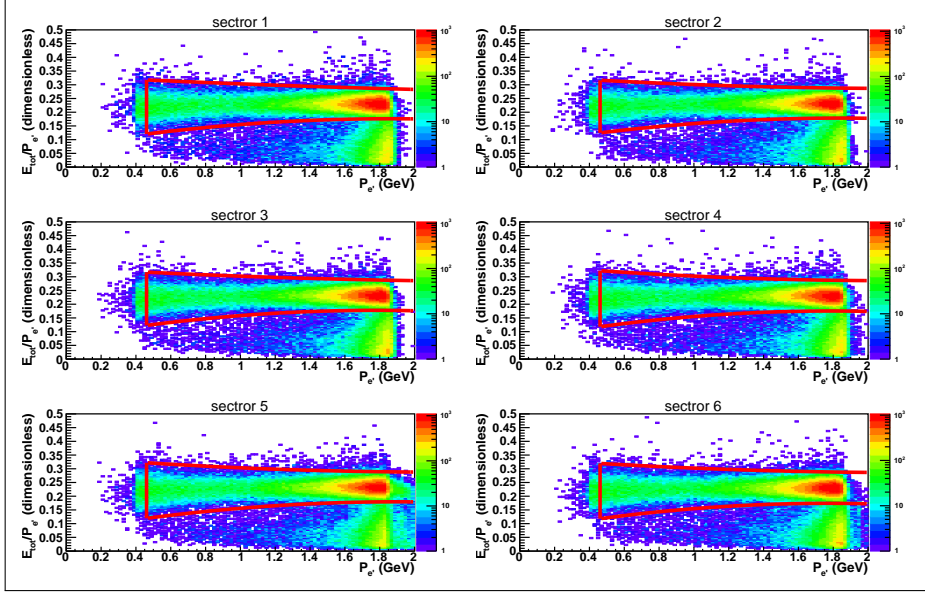


Figure 2.2: Sampling fraction distributions for Monte Carlo. Six plots correspond to six CLAS sectors. Events between red curves are selected for further analysis.

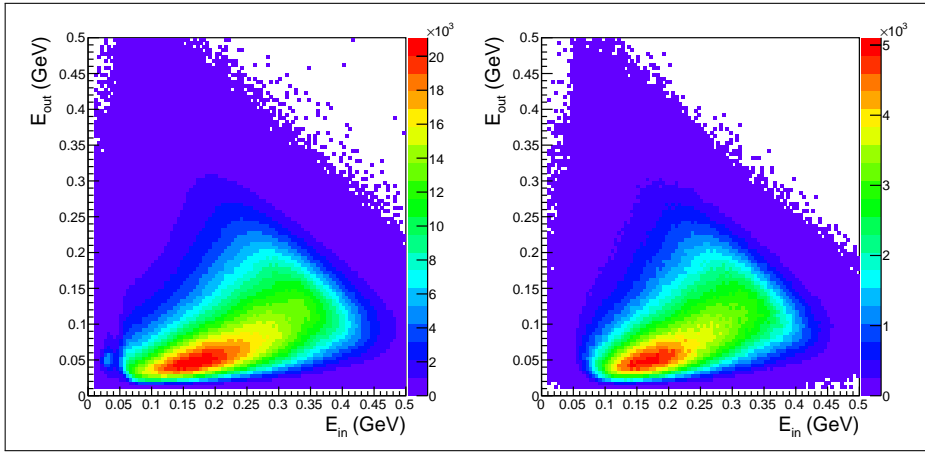


Figure 2.3: Energy deposited in the outer part of EC versus energy deposited in the inner part of EC before (left plot) and after (right plot) final electron selection.

<sup>234</sup> **CC cuts**

<sup>235</sup> To improve the quality of electron candidate selection and  $\pi^-/e^-$  separation a Čerenkov  
<sup>236</sup> counter is used. In this experiment the Čerenkov counter had inhomogeneously distributed  
<sup>237</sup> zones with partially low detection efficiency. For that purpose a geometrical cut for the  
<sup>238</sup> removal of CC low efficiency zones is established. This cut is defined in the plane of Čerenkov  
<sup>239</sup> counter. Since polar and azimuthal angles ( $\theta_{cc}, \varphi_{cc}$ ) in the CC plane are not directly defined  
<sup>240</sup> in the BOS banks [23] some calculations were made to derive these angles from variables  
<sup>241</sup> available in DCPB bank. Fig. 2.4 illustrates these calculations.

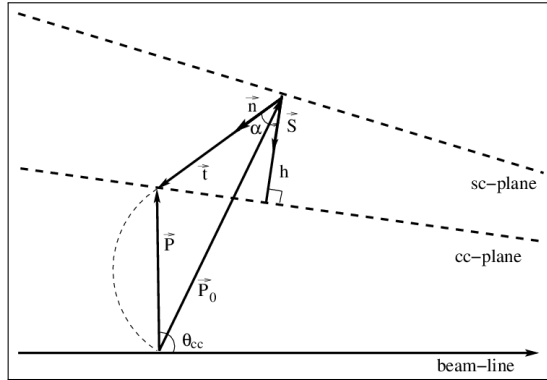


Figure 2.4: Calculation of polar  $\theta_{cc}$  and azimuthal  $\varphi_{cc}$  angles in the CC plane using variables that are available in DCPB bank.

<sup>242</sup> The equation 2.1.2 of the CC plane is known from [25]:

$$\begin{aligned}
 Ax + By + Cz + D &= 0, \\
 D &= 1., \\
 A &= -0.000785, \\
 B &= 0, \\
 C &= -0.00168, \\
 \vec{S} &= (A, B, C)
 \end{aligned} \tag{2.1.2}$$

<sup>243</sup> The distance ( $h$ ) from the SC hit point to the CC plane (see Fig. 2.4) is then given by

$$h = \frac{(\vec{S} \cdot \vec{P}_0) + D}{|\vec{S}|}, \tag{2.1.3}$$

<sup>244</sup> where components of  $\vec{P}_0$  are available in DCPB bank ( $x_{sc}, y_{sc}, z_{sc}$ ). A tangent to the  
<sup>245</sup> particle track at the point of intersection with the CC plane ( $\vec{t}$ ) is shown in Fig. 2.4 by a

<sup>246</sup> dashed line and can be written as

$$|\vec{t}| = \frac{h}{\cos(\alpha)}. \quad (2.1.4)$$

<sup>247</sup> In turn  $\cos(\alpha)$  can be calculated as 2.1.5.

$$\cos(\alpha) = \frac{(\vec{n} \cdot \vec{S})}{|\vec{S}|}, \quad (2.1.5)$$

<sup>248</sup> where  $\vec{n}$  is a unit vector in  $\vec{t}$ -direction based on the DCPB bank variables ( $cx\_sc, cy\_sc, cz\_sc$ ).  
<sup>249</sup> It needs to be mentioned that there is no magnetic field between the CC and SC planes, so  
<sup>250</sup> after hitting the CC plane the particle moves along the  $\vec{t}$ -vector.

<sup>251</sup> It is easy to see from Fig. 2.4 that the vector  $\vec{P}$ , which goes from the interaction vertex  
<sup>252</sup> to the track intersection with the CC plane, is  $\vec{P} = \vec{P}_0 + \vec{t}$ . Therefore, the angles  $\theta_{cc}$  and  
<sup>253</sup>  $\varphi_{cc}$  can be calculated by 2.1.6 and 2.1.7, respectively.

$$\theta_{cc} = \arccos \left( \frac{P_z}{|\vec{P}|} \right) \quad (2.1.6)$$

$$\begin{aligned} \varphi_{cc} &= \arctan \left( \frac{P_y}{P_x} \right) & \text{if } P_x > 0, P_y > 0 \\ \varphi_{cc} &= \arctan \left( \frac{P_y}{P_x} \right) + 2\pi & \text{if } P_x > 0, P_y < 0 \\ \varphi_{cc} &= \arctan \left( \frac{P_y}{P_x} \right) + \pi & \text{if } P_x < 0, P_y < 0 \\ \varphi_{cc} &= \arctan \left( \frac{P_y}{P_x} \right) + \pi & \text{if } P_x < 0, P_y > 0 \\ \varphi_{cc} &= \frac{\pi}{2} & \text{if } P_x = 0, P_y > 0 \\ \varphi_{cc} &= \frac{3\pi}{2} & \text{if } P_x = 0, P_y < 0 \end{aligned} \quad (2.1.7)$$

<sup>254</sup> After the angles in the CC plane are defined, distributions  $\varphi_{cc}$  vs.  $\theta_{cc}$  are plotted for each  
<sup>255</sup> CLAS sector (see Fig. 2.5). The quantity 2.1.8 is shown by the color code in Fig. 2.5. This  
<sup>256</sup> quantity varies from zero to one and shows the portion of good electrons with number of  
<sup>257</sup> photoelectrons greater than five inside a  $(\theta_{cc}, \varphi_{cc})$  bin. Or in other words how efficient CC  
<sup>258</sup> is in a given  $(\theta_{cc}, \varphi_{cc})$  bin.

$$\frac{\text{number of events inside } (\theta_{cc}, \varphi_{cc}) \text{ bin with more than 5 photoelectrons in CC}}{\text{total number of events inside } (\theta_{cc}, \varphi_{cc}) \text{ bin}} \quad (2.1.8)$$

259 The edges of the distributions in Fig. 2.5 are sharp due to the fiducial cut that is applied  
 260 in the CC plane 2.1.9. The shape of this cut is taken from [26].

$$\begin{aligned} \theta_{cc} &> 7.0 + 0.0032\varphi_{cc} + 0.0499\varphi_{cc}^2 \\ \left(\frac{\theta_{cc} - 45.5^\circ}{34.5^\circ}\right)^2 + \left(\frac{\varphi_{cc}}{21^\circ}\right)^2 &\leq 1 \\ \left(\frac{\theta_{cc} - 45.5^\circ}{1.75^\circ}\right)^2 + \left(\frac{\varphi_{cc}}{21^\circ}\right)^2 &> 1 \\ \theta_{cc} &< 45^\circ \end{aligned} \quad (2.1.9)$$

261 The two stripes in sector five in Fig. 2.5 correspond to the inefficient zones that will be  
 262 discussed in Sec. 3.1.

263 For further analysis only zones with a ratio 2.1.8 greater than 0.8 are selected. These  
 264 zones are shown in black in Fig. 2.6. As it is seen in Fig. 2.6, there is an inefficient zone in  
 265 the middle of each sector, that is expected since two CC mirrors are joined there.

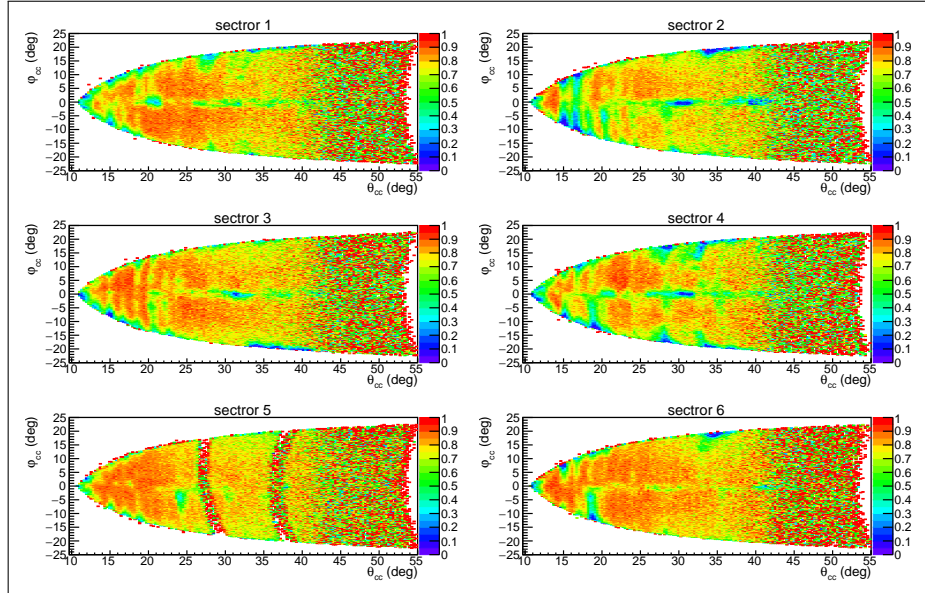


Figure 2.5: Distributions of the quantity 2.1.8 as function of the polar ( $\theta_{cc}$ ) and azimuthal ( $\varphi_{cc}$ ) angles in the CC plane for six CLAS sectors.

266 After the geometrical cut shown in Fig. 2.6 is applied photoelectron distributions are  
 267 plotted for each PMT on the left and right sides of each CC segment and for each CLAS  
 268 sector (see Fig. 2.7). The segment number and *index* that indicates which side PMT was  
 269 fired are taken from the CCPB bank *Status* variable according to

$$Status = 10 \times (\text{CC segment number}) + 1000 \times (1 + index), \quad (2.1.10)$$

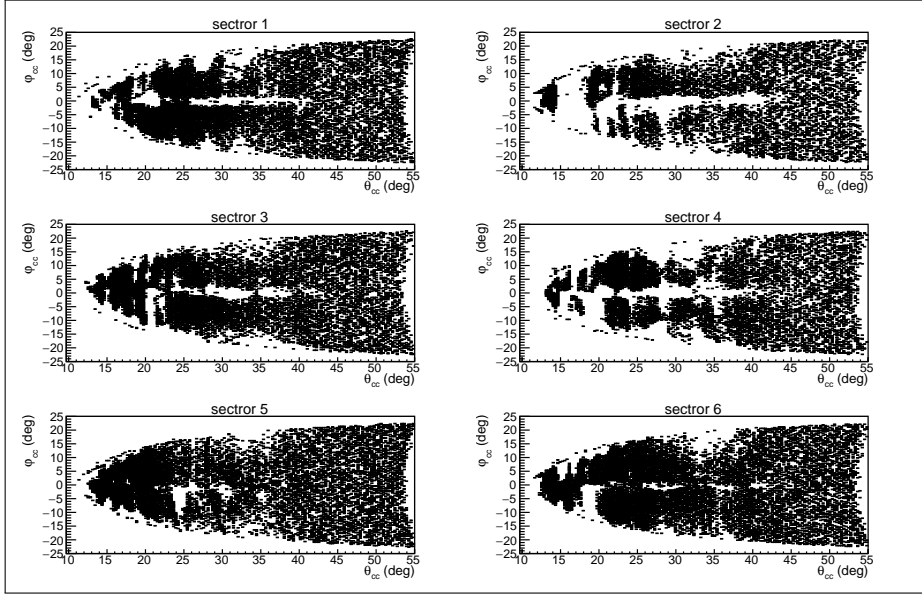


Figure 2.6: Zones where CC is efficient enough to accept good electron candidates are shown in black as function of the polar ( $\theta_{cc}$ ) and azimuthal ( $\varphi_{cc}$ ) angles in the CC plane for six CLAS sectors.

270 where *index* is 1 for right PMTs, -1 for left PMTs, and 0 for the case when both PMTs were  
271 fired.

272 As it is seen in Fig. 2.7, there are some peaks at low number of photoelectrons. These  
273 peaks correspond to  $\pi^-$  contamination and/or noise in PMTs [25]. To eliminate events under  
274 this peak all events on the left side of the red vertical line in Fig. 2.7 are excluded from the  
275 analysis.

276 Since Monte Carlo does not reproduce photoelectron distributions well enough, the cut  
277 shown by the red line in Fig. 2.7 is applied only to the data. To recover good electrons that  
278 were cut off in this way a special procedure is developed. The part of the distributions on  
279 the right side of the red line is fit by function 2.1.11, which is a slightly modified Poisson  
280 distribution.

$$y = P_1 \left( \frac{P_3^{\frac{x}{P_2}}}{\Gamma \left( \frac{x}{P_2} + 1 \right)} \right) e^{-P_3} \quad (2.1.11)$$

281 The fitting function is then continued into the region on the left side of the red line. In  
282 this way the two regions, shown by blue and green in Fig. 2.7, are determined. Finally the  
283 correction factors are defined by 2.1.12 and applied as a weight for each event which goes to  
284 the particular PMT.

$$F_{ph. el.} = \frac{\text{green area} + \text{blue area}}{\text{green area}} \quad (2.1.12)$$

285 It needs to be mentioned that segments one, two, and 18 are removed from the analysis  
 286 completely since they are dominated by events with very low number of photoelectrons. The  
 287 procedure described above is applied for left and right side PMTs. For the events with both  
 288 PMTs fired the peak at low number of photoelectrons is almost absent and no additional  
 289 cut like this is needed.

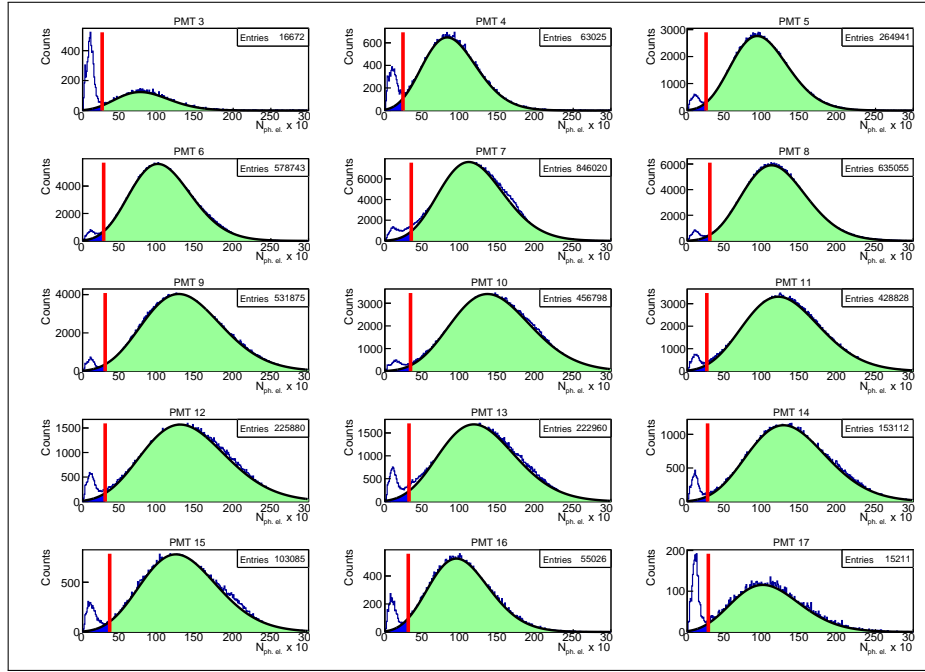


Figure 2.7: Number of photoelectrons multiplied by ten for the left side of sector one of CC. Various plots correspond to various CC segments. Black curves show the fit by function 2.1.11. Red vertical lines show the applied cut. Regions that are needed to calculate the ratio 2.1.12 are shown in blue and green.

## 290 2.1.2 Hadron identification

291 The CLAS time-of-flight (TOF) system provides information on particle velocity ( $\beta = v/c$ ).  
 292 The information from the Drift Chambers allows to measure the particle momentum ( $P$ ).  
 293 Therefore, charged hadron can be identified using the relation between particle mass, mo-  
 mentum, and velocity

$$\beta = \frac{p}{\sqrt{p^2 + m^2}}. \quad (2.1.13)$$

295 For the hadron identification, only events with electron candidates that have been selected  
 296 in the previous step are used.  $\beta$  versus momentum distributions are plotted for each TOF

297 scintillator in each CLAS sector (see example plots for CLAS sector one in Fig. 2.8 for  
 298 positively charged particles and in Fig. 2.9 for preliminary selected  $\pi^-$  candidates).

299 It needs to be mentioned that in order to simplify the analysis process the preliminary  
 300 particle id was made on an initial step of converting data from the BOS files to the files with  
 301 ROOT trees. It leads to the fact that in Figure 2.9 only the region that corresponds to the  
 302 preliminary selected  $\pi^-$  candidates is filled with events.

303 For visual identification of improperly working scintillation bars, theoretical curves with  
 304 hadron 2.1.13 ( $\pi^+$ ,  $\pi^-$ , proton) proper mass assumptions are plotted. As it can be seen in the  
 305 plots paddle number 48 has enormous number of events. It happened most likely, because  
 306 more paddles of TOF were connected to TDC 48 or due to cooking problems. Therefore,  
 307 paddles 48 are excluded from the analysis. Besides scintillators number 17 in sectors two  
 308 and five worked improperly and are also excluded from the analysis.

309 Events between purple dashed curves in Fig. 2.8 and Fig. 2.9 are selected as  $\pi^+$  and  $\pi^-$   
 310 candidates, respectively. Analytical formulae for these curves are given in 2.1.14.

$$\begin{aligned} \beta &< \frac{(205.98 - P_{hadron}) \left( \frac{200 - P_{hadron}}{200 + P_{hadron}} \right)^{0.7} (P_{hadron} + 0.5)}{(200.02 + P_{hadron}) \sqrt{(P_{hadron} + 0.5)^2 + 0.019}} + 0.019 \\ \beta &> \frac{(1 + 5 \times 1.07 \times (P_{hadron} - 0.07))(P_{hadron} - 0.07)}{(1 + 5(P_{hadron} - 0.07)) \sqrt{(P_{hadron} - 0.07)^2 + 0.138^2}} - 0.1 \end{aligned} \quad (2.1.14)$$

311 For proton candidates the selection cuts 2.1.15 are used. They are shown by the red  
 312 dashed lines in Fig. 2.8.

$$\begin{aligned} \beta &< \left( \frac{P_{hadron}}{\sqrt{P_{hadron}^2 + 0.938^2}} + 0.02 \right) \frac{1.2 + 0.92P_{hadron}}{1 + P_{hadron}} \\ \beta &> \left( \frac{P_{hadron}}{\sqrt{P_{hadron}^2 + 0.938^2}} - 0.05 \right) \frac{1 + P_{hadron}}{0.9 + 1.06P_{hadron}} \end{aligned} \quad (2.1.15)$$

313 As seen in Figs. 2.8 and 2.9 some scintillators with numbers larger equal 40 have two  
 314 bands (both of them most likely correspond to the given hadron). The origin of these two  
 315 bands can be based on mistakes in data cooking/calibration or the consequence of the fact  
 316 that two scintillation bars are connected to one TDC. For this large-number scintillators all  
 317 events laying higher than the upper cut for protons are assumed to be pions.

### 318 2.1.3 Timing correction

319 Another approach can be used to treat the scintillators with numbers larger equal 40, which  
 320 have two bands that correspond to the same hadron. The idea of this approach is to plot

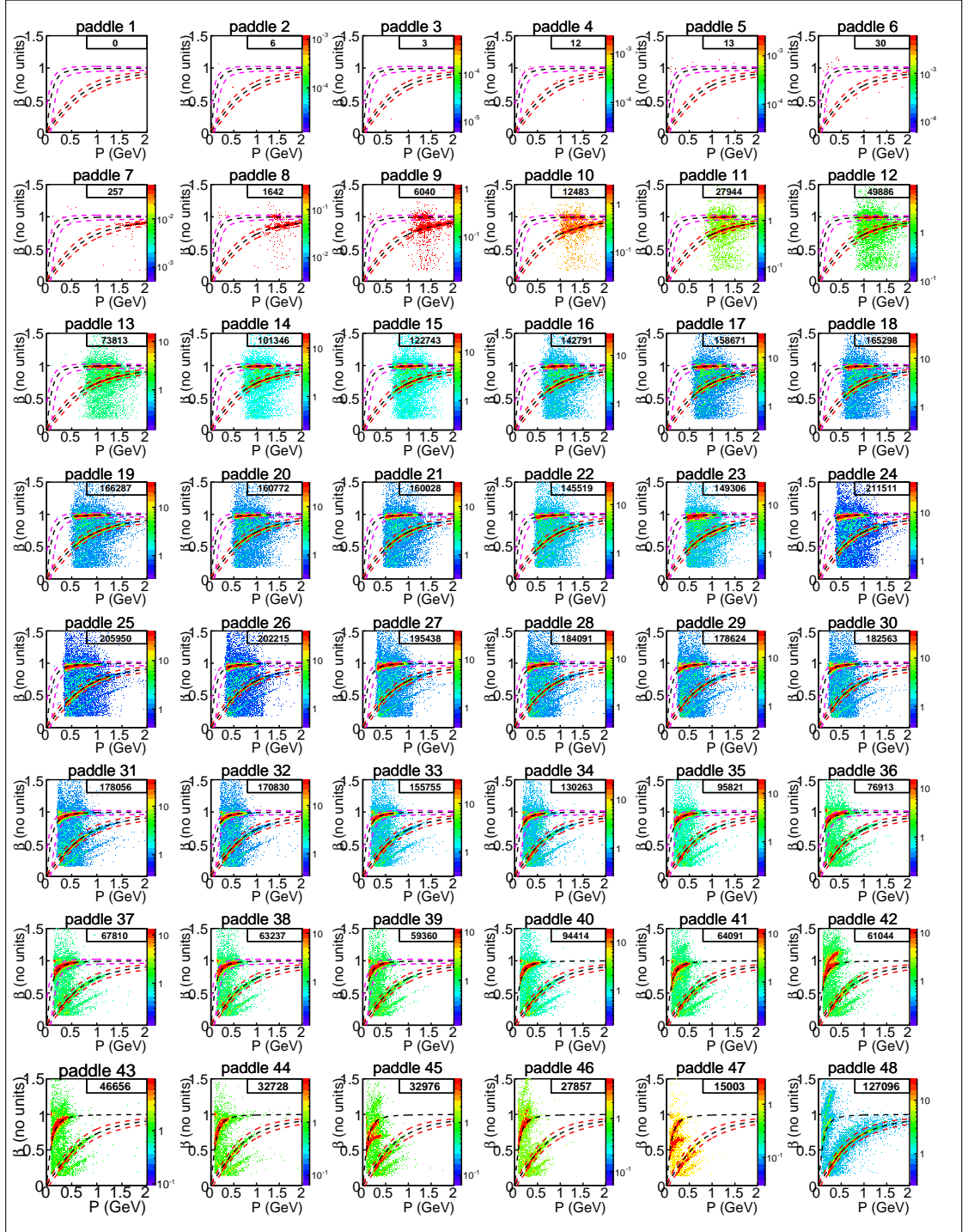


Figure 2.8:  $\beta$  versus momentum distributions for positively charged particles for different TOF scintillators in CLAS sector one. Black dashed curves are theoretical under the exact hadron mass assumption 2.1.13. Events between the two purple dashed 2.1.14 and two red dashed 2.1.15 curves are selected as  $\pi^+$  and proton candidates, respectively. For scintillators with number greater equal 40 all events laying higher than the upper red dashed curve are assumed as  $\pi^+$  candidates. Number of events is shown in the right upper corner of each plot.

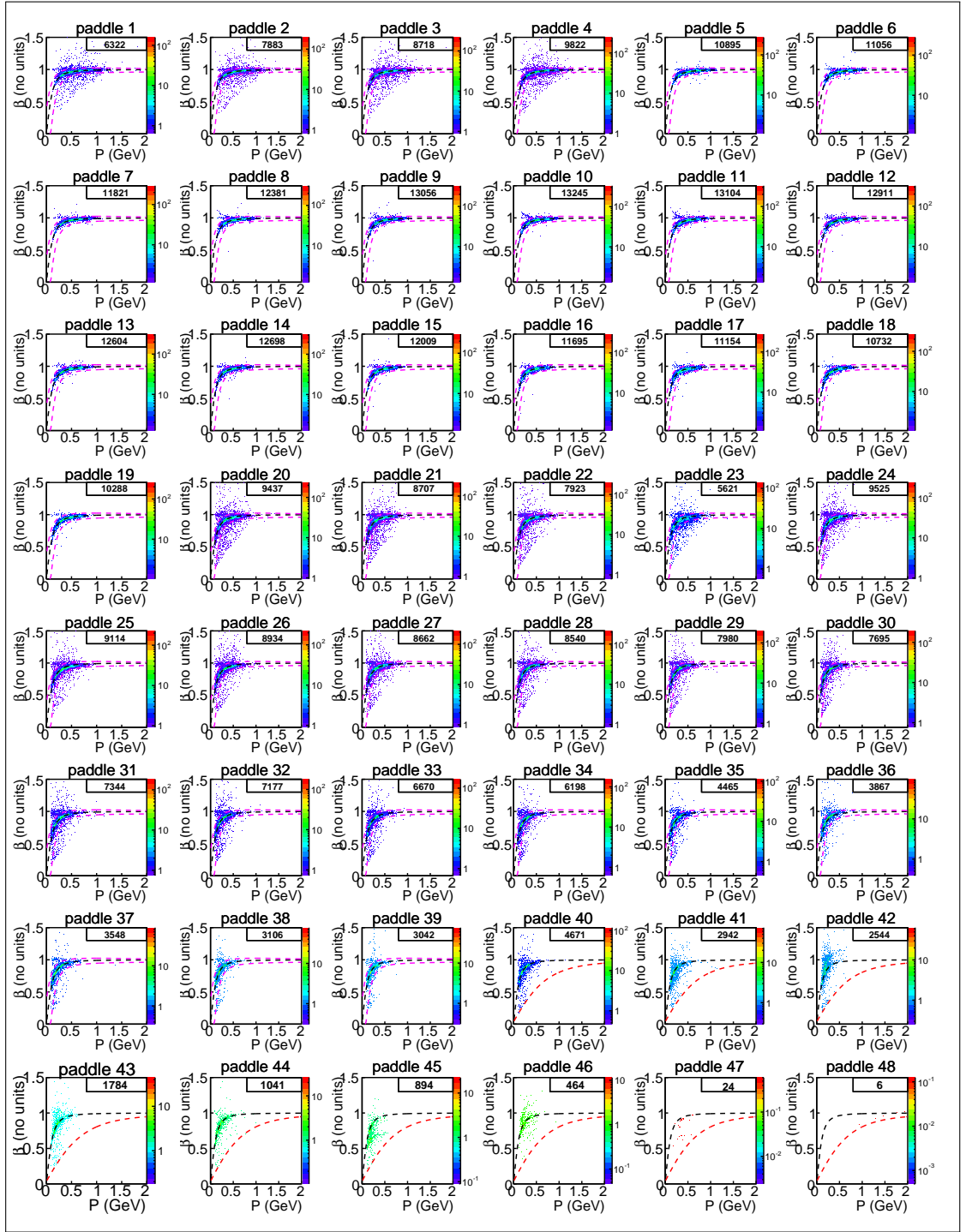


Figure 2.9:  $\beta$  versus momentum distributions for negatively charged particles for different TOF scintillators in CLAS sector one. Black dashed curves are theoretical under the exact  $\pi^-$  mass assumption 2.1.13. Events between the two purple dashed 2.1.14 curves are selected as  $\pi^-$  candidates. For scintillators with number greater equal 40 all events laying higher than the red dashed curve are assumed as  $\pi^-$  candidates. Number of events is shown in the right upper corner of each plot.

321 the difference between the measured time that hadron travels between the target and the  
 322 SC plane and the same quantity calculated under the exact hadron mass assumption. This  
 323 time difference  $\Delta T$  is calculated as:

$$\Delta T = \frac{l_h}{c} \left( \frac{1}{\beta_n} - \frac{1}{\beta_{old}} \right), \quad (2.1.16)$$

324 where  $l_h$  is the hadron path length from the vertex to the SC plane (the *Path* variable in  
 325 DCPB bank),  $\beta_n$  is the nominal  $\beta$  with the exact mass of the hadron assumed (see Eq. 2.1.13),  
 326  $\beta_{old}$  is the value of  $\beta$  that needs to be corrected,  $c$  is the speed of light.

327 In the left side in Fig. 2.10  $\Delta T$  is plotted for the  $\pi^+$  candidates for the paddle 42 in  
 328 CLAS sector one as a function of their momentum. The two horizontal bands are clearly  
 329 seen in this figure. One of them is around  $\Delta T = 0$ , while another one is shifted by two nano  
 330 seconds and corresponds to the wrong band in  $\beta$  versus momentum distribution for paddle  
 331 42 (see Fig. 2.8).

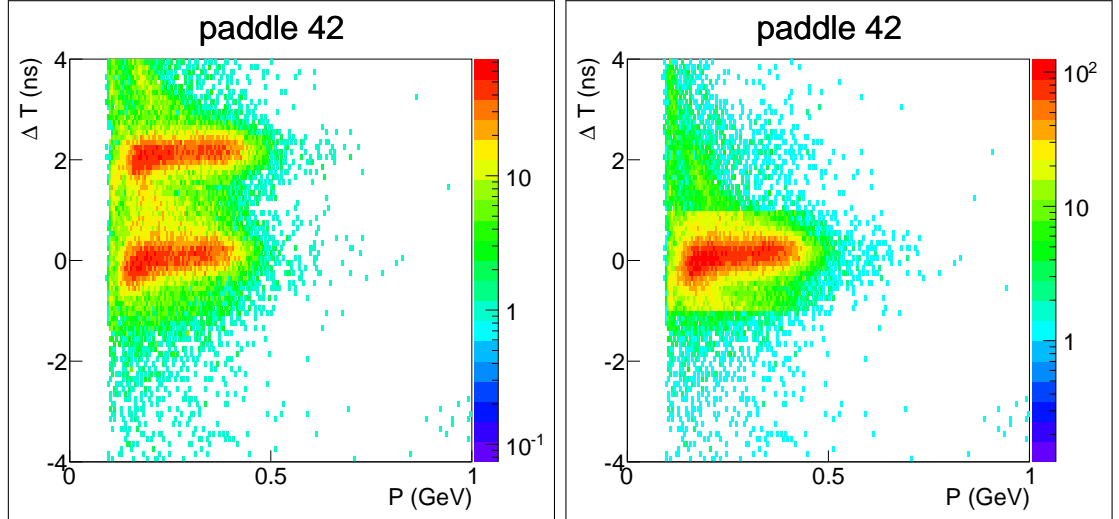


Figure 2.10: Quantity  $\Delta T$  that is given by Eq. 2.1.16 before (left plot) and after (right plot) the timing corrections.

322 The idea of timing corrections is to shift the wrong bands in  $\Delta T$  versus momentum  
 323 distributions to their correct position around  $\Delta T = 0$ . The result of this shift is shown in  
 324 the right side in Fig. 2.10. After this shift the correct value of  $\beta$  is calculated using Eq. 2.1.17.

$$\beta_{corr} = \frac{1}{\frac{1}{\beta_n} - \frac{(\Delta T - t_{max})c}{l_h}}, \quad (2.1.17)$$

335 where  $t_{max}$  is the position of each wrong band, 2 ns in the example shown in Fig. 2.10.

After applying the procedure that is described above for all pion candidates in all problematic paddles with double bands, the  $\beta$  versus momentum distributions are plotted, see Fig. 2.11. As it is seen in Fig. 2.11 there are no paddles with double bands anymore. So, even for scintillators with the numbers greater equal 40 the same  $\beta$  versus momentum cuts (see Eq. 2.1.14) can be applied. This procedure is performed for pion candidates only, since the effect of the band doubling in the  $\beta$  versus momentum distributions for the protons is rather small and all proton candidates are lying inside the cut given by Eq. 2.1.15 even without timing corrections.

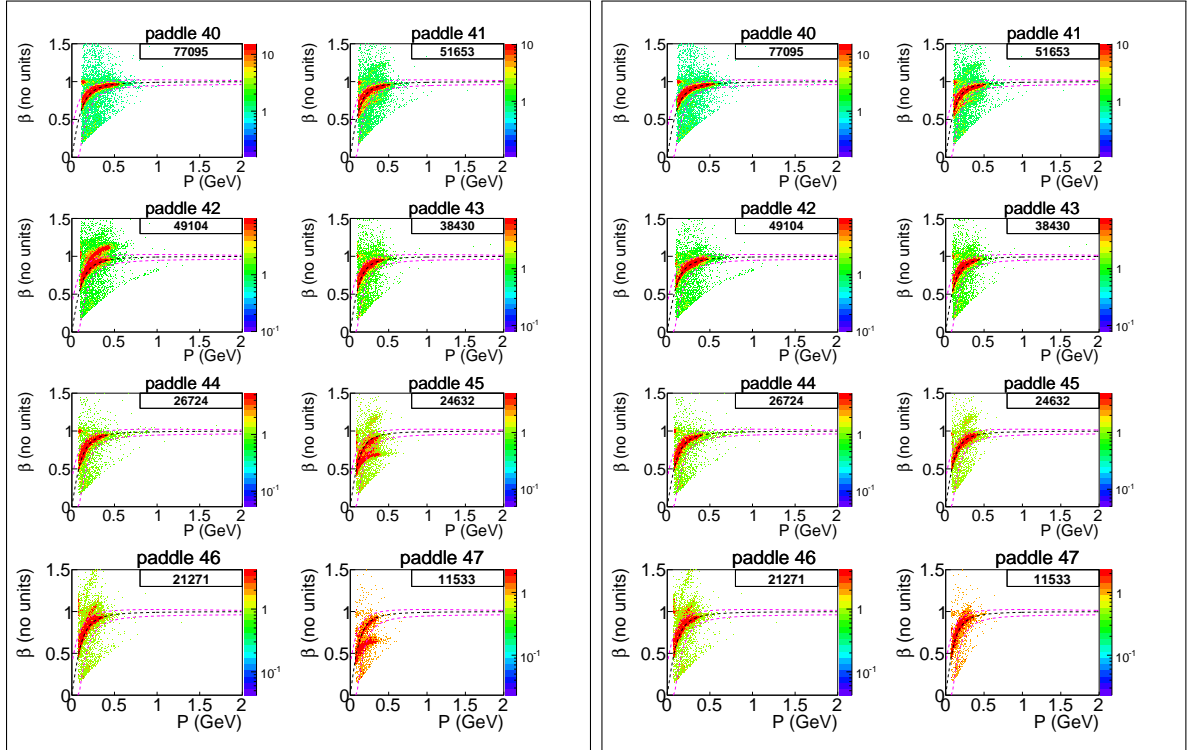


Figure 2.11:  $\beta$  versus momentum distributions before (left plot) and after (right plot) the timing corrections for  $\pi^+$ . Only scintillators in CLAS sector one with number larger than 40 are shown. Black dashed curves are theoretical under the exact  $\pi^+$  mass assumption 2.1.13. Events between the two purple dashed 2.1.14 and two red dashed 2.1.15 curves are selected as pions. Number of events is shown in the right upper corner of each plot.

Both methods of hadrons identification that are described in the previous and this sections have been compared and it is found that they give pretty small difference in the cross sections. Nevertheless, the final cross sections presented in this analysis are obtained using the timing corrections described in this section.

## 348 2.2 Momentum corrections

### 349 2.2.1 Electron momentum correction

350 Due to the slight misalignments in the DC position, small inaccuracies in the description of  
 351 the torus magnetic field, and other possible reasons the momentum and angle of particles  
 352 may have some small systematic deviations from the real values. Since the effects are of  
 353 unknown origin, they cannot be simulated in GSIM. Hence a special momentum correction  
 354 procedure is needed for the data. The approach [27], which is based on elastic kinematic,  
 355 was chosen for this purpose.

356 Low beam energy  $\sim 2$  GeV of analyzed dataset leads to the small shift ( $\sim 3$  MeV) in  
 357 elastic peak position. For comparison for 6 GeV runs this shift is about 20 MeV. From [27]  
 358 it is known that momentum corrections are essential only for high-energetic particles. Since  
 359 in  $2\pi$  kinematics hadrons carry only small portion of the system momentum, the expected  
 360 momentum corrections for them are significantly less than for electrons and can be neglected.

361 In Fig. 2.12 elastic peak positions are shown for six CLAS sectors before (left panel)  
 362 and after (right panel) electron momentum correction. The peaks are fit by Gaussians with  
 363 polynomial background, fitting curves are shown in Fig. 2.12, and the fit parameter  $p_1$   
 364 corresponds to the elastic peak position. As seen in Fig. 2.13, elastic peak positions for all  
 365 CLAS sectors get closer to the proton mass, shown by red horizontal line. The momentum  
 366 resolution for electrons can be roughly estimated from elastic peak width that is about nine  
 367 MeV.

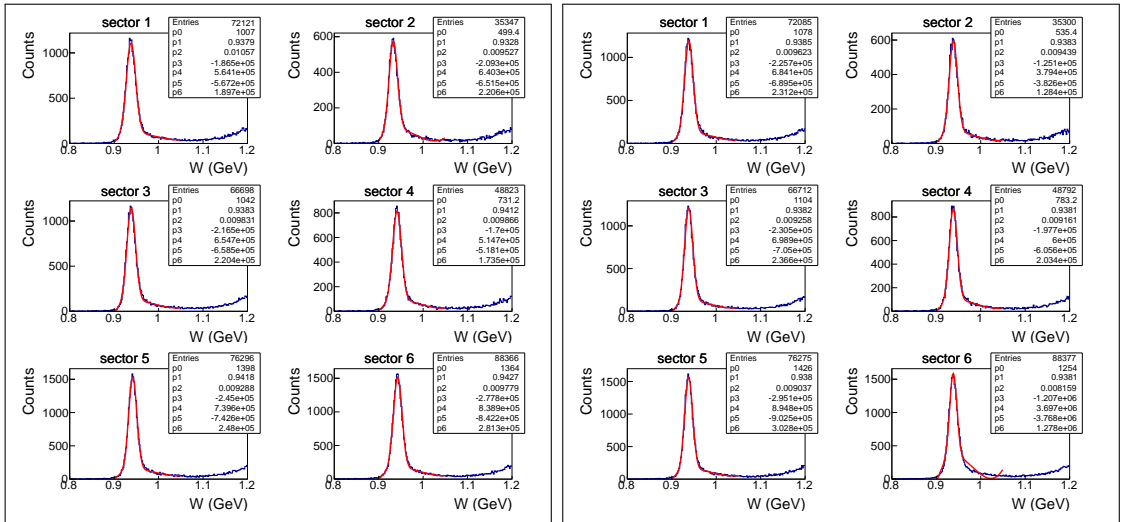


Figure 2.12: Elastic peaks for six CLAS sectors before (left panel) and after (right panel) electron momentum correction. Fit parameter  $p_1$  corresponds to elastic peak position.

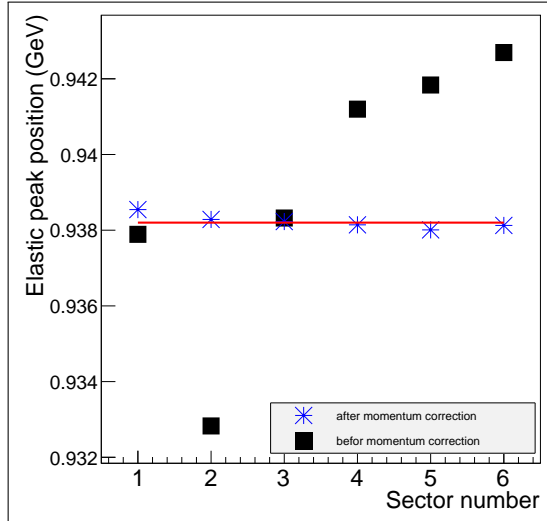


Figure 2.13: Elastic peak position for six CLAS sectors before (black squares) and after (blue stars) electron momentum correction. Horizontal red line shows the proton mass.

368 Due to unknown reasons (most likely because electrons lose energy when they travel  
 369 through the detector and target media) the reconstructed electron momentum appears to  
 370 be slightly lower than the generated one. Therefore, an adapted electron momentum correc-  
 371 tion procedure is also applied to the Monte Carlo events. This correction depends only on  
 372 scattered electron angle  $\theta$  and momentum, but not on the CLAS sector. Figure 2.14 shows  
 373 differences between thrown and reconstructed electron momenta before and after the correc-  
 374 tion procedure. As shown in Fig. 2.14, these differences become negligible after momentum  
 375 corrections have been applied.

### 376 2.2.2 Proton momentum correction (Energy loss)

377 While traveling through the detector and the target, the proton loses part of its energy due  
 378 to interaction with media, hence the measured momentum is lower than the one the proton  
 379 actually had right after the interaction. This effect is especially important for the low-  
 380 energy protons and can lead to misdetermination of various kinematical quantities. GSIM  
 381 simulation of the CLAS detector correctly propagates protons through the media and is used  
 382 to account for this effect by using both information about the generated and reconstructed  
 383 protons.

384 To obtain the correction function, event distributions for the differences between gener-  
 385 ated and reconstructed proton momenta are binned in proton momentum and proton angle  
 386  $\theta$  and fit by Gaussians. The in this way obtained peak positions are fit as function of proton  
 387 momentum and proton angle  $\theta$ . The results are shown in Fig. 2.15. The function shown in

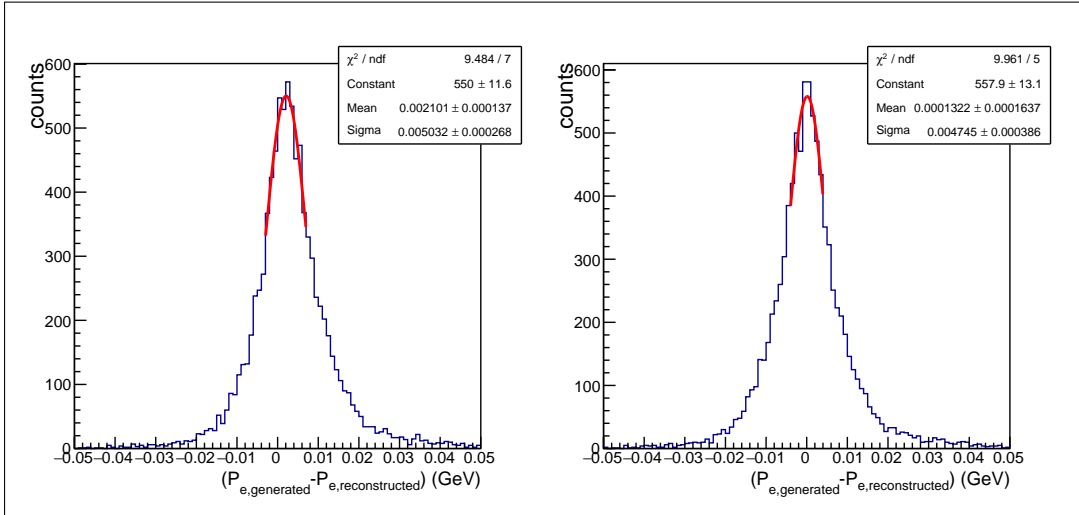


Figure 2.14: The difference between generated and reconstructed electron momenta before (left plot) and after (right plot) the momentum correction has been applied to the reconstructed electrons.

388 Fig. 2.15 gives the percentage of the momentum that protons lose when they move through  
 389 the detector and target media. This function is used to correct the momentum both in the  
 390 simulation and the data.

391 It needs to be mentioned that to isolate the pure effect of energy loss, reconstructed  
 392 events with and without detector and target material need to be compared. Since in the  
 393 used procedure differences between generated and reconstructed events are analyzed, the  
 394 correction function shown in Fig. 2.15 can also include other effects that lead to improper  
 395 proton momentum reconstruction.

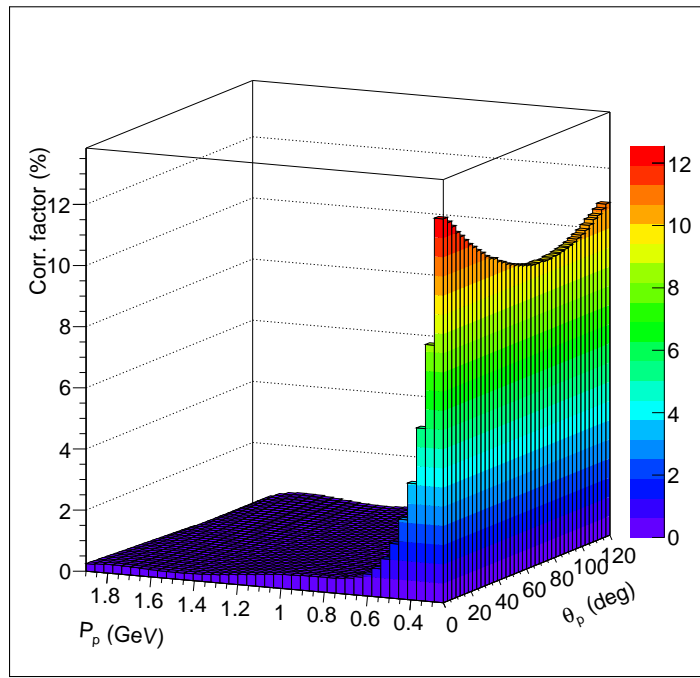


Figure 2.15: The percentage of momentum that protons lose when they move through the detector and target media as a function of the momentum and scattered angle  $\theta$  of the proton.

<sup>396</sup> **Chapter 3**

<sup>397</sup> **Other cuts and corrections**

<sup>398</sup> **3.1 Fiducial cuts**

<sup>399</sup> The CLAS detector has an active detection solid angle that is obviously smaller than  $4\pi$ .  
<sup>400</sup> This is in part due to the space filled with the torus field coils: the angles covered by the coils  
<sup>401</sup> are not equipped with any detection system and therefore form a "dead" area for detection.  
<sup>402</sup> Moreover, different studies and analyses have shown that also the edges of the active area  
<sup>403</sup> do not provide a safe region for particle reconstruction, being affected by rescattering from  
<sup>404</sup> the coil, field distortions, and similar effects. Therefore it is now common practice to accept  
<sup>405</sup> for the analysis only events inside specific fiducial cuts, i.e. cuts on the kinematic variables  
<sup>406</sup> (momentum and angles) of each particle. This method guarantees that the reconstructed  
<sup>407</sup> events accepted in the analysis include only particles detected in "safe" areas of the detector,  
<sup>408</sup> that is where the acceptance is thought to be well understood. These cuts are applied for  
<sup>409</sup> both real events and Monte Carlo reconstructed events and produce a reduction factor in  
<sup>410</sup> the number of events accepted in each kinematic bin that is called detector acceptance.

<sup>411</sup> **3.1.1 Fiducial cuts for negatively charged particles**

<sup>412</sup> In the CLAS experiments with the normal direction of the torus magnetic field, like in e1e  
<sup>413</sup> experiment, negatively charged particles are inbending. For that type of particles sector  
<sup>414</sup> independent, symmetrical, and momentum dependent cuts are applied. To establish the  
<sup>415</sup> shape of these cuts relatively flat areas in  $\varphi$  distributions are selected. For that purpose all  
<sup>416</sup> events are binned in the particle momentum and the particle polar angle  $\theta$  (see Fig. 3.1).  
<sup>417</sup> In Fig. 3.1  $\varphi$  distributions are shown for one slice over momentum and for various bins in  
<sup>418</sup>  $\theta$  for electrons (left side plots) and  $\pi^-$  (right side plots). Events between the vertical lines  
<sup>419</sup> in Fig. 3.1 are selected for further analysis. The analytical shape of these cuts is given by

<sup>420</sup> Eq. 3.1.1 for electrons and Eq. 3.1.2 for  $\pi^-$

$$\begin{aligned}
\theta_{min} &= 9.7 + 17/(P_{e'} + 0.2) \\
\delta\varphi_{e'} &= p_1 \sin(p_2(\theta_{e'} - \theta_{min}))^{p_3 + p_4/\theta_{e'} + p_5/\theta_{e'}^2} + p_6 \\
p_1 &= 37.3(0.85 + 1.1P_{e'}) \\
p_2 &= 0.01745 \\
p_3 &= p_1/37.3 \\
p_4 &= -62.8 - 30P_{e'} \\
p_5 &= 1525 \\
p_6 &= 0
\end{aligned} \tag{3.1.1}$$

$$\begin{aligned}
\theta_{min} &= 11 + 8/(0.472P_{\pi^-} + 0.117) \\
\delta\varphi_{\pi^-} &= p_1 \sin(p_2(\theta_{\pi^-} - \theta_{min}))^{p_3 + p_4/\theta_{\pi^-} + p_5/\theta_{\pi^-}^2} + p_6 \\
p_1 &= 30.5 \\
p_2 &= 0.01745 \\
p_3 &= 0.705 + 1.1P_{\pi^-} \\
p_4 &= -63.2 - 33.3P_{\pi^-} \\
p_5 &= 1530 \\
p_6 &= -1
\end{aligned} \tag{3.1.2}$$

<sup>421</sup> where  $P_{e'}$  and  $P_{\pi^-}$  are the momenta of the particles in GeV,  $\theta_{e'}$  and  $\theta_{\pi^-}$  are the polar angles  
<sup>422</sup> of the particles in degrees.  $\delta\varphi_{e'}$  and  $\delta\varphi_{\pi^-}$  are the portions of the polar angle  $\varphi$  accepted by  
<sup>423</sup> the fiducial cut, or in other words if  $\theta > \theta_{min}$  and  $|\varphi| < \delta\varphi$  then the particle is accepted.  
<sup>424</sup> The functions 3.1.1,3.1.2 are shown in 2D plots  $\varphi$  versus  $\theta$  in Fig. 3.2 for electrons (left side)  
<sup>425</sup> and  $\pi^-$  (right side).

<sup>426</sup> There are some additional inefficient areas that are not related to the gaps between  
<sup>427</sup> CLAS sectors. These areas are typically caused by drift chamber and time-of-flight system  
<sup>428</sup> inefficiencies (dead wires or PMTs). Some of them are reproduced in Monte Carlo simulation,  
<sup>429</sup> while others are not. To exclude the latter from the analysis additional fiducial cuts on  $\theta$   
<sup>430</sup> versus momentum distributions are applied. These cuts are individual for each CLAS sector.  
<sup>431</sup> They are shown by the black curves for real and Monte Carlo events in Fig. 3.3 for electrons  
<sup>432</sup> and in Fig. 3.4 for  $\pi^-$ . For the electron distributions in Fig. 3.3 only CLAS sector five is  
<sup>433</sup> shown since there are no dead areas in other sectors.

### <sup>434</sup> 3.1.2 Fiducial cuts for positively charged particles

<sup>435</sup> For positively charged particles, which are outbending in the e1e experiment, momentum  
<sup>436</sup> independent and asymmetrical fiducial cuts are the best choice. These cuts are established

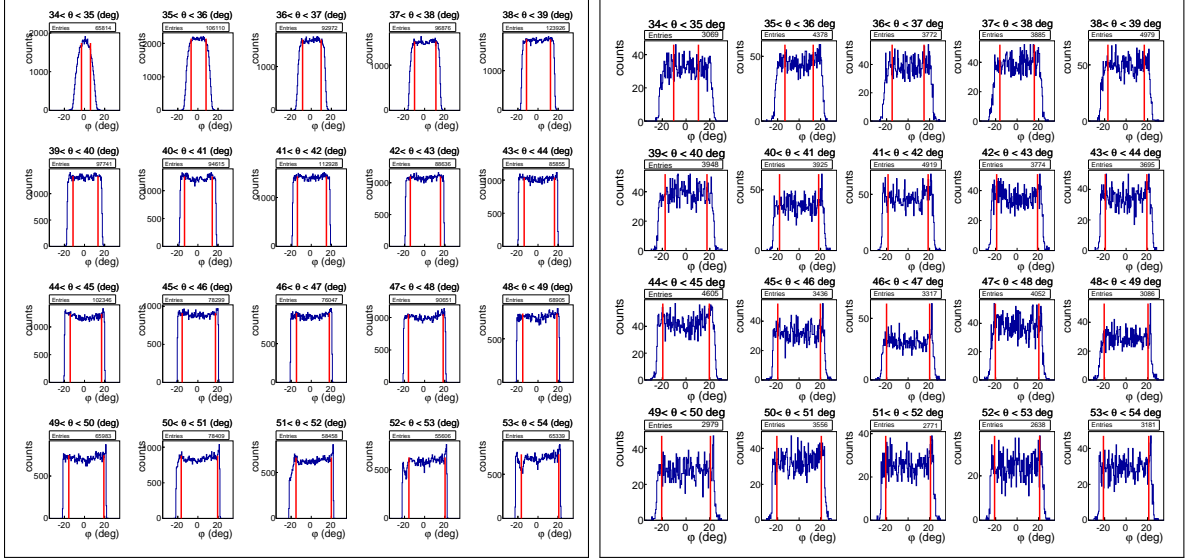


Figure 3.1:  $\varphi$ -event distributions for electrons (left plot) and  $\pi^-$  (right plot). Electrons are shown for CLAS sector 6 and a momentum range from 480 MeV to 560 MeV, while  $\pi^-$  are for sector 3 and a momentum range from 400 MeV to 600 MeV. Various plots represent bins in polar angle  $\theta$ . Events between the red lines are selected for the analysis.

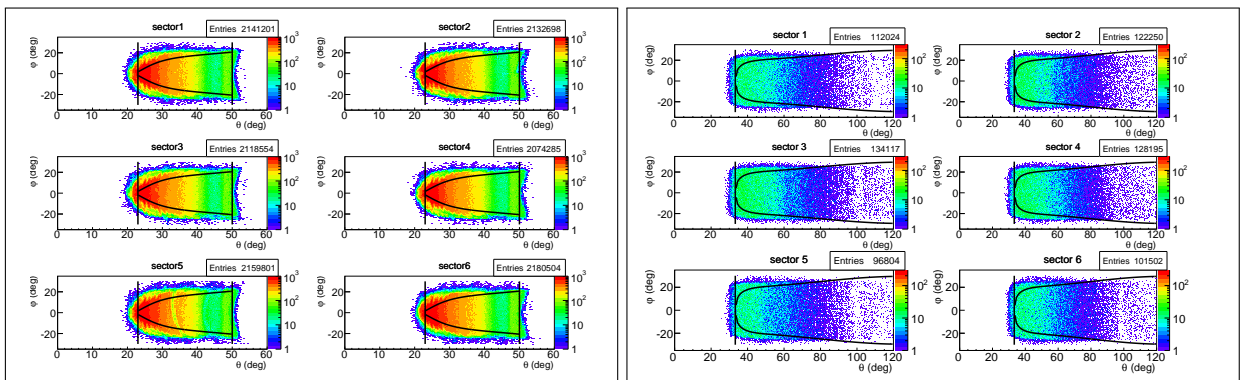


Figure 3.2:  $\varphi$  versus  $\theta$  distributions for electrons with momenta from 1120 MeV to 1200 MeV (left frame) and  $\pi^-$  with momenta from 400 MeV to 600 MeV (right frame) for all six CLAS sectors. Curves show the applied fiducial cuts, vertical lines stand for minimum and maximum  $\theta$  cuts.

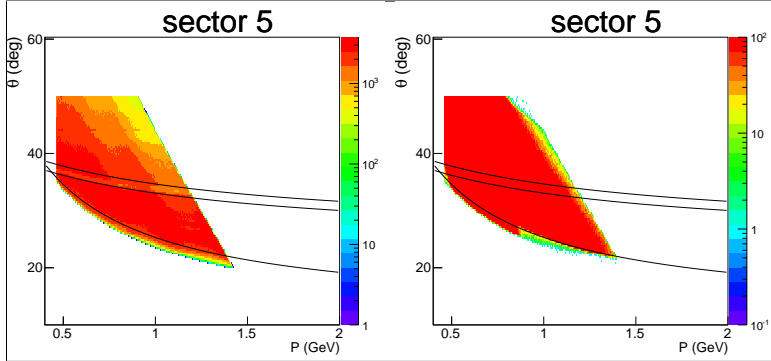


Figure 3.3:  $\theta$  versus momentum distributions for electrons in CLAS sector five. Left plot shows real and right plot Monte Carlo events. Black curves show cuts applied to remove inefficient areas.

437 in the same way as for negatively charged particles, i.e. by selection of the flat parts of the  
 438 event distributions over  $\varphi$ . The shape of these cuts is given by

$$\begin{aligned}\varphi_{upper} &= 24(1 - e^{-0.08(\theta-9)}) \\ \varphi_{lower} &= -25(1 - e^{-0.1(\theta-10)}),\end{aligned}\quad (3.1.3)$$

439 where  $\theta$  is the particle angle in degrees.  $\varphi_{upper}$  and  $\varphi_{lower}$  are the upper and lower cut  
 440 boundaries. Events with  $\varphi_{lower} < \varphi < \varphi_{upper}$  are selected for further analysis.

441 This function is superimposed on the 2D  $\varphi$  versus  $\theta$  distributions of real events and shown  
 442 in Fig. 3.5 by the black curves. Additional cuts in  $\theta$  versus momentum coordinates are shown  
 443 by the black curves for Monte Carlo and real events in Fig. 3.6 for protons and in Fig. 3.7  
 444 for  $\pi^+$ .

## 445 3.2 Data quality check

446 During the quite long experimental run the variations of the experimental conditions, like  
 447 the target density deviation or improper operation of some parts of the detector, can lead to  
 448 different yields of events. Only parts of the run with relatively stable event rates are selected  
 449 for the analysis. For that purpose cuts on DAQ live time and number of events per Faraday  
 450 cup (FC) charge are used.

451 FC charge updates with given frequency, so the whole run time can be divided into so-  
 452 called *blocks*. Each *block* corresponds to the portion of time between two FC charge readouts.  
 453 FC charge readout happens approximately once in ten seconds. The *block* number ranges  
 454 from one to the maximum number over the run time. The first and last *blocks* in each run

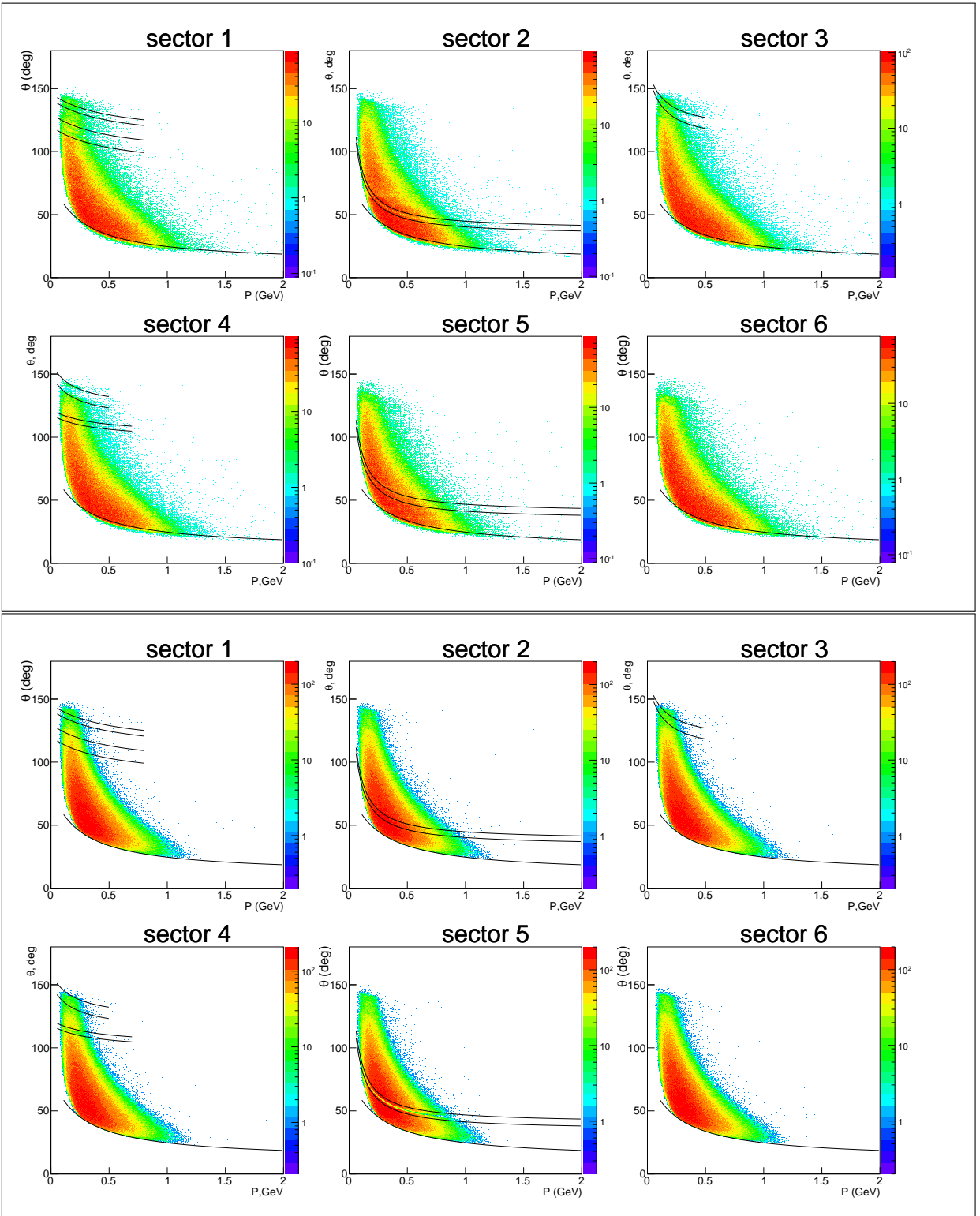


Figure 3.4:  $\theta$  versus momentum distributions for real  $\pi^-$  events (upper frame) and for Monte Carlo events (lower frame) for all six CLAS sectors. Black curves show cuts applied to remove inefficient areas.

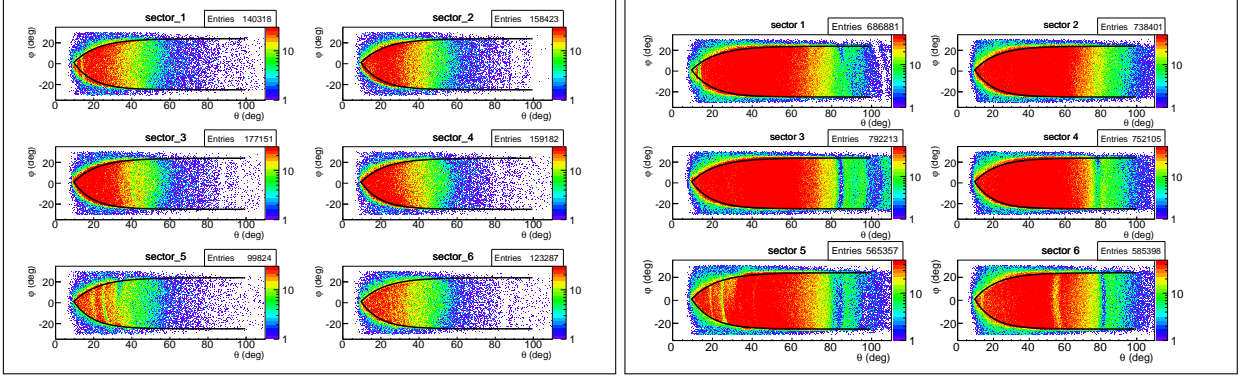


Figure 3.5:  $\varphi$  versus  $\theta$  distributions for protons with momenta from 600 MeV to 800 MeV (left frame) and  $\pi^+$  with momenta from 400 MeV to 600 MeV (right frame) for all six CLAS sectors. Curves show the applied fiducial cuts.

file are excluded from the analysis since FC readout is not synchronized with begin/end of the file.

DAQ live time is the portion of time within the *block* during which the DAQ is able to accumulate events. A significant deviation of the live time from the average value indicates event rate alteration. For instance, if the live time is close to one, then the event rate is too low and vice versa. In Fig. 3.8 DAQ live time and yields of elastic and inclusive events normalized to FC charge are shown as function of *block* number. *Blocks* between the horizontal red lines in Fig. 3.8 are selected for the analysis. Due to the enormous amount of *blocks* all of them can not be made visible in two dimensional histogram, so y-axis projections of histograms in Fig. 3.8 are produced (see Fig. 3.9). The horizontal red cut lines in Fig. 3.8 correspond to the vertical red cut lines in Fig. 3.9.

### 3.3 Vertex cut

The target is specific to the e1e experiment and its setup is presented in Fig. 3.10. It has a conical shape with diameter varying from 0.4 to 0.6 cm. In some instances cooling system could not extract all the heat generated by the beam and the hydrogen in the target cell could boil. If bubbles stay along the beamline, the real luminosity would be different from the expected value and the absolute measurement will lack accuracy. The conical shape helps to direct bubbles upwards and into a wider area of the target, thus clearing the beamline. The forward aluminum window is made exactly the same as the entry/exit windows of the target cell and can serve for both the estimation of the number of events originated in the target windows and to precisely measure target  $z$  position in the beamline.

In Fig. 3.11 distributions of electron coordinate  $z$  at the interaction vertex are shown for

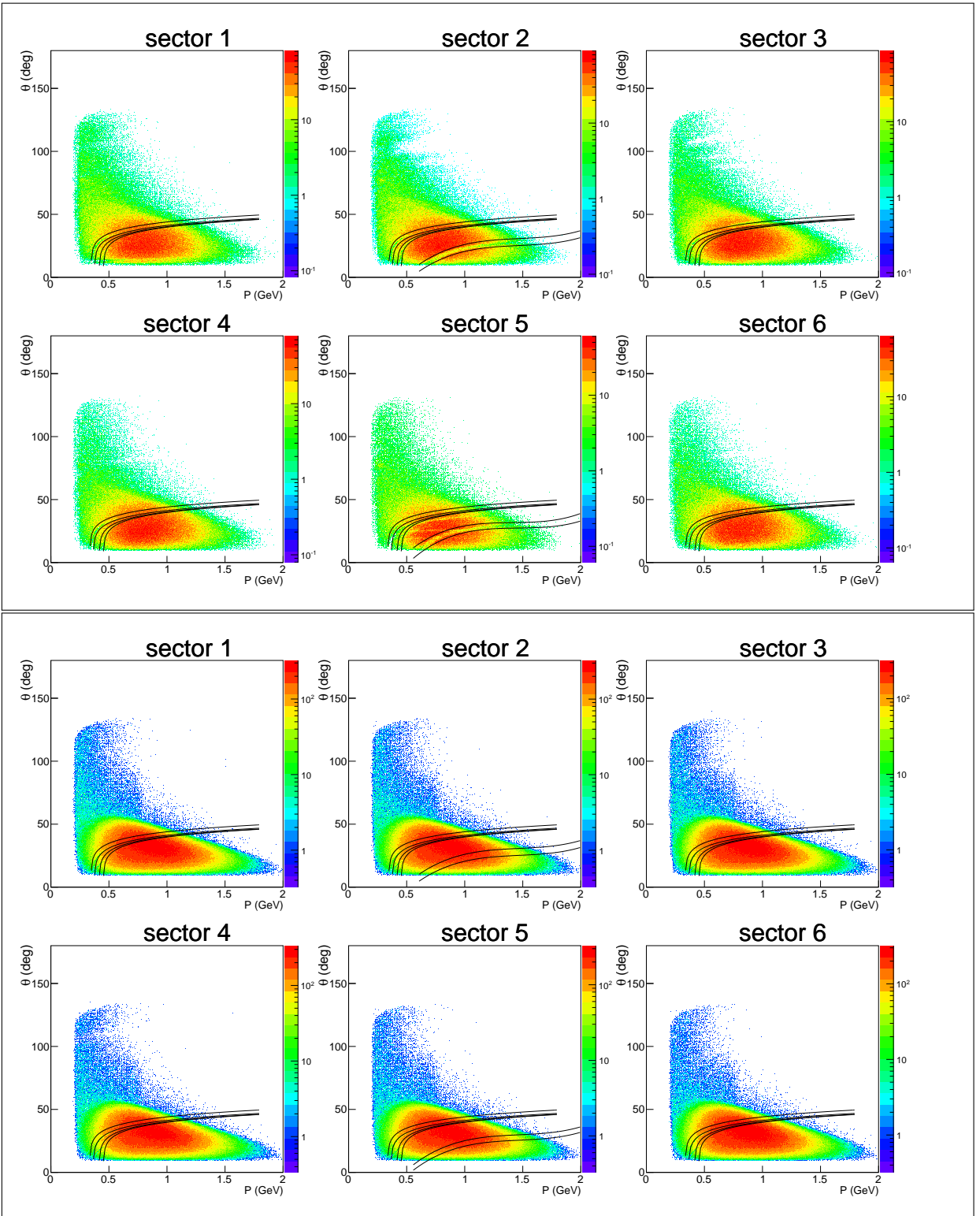


Figure 3.6:  $\theta$  versus momentum distributions for real proton events (upper frame) and for Monte Carlo events (lower frame) for all six CLAS sectors. Black curves show cuts applied to remove inefficient areas.

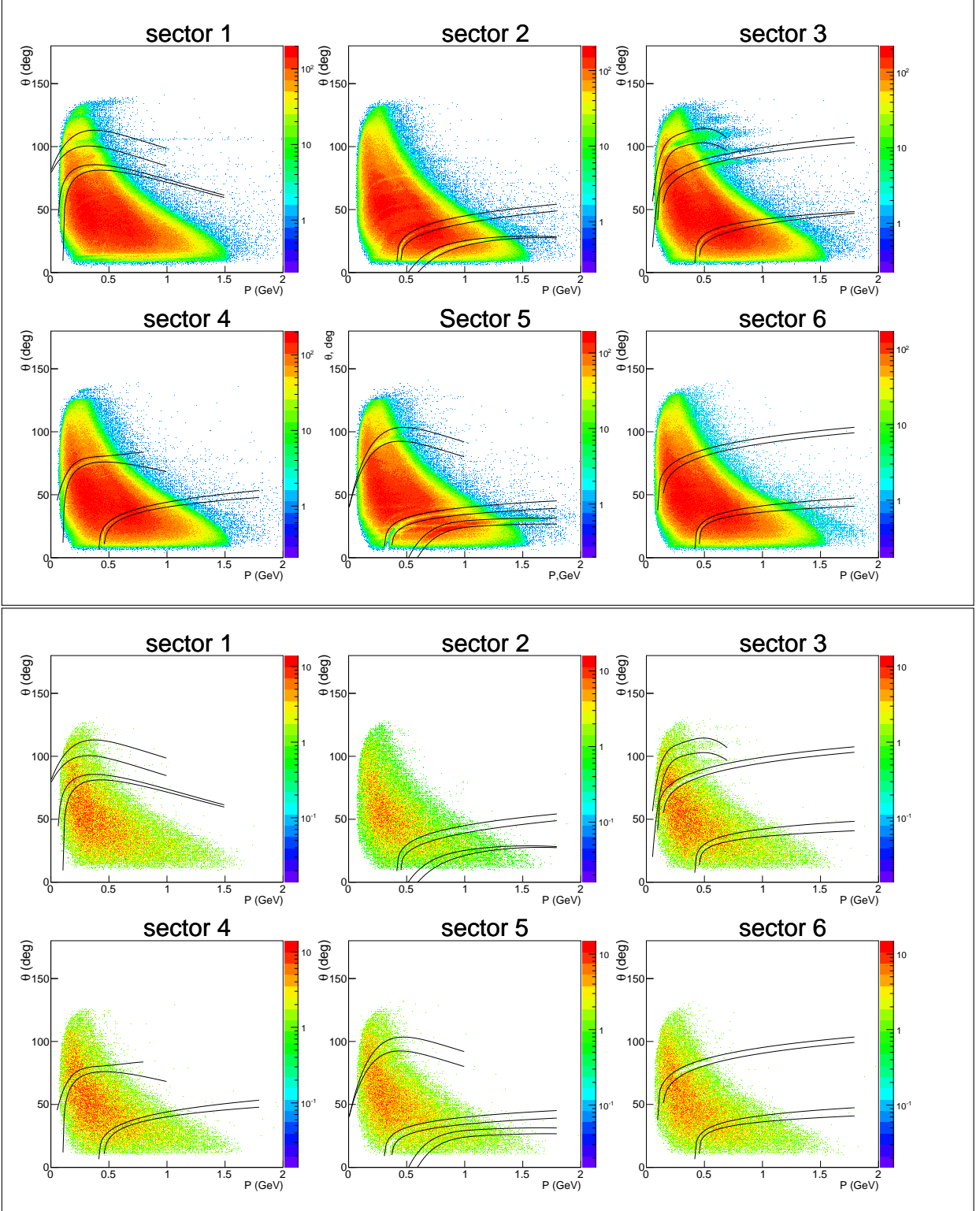


Figure 3.7:  $\theta$  versus momentum distributions for real  $\pi^+$  events (upper frame) and for Monte Carlo events (lower frame) for all six CLAS sectors. Black curves show cuts applied to remove inefficient areas.

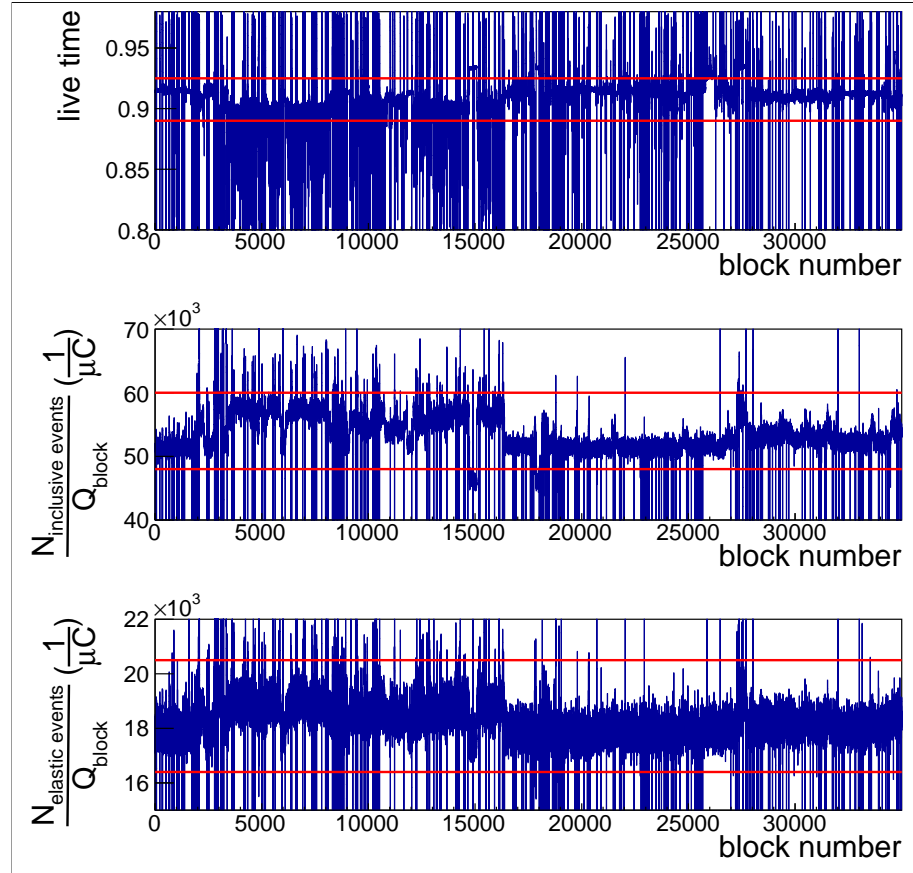


Figure 3.8: In the top plot DAQ live time is shown as function of *block* number. Each *block* corresponds to the portion of events that is accumulated during a single Faraday cup charge reading cycle. *Block* numbers range from one to the maximum number and represents the run duration in Faraday cup reading units. In the middle plot the number of inclusive events accumulated within each *block* divided by FC charge accumulated during the *block* is plotted versus *block* number. Bottom plot shows the number of elastic events accumulated within each *block* divided by FC charge accumulated during the *block* as function of *block* number. Horizontal red lines show the applied cuts.

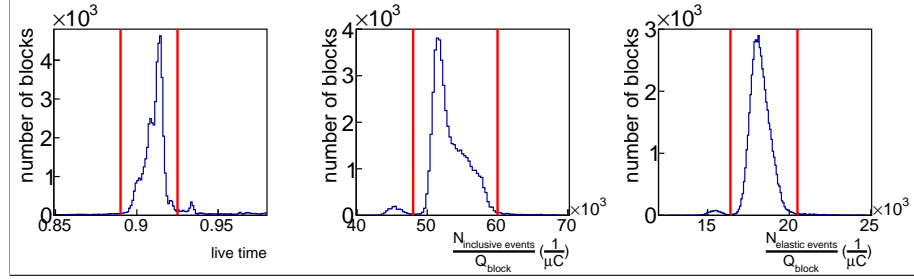


Figure 3.9: Number of *block* occurrences (see explanation in the text) as function of DAQ live time (left plot), inclusive event yield normalized to FC charge (middle plot), and elastic event yield normalized to FC charge (right plot).

477 events from both empty and full target runs for six CLAS sectors. The vertex coordinate  $z$   
 478 is taken from DCPB bank, where already beam-offset corrected values are stored. However  
 479 small vertex corrections are made to shift the peak that corresponds to the forward aluminum  
 480 window to the same position for full and empty target runs. Vertical green lines in Fig. 3.11  
 481 show the cut that is applied in addition to the empty target event subtraction.

482 In Fig. 3.12 event distributions after subtraction of empty target contribution are shown  
 483 in comparison with Monte Carlo events both reconstructed and generated. As it can be seen  
 484 in Fig. 3.12 the simulation reproduces data well enough.

485 To reduce the number of events in which the electron comes from one and any hadron  
 486 from another event, additional cuts on the difference of  $z$  coordinates of particles at the  
 487 vertex are applied. These cuts do not allow the registered particles to have  $z$  vertices farther  
 488 apart than 4 cm.

### 489 3.4 Exclusivity cut

490 Due to the experimental conditions the statistics of the double-pion events with all final  
 491 hadrons registered is rather limited. Moreover, registration of all final hadrons leads to a  
 492 limited acceptance, so the missing mass technique, when one of the final hadrons is not  
 493 registered, is the best choice for the double-pion cross section extraction.

494 For the analyzed reaction one can distinguish four topologies:

- 495 •  $ep \rightarrow e' p' \pi^+ X$
- 496 •  $ep \rightarrow e' p' \pi^- X$
- 497 •  $ep \rightarrow e' \pi^+ \pi^- X$
- 498 •  $ep \rightarrow e' p \pi^+ \pi^- X$

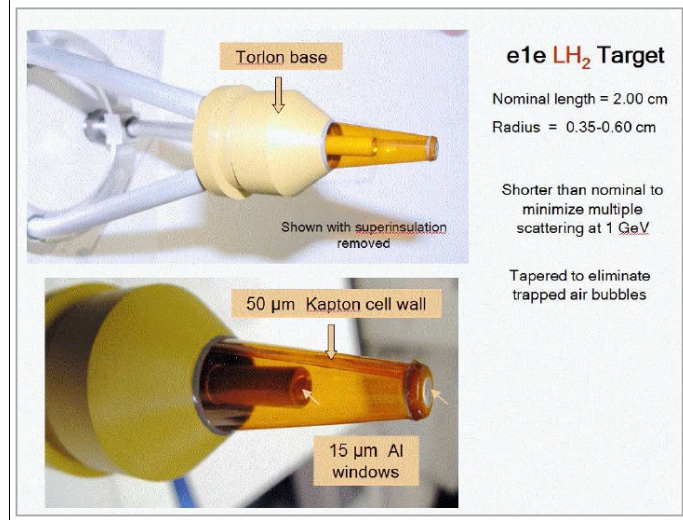


Figure 3.10: The target cell and support structure used during e1e run period.

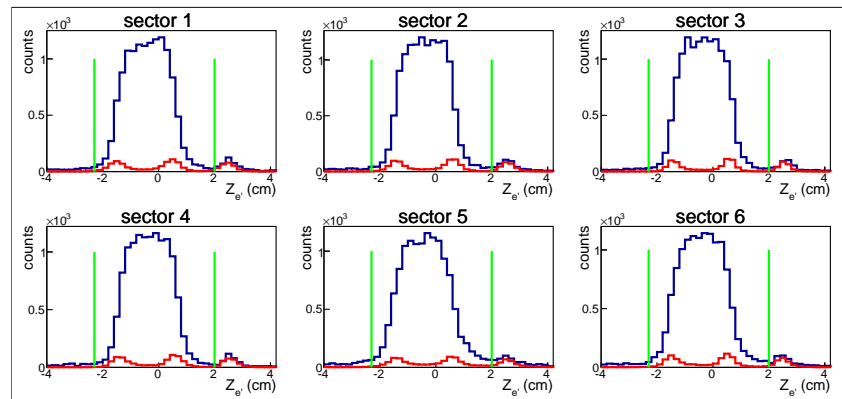


Figure 3.11: Distributions of the electron  $z$  coordinate at the vertex for full (blue curves) and empty (red curves) target runs for six CLAS sectors. Vertical green lines show the applied cuts. Both full and empty target distributions are normalized to the corresponding FC charge.

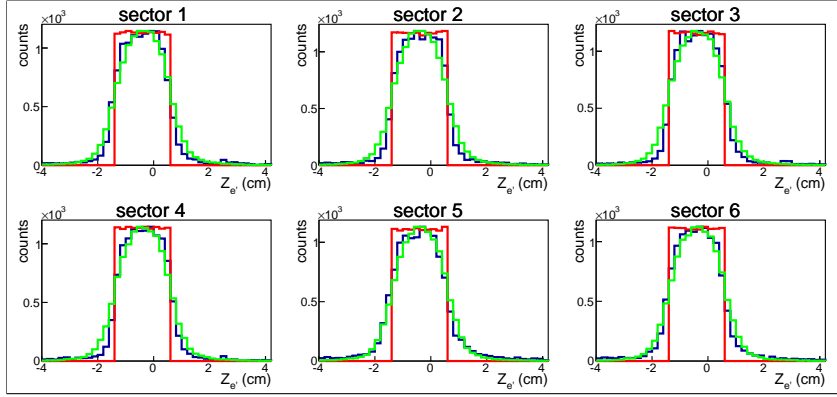


Figure 3.12: Distributions of the electron  $z$  coordinate at the vertex for data (blue curves) and Monte Carlo (green curves - reconstructed, red - generated) events for six CLAS sectors. For data empty target contributions are subtracted. All distributions are normalized to the maximum.

These topologies are defined in a way they do not overlap. For example the topology  $ep \rightarrow e'p'\pi^+X$  requires the presence of  $e'$ ,  $p'$  and  $\pi^+$  candidates and absence of  $\pi^-$  candidates, avoiding in this way double counting.

For the case when one of the final hadrons is not registered, the missing mass  $M_X$  for the reaction  $ep \rightarrow e'h_1h_2X$  is determined by

$$M_X^2 = (P_e + P_p - P_{e'} - P_{h_1} - P_{h_2})^2, \quad (3.4.1)$$

where  $P_{h_1}$  and  $P_{h_2}$  are the four-momenta of the registered final hadrons,  $P_e$  and  $P_p$  - four-momenta of initial electron and proton, and  $P_{e'}$  - four-momentum of the scattered electron.

While for the events with all final hadrons registered, the missing mass  $M_X$  for the reaction  $ep \rightarrow e'p'\pi^+\pi^-X$  is given by

$$M_X^2 = (P_e + P_p - P_{e'} - P_{\pi^+} - P_{\pi^-} - P_{p'})^2, \quad (3.4.2)$$

where  $P_e$ ,  $P_p$ ,  $P_{e'}$ ,  $P_{\pi^+}$ ,  $P_{\pi^-}$ , and  $P_{p'}$  are the four-momenta of the initial and final particles.

Distributions of the missing mass squared for various topologies are shown in Fig. 3.13 for different  $W$  bins in comparison with Monte Carlo. The top row in Fig. 3.13 stands for the  $\pi^-$ -missing topology, the second row - for  $\pi^+$ -missing topology, the third row - for proton-missing topology, and the bottom row for the case when all final hadrons are registered. The green arrows show the applied cuts. The  $\pi^-$ -missing topology contributes the biggest part to the statistics (about 70%), while events from other topologies populate kinematical areas with no acceptance for the  $\pi^-$ -missing topology. By combining events from various topologies one can reduce contributions from kinematical cells with zero acceptance (so-called empty cells) (see Sect. 4.5).

518     The simulation is carried out with the JM05 version of double-pion production model  
 519 [28–30] and includes inclusive radiative effects according to [31]. More details about Monte  
 520 Carlo simulation are in Sect. 4.4.

521     The contribution from the other exclusive channels (exclusive background) to the events  
 522 within the exclusivity cuts is also taken into account by the Monte Carlo simulation. Most  
 523 of the exclusive background events come from the  $ep \rightarrow e'p'\pi^+\pi^-\pi^0$  channel. Both double-  
 524 pion and three-pion channels are generated together with the relative weight of their cross  
 525 sections taken from [32]. A phase space distribution is assumed for the  $3\pi$  events. The  $3\pi$   
 526 background can be barely seen as a separate peak on the right side of the missing mass  
 527 squared distributions for the exclusive topology in last two  $W$  bins (see Fig. 3.13 bottom row). For the other topologies the  $3\pi$  background can not be seen as a separate peak and  
 528 it manifests itself as a contribution to the tail on the right side of the missing mass squared  
 529 distributions.  
 530

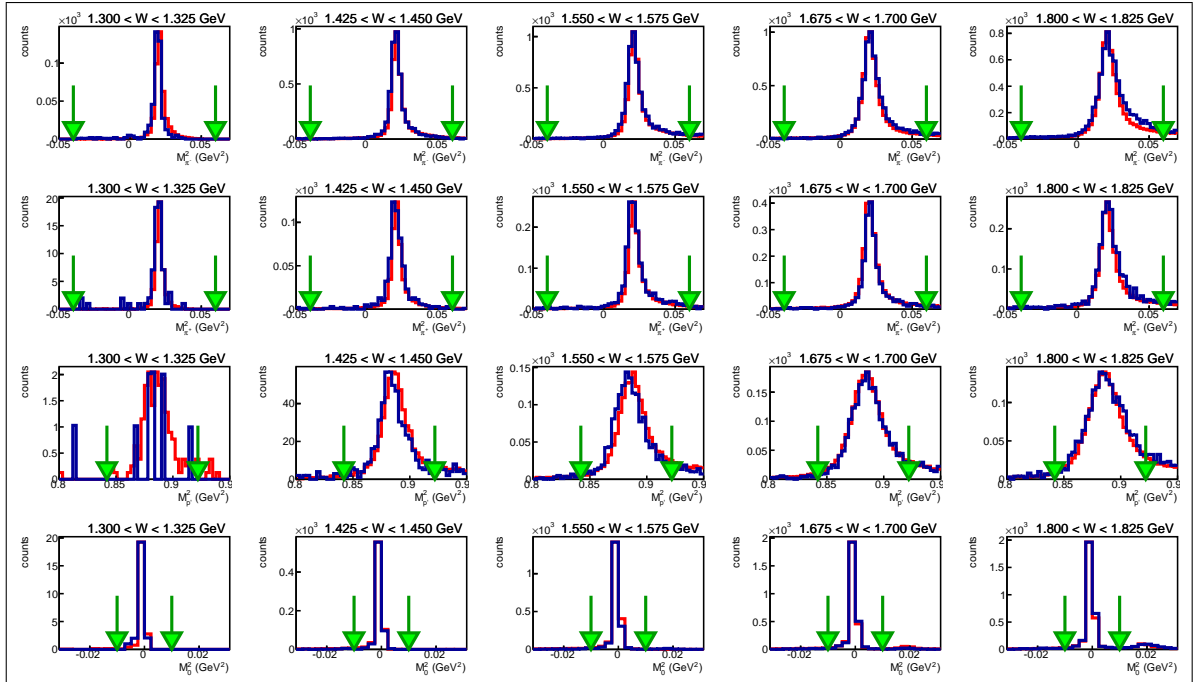
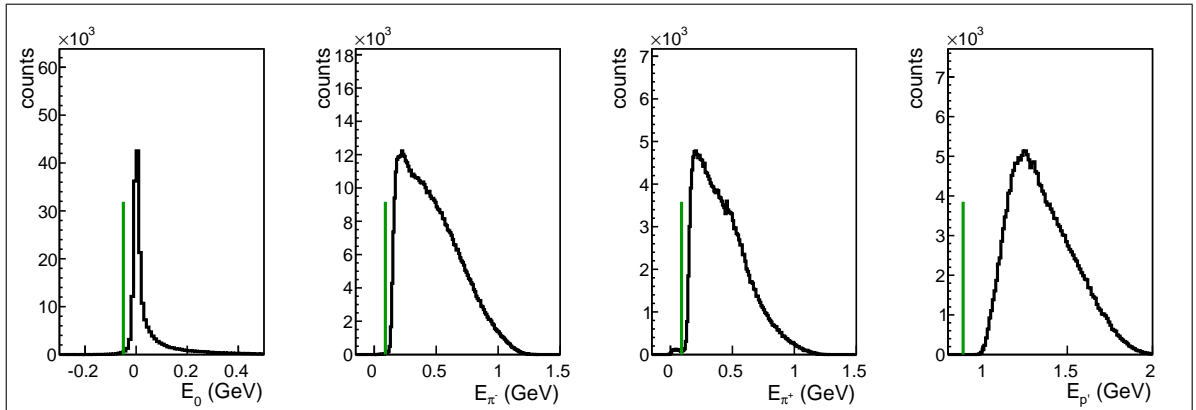


Figure 3.13: Missing mass squared distributions for various bins in  $W$  for  $Q^2$  from  $0.45 \text{ GeV}^2$  to  $0.5 \text{ GeV}^2$ . Blue curves show real and red curves Monte Carlo events. The top row corresponds to  $\pi^-$ -missing topology, the second to  $\pi^+$ -missing topology, the third to proton-missing topology, and the bottom to the fully exclusive topology. Green arrows show the applied exclusivity cuts.

## 531 3.5 Missing energy cut

532 To clean up event samples from misidentified and out-of-time particles, a cut on the missing  
 533 energy is used in addition to the missing mass cut (Sect. 3.4). It limits the missing energy to  
 534 be greater than  $m_{miss.hadron} - 50$  MeV, where  $m_{miss.hadron}$  is equal to the mass of the missing  
 535 hadron ( $\pi^-$ ,  $\pi^+$ , or proton depending on the topology) or zero for the topology where all  
 536 final hadrons are registered. The position of this cut is shown by the green vertical lines in  
 Fig. 3.14.



537 Figure 3.14: Missing energy distributions for various topologies. Left plot corresponds to the topology where all final hadrons are registered and other plots correspond to the topologies with missing  $\pi^-$ ,  $\pi^+$ , or proton, respectively. Green vertical lines show the applied cut. All events on the right side of the lines are selected as good for analysis.

537

## 538 3.6 Binning and kinematical coverage

539 After all described above cuts and corrections about 2.5 million double-pion events survive  
 540 and are used for the cross section calculation. Figure 3.15 shows the available kinematical  
 541 coverage in electron variables. double-pion cross sections are calculated in 2D cells within  
 542 the white boundaries in Fig. 3.15.

543 The binning in the final hadron variables is chosen according to the statistics left after  
 544 the event selection (see Tab. 3.1) and takes into account the fact that the cross section is  
 545 small in the  $W$  area near the double-pion production threshold. A more detailed description  
 546 of the final hadron variable choice is given in Sect. 4.1.

547 It also needs to be mentioned that the right boundary of the invariant mass distributions

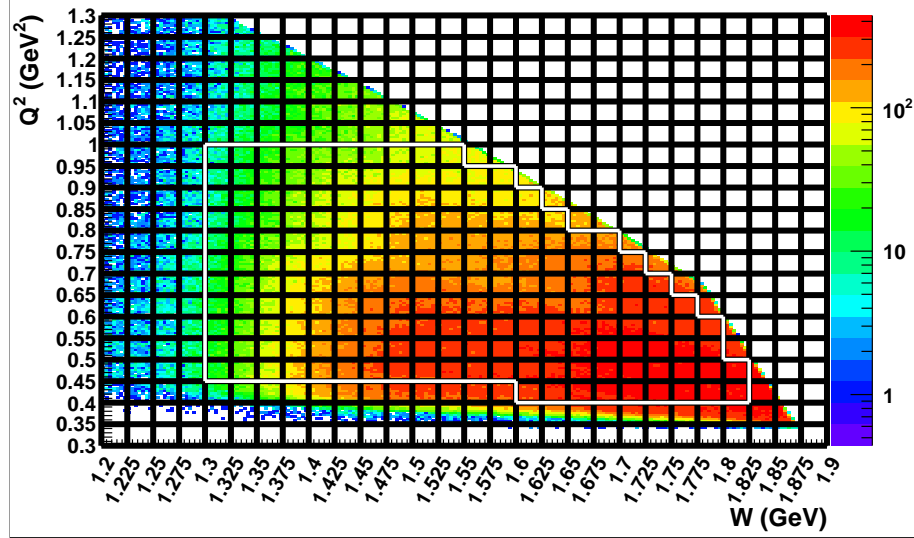


Figure 3.15:  $Q^2$  versus  $W$  distribution populated with selected double-pion events. The cross section is calculated in 2D cells within the white boundaries.

548 depends on the value of  $W$ , while the left does not (see Eq. 3.6.1).

$$\begin{aligned} M_{left} &= m_{h_1} + m_{h_2} \\ M_{right} &= W - m_{h_3}, \end{aligned} \quad (3.6.1)$$

549 where  $M_{left}$  and  $M_{right}$  are the left and right boundaries of the invariant mass distribution.  
550  $m_{h_1}$ ,  $m_{h_2}$ , and  $m_{h_3}$  are the masses of final hadrons. The value of  $W$  is taken in the center of  
551 the corresponding  $W$  bin.

552 It leads to the fact that invariant mass distributions are broader at high  $W$  and hence a  
553 more detailed binning in that area is necessary (see Tab. 3.1).

554 Since  $M_{right}$  is calculated using the value of  $W$  in the center of the corresponding  $W$   
555 bin some events are located beyond the boundaries determined by Eq. 3.6.1. Therefore the  
556 binning in invariant mass needs special attention. Firstly the bin width is determined as:

$$width = \frac{M_{right} - M_{left}}{N_{bins} - 1}, \quad (3.6.2)$$

557 where  $N_{bins}$  is the number of bins.

558 Then the invariant mass distributions are obtained with the number of bins  $N_{bins}$  and  
559 the left boundary of the first bin is set to  $M_{left}$ . That makes the last bin to be situated  
560 completely out of the boundaries given by Eq. 3.6.1. Although the cross section obtained  
561 in this bin is very small, it is kept in analysis since its content contributes to all other cross  
562 sections obtained by integration over the corresponding invariant mass. After the binning

<sup>563</sup> corrections this effect is assumed to be taken into account and this last bin in invariant masses is neglected.  
<sup>564</sup>

Variable $W$ range	Number of bins in invariant mass $M$	Number of bins in polar angle $\theta$	Number of bins in azimuthal angle $\varphi$	Number of bins in angle between two planes $\alpha$
1.3 - 1.35 GeV	8	6	5	5
1.35 - 1.4 GeV	10	8	5	6
1.4 - 1.45 GeV	12	10	5	8
$> 1.45$ GeV	12	10	8	8

Table 3.1: Number of bins for the given final hadron variables.

<sup>565</sup> Chapter 4

<sup>566</sup> Cross section calculation

<sup>567</sup> 4.1 Kinematical variables

<sup>568</sup> After the double-pion event selection that uses the missing mass technique, the four-momenta  
<sup>569</sup> of all particles are known and can be used for the calculation of all kinematic variables. The  
<sup>570</sup> cross sections are obtained in the single-photon exchange approximation in the center of  
<sup>571</sup> mass frame of the *virtual photon – initial proton* system.

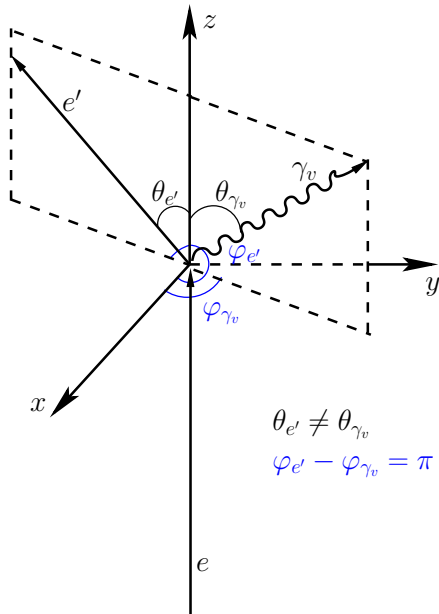


Figure 4.1: Virtual photon and scattered electron angles  $\theta$  and  $\varphi$  in the lab frame.

572 Therefore, to calculate the kinematic variables the four-momenta of all particles need to  
 573 be transformed from the lab frame to the c.m. frame. For that purpose Lorentz transforma-  
 574 tions that include the following steps are used <sup>1</sup>.

575 1) Firstly ( $xy$ )-plane of the lab system is rotated around  $z$ -axis to make  $x$ -axis laying in  
 576 the electron scattering plane (see Fig. 4.1). This rotation transforms the four-momentum as  
 577  $P' = P * R_1$ , with

$$R_1 = \begin{pmatrix} \cos(\varphi_{e'}) & -\sin(\varphi_{e'}) & 0 & 0 \\ \sin(\varphi_{e'}) & \cos(\varphi_{e'}) & 0 & 0 \\ 0 & 0 & 1 & 0 \\ 0 & 0 & 0 & 1 \end{pmatrix}, \quad (4.1.1)$$

578 where  $\varphi_{e'}$  is the azimuthal angle of the scattered electron.

579 After this rotation  $\varphi_{\gamma_v} = \pi$ , since the  $\varphi$  angle between scattered electron and virtual  
 580 photon is equal to  $\pi$ ; and after the rotation  $\varphi_{e'} = 0$  with respect to the intermediate reference  
 581 frame.

582 2) After that the lab system is rotated to align the  $z$ -axis with the virtual photon direction.  
 583 The four-momentum transformation for this rotation is given by  $P'' = P' * R_2$ , with

$$R_2 = \begin{pmatrix} \cos(\theta_{\gamma_v}) & 0 & -\sin(\theta_{\gamma_v}) & 0 \\ 0 & 1 & 0 & 0 \\ \sin(\theta_{\gamma_v}) & 0 & \cos(\theta_{\gamma_v}) & 0 \\ 0 & 0 & 0 & 1 \end{pmatrix}, \quad (4.1.2)$$

584 where  $\theta_{\gamma_v}$  is the polar angle of the virtual photon. <sup>2</sup>

585 3) Finally a boost into the c.m. frame of the *virtual photon – initial proton* system is

---

<sup>1</sup>In all derivations the energy is assumed to be the last component of the four-momentum and the four-momentum to be a row vector.

<sup>2</sup>Using embedded ROOT functions, both rotations can be coded using the unit vectors TVector3  $uz = P4\_gamma.Vect().Unit()$  and TVector3  $ux = (P4\_EL.Vect().Cross(P4\_ELP.Vect())).Unit()$ , where P4\_gamma, P4\_EL, and P4\_ELP are the four-momenta of the virtual photon, initial and final electrons, respectively. The axis vector  $ux$  needs to be rotated according to  $ux.Rotate(3.*M_PI/2,uz)$ . Finally the rotation is defined as  $rot.SetZAxis(uz,ux).Invert()$  and needs to be applied to the four-momentum (P4) of each particle:  $P4.Transform(rot)$ .

<sup>586</sup> performed. It is given by the formula  $P''' = P'' * R_3$ , with

$$R_3 = \begin{pmatrix} 1 & 0 & 0 & 0 \\ 0 & 1 & 0 & 0 \\ 0 & 0 & \gamma & -\gamma\beta \\ 0 & 0 & -\gamma\beta & \gamma \end{pmatrix}, \quad \beta = \frac{|\vec{q}|}{E_\gamma + m_{proton}} = \frac{\sqrt{E_\gamma^2 + Q^2}}{E_\gamma + m_{proton}}, \quad \gamma = \frac{1}{\sqrt{1 - \beta^2}}, \quad (4.1.3)$$

<sup>587</sup> where  $|\vec{q}|$  is the magnitude of the three-vector of the virtual photon and  $\beta$  the magnitude  
<sup>588</sup> and  $z$ -component of the three-vector  $\vec{\beta} = (0, 0, \beta)$ . <sup>3</sup>

<sup>589</sup> When the four-momenta of all particles in the c.m. frame are defined one can calculate  
<sup>590</sup> the kinematic variables that describe the final hadron state. The three-body final state is  
<sup>591</sup> unambiguously determined by five kinematic variables. Indeed, three final particles could be  
<sup>592</sup> described by  $4 \times 3 = 12$  components of their four-momenta. All these particles are on mass  
<sup>593</sup> shell. So, it gives us three restrictions  $E_i^2 - P_i^2 = m_i^2$  ( $i = 1, 2, 3$ ). The energy-momentum  
<sup>594</sup> conservation imposes four additional constraints for the final particles four-momenta com-  
<sup>595</sup> ponents. So, eventually five kinematic variables remain, which determine unambiguously  
<sup>596</sup> the three-body final state kinematics. In the electron scattering process  $ep \rightarrow e'p'\pi^+\pi^-$  the  
<sup>597</sup> variables  $W, Q^2$  are also present besides the hadronic final state variables. So electron scat-  
<sup>598</sup> tering cross section for double-charged pion electroproduction should be seven-differential:  
<sup>599</sup> five variables for the final hadrons plus  $W$  and  $Q^2$  that are determined by the scattered elec-  
<sup>600</sup> tron kinematics. Such seven-differential cross sections may be written as  $\frac{d^7\sigma}{dWdQ^2d^5\tau}$ , where  
<sup>601</sup>  $d^5\tau$  is five-dimensional phase space differential.

<sup>602</sup> Several sets of five variables for the description of the final hadron kinematics may be  
<sup>603</sup> used. The following generalized set of variables is used in this analysis:

- <sup>604</sup> • invariant mass of the first pair of the particles  $M_{12}$ ;
- <sup>605</sup> • invariant mass of the second pair of the particles  $M_{23}$ ;
- <sup>606</sup> • the first particle solid angle  $\Omega$ ;
- <sup>607</sup> • the angle between two planes: one of them (plane A) is defined by the three-momenta  
<sup>608</sup> of the virtual photon (or initial proton) and the first final hadron, the second plane  
<sup>609</sup> (plane B) is defined by the three-momenta of all final hadrons (these angles are shown  
<sup>610</sup> in Figs. 4.3, 4.4, 4.5 for various choices of the first particle).

<sup>611</sup> The cross sections in this analysis are obtained in three sets of variables depending on  
<sup>612</sup> various assignments for the first, second, and third final hadrons:

---

<sup>3</sup> Note: if you use ROOT function `.Boost` you should change the sign of the  $z$ -component of  $\beta$ -vector:  
`.Boost(0,0,-\beta)`.

- invariant mass of the  $p'\pi^+$  pair, invariant mass of the  $\pi^+\pi^-$  pair, proton spherical angles  $\theta_{p'}$  and  $\varphi_{p'}$  and angle  $\alpha_{(p,p')(\pi^+,\pi^-)}$  (or  $\alpha_{p'}$ ) between planes B (defined by the momenta of all final hadrons) and A (defined by initial and final protons), see Fig. 4.3;
- invariant mass of the  $\pi^-\pi^+$  pair, invariant mass of the  $\pi^+p$  pair,  $\pi^-$  spherical angles  $\theta_{\pi^-}$  and  $\varphi_{\pi^-}$  and angle  $\alpha_{(\pi^-)(p\pi^+)}$  (or  $\alpha_{\pi^-}$ ) between planes B (defined by the momenta of all final hadrons) and A (defined by initial proton and  $\pi^-$ ), see Fig. 4.4;
- invariant mass of the  $\pi^+\pi^-$  pair, invariant mass of the  $\pi^-p$  pair,  $\pi^+$  spherical angles  $\theta_{\pi^+}$  and  $\varphi_{\pi^+}$  and angle  $\alpha_{(\pi^+)(p\pi^-)}$  (or  $\alpha_{\pi^+}$ ) between planes B (defined by the momenta of all final hadrons) and A (defined by initial proton and  $\pi^+$ ), see Fig. 4.5.

Lets explain in more detail the calculation of the kinematical variables in case of set number two. The invariant masses  $M_{\pi^+\pi^-}$  and  $M_{\pi^+p'}$  are calculated from the four-momenta of the final particles  $P_{\pi^-}$ ,  $P_{\pi^+}$ ,  $P_{p'}$  in the c.m. frame in the following way

$$\begin{aligned} M_{\pi^+\pi^-} &= \sqrt{(P_{\pi^+} + P_{\pi^-})^2} \text{ and} \\ M_{\pi^+p'} &= \sqrt{(P_{\pi^+} + P_{p'})^2}. \end{aligned} \quad (4.1.4)$$

The angle  $\theta_{\pi^-}$  between the three-momentum of the initial photon ( $\vec{P}_\gamma$ ) and three-momentum of the final  $\pi^-$  ( $\vec{P}_{\pi^-}$ ) in c.m. frame is calculated as:

$$\theta_{\pi^-} = \arccos \left( \frac{(\vec{P}_{\pi^-} \cdot \vec{P}_\gamma)}{|\vec{P}_{\pi^-}| |\vec{P}_\gamma|} \right) \quad (4.1.5)$$

The angle  $\varphi_{\pi^-}$  is determined as:

$$\begin{aligned} \varphi_{\pi^-} &= \arctg \left( \frac{P_{y\pi^-}}{P_{x\pi^-}} \right); P_{x\pi^-} > 0; P_{y\pi^-} > 0 \\ \varphi_{\pi^-} &= \arctg \left( \frac{P_{y\pi^-}}{P_{x\pi^-}} \right) + 2\pi; P_{x\pi^-} > 0; P_{y\pi^-} < 0 \\ \varphi_{\pi^-} &= \arctg \left( \frac{P_{y\pi^-}}{P_{x\pi^-}} \right) + \pi; P_{x\pi^-} < 0; P_{y\pi^-} < 0 \\ \varphi_{\pi^-} &= \arctg \left( \frac{P_{y\pi^-}}{P_{x\pi^-}} \right) + \pi; P_{x\pi^-} < 0; P_{y\pi^-} > 0 \\ \varphi_{\pi^-} &= \pi/2; P_{x\pi^-} = 0; P_{y\pi^-} > 0 \\ \varphi_{\pi^-} &= 3\pi/2; P_{x\pi^-} = 0; P_{y\pi^-} < 0, \end{aligned} \quad (4.1.6)$$

where  $P_{i\pi^-}$  is  $i$ -component of the  $\pi^-$  three-momentum ( $i = x, y, z$ ). The angles  $\theta_{\pi^-}$  and  $\varphi_{\pi^-}$  are shown in Fig. 4.2.

630        The calculation of the angle  $\alpha_{\pi^-}$  between two planes A and B (see Fig. 4.4) is more  
 631        complicated. Firstly two auxiliary vectors  $\vec{\gamma}$  and  $\vec{\beta}$  should be determined. The vector  $\vec{\gamma}$  is  
 632        the unit vector perpendicular to the three-momentum  $\vec{P}_{\pi^-}$ , directed toward the vector  $(-\vec{n}_z)$   
 633        and situated in the plane A, which is defined by the three-momentum of initial proton and  
 634        three-momentum of  $\pi^-$ .  $\vec{n}_z$  is the unit vector directed along  $z$ -axis. The vector  $\vec{\beta}$  is the unit  
 635        vector perpendicular to the three-momentum of  $\pi^-$ , directed toward the three-momentum  
 636        of  $\pi^+$  and situated in the plane B, which is defined by all final hadrons. Note that the three-  
 637        momenta of  $\pi^+$ ,  $\pi^-$ ,  $p'$  are in the same plane, since in c.m. frame their total three-momentum  
 638        has to be equal to zero. Then the angle between two planes  $\alpha_{\pi^-}$  is

$$\alpha_{\pi^-} = \arccos(\vec{\gamma} \cdot \vec{\beta}), \quad (4.1.7)$$

639        where  $\arccos$  is a function that runs between zero and  $\pi$ , while the angle  $\alpha_{\pi^-}$  may vary between  
 640        zero and  $2\pi$ . To determine the  $\alpha$  angle in the range between  $\pi$  and  $2\pi$  the relative direction  
 641        between the  $\pi^-$  three-momentum and the vector product  $\vec{\delta} = [\vec{\gamma} \times \vec{\beta}]$  of the auxiliary vectors  
 642         $\vec{\gamma}$  and  $\vec{\beta}$  should be taken into account. If the vector  $\vec{\delta}$  is colinear to the three-momentum of  
 643         $\pi^-$ , the angle  $\alpha_{\pi^-}$  is determined by (4.1.7), and in a case of anti-collinearity by

$$\alpha_{\pi^-} = 2\pi - \arccos(\vec{\gamma} \cdot \vec{\beta}). \quad (4.1.8)$$

644        The defined above vector  $\vec{\gamma}$  can be expressed as

$$\begin{aligned} \vec{\gamma} &= a_\alpha(-\vec{n}_z) + b_\alpha \vec{n}_{P_{\pi^-}} \quad \text{with} \\ a_\alpha &= \sqrt{\frac{1}{1 - (\vec{n}_{P_{\pi^-}} \cdot (-\vec{n}_z))^2}} \quad \text{and} \\ b_\alpha &= -(\vec{n}_{P_{\pi^-}} \cdot (-\vec{n}_z))a_\alpha, \end{aligned} \quad (4.1.9)$$

645        where  $\vec{n}_{P_{\pi^-}}$  is the unit vector directed along the three-momentum of  $\pi^-$  (see Fig. 4.4).  
 646        Taking the scalar products  $(\vec{\gamma} \cdot \vec{n}_{P_{\pi^-}})$  and  $(\vec{\gamma} \cdot \vec{\gamma})$ , it is straightforward to verify, that  $\vec{\gamma}$  is  
 647        the unit vector perpendicular to the three-momentum of  $\pi^-$ .

648        The vector  $\vec{\beta}$  can be obtained as

$$\begin{aligned} \vec{\beta} &= a_\beta \vec{n}_{P_{\pi^+}} + b_\beta \vec{n}_{P_{\pi^-}} \quad \text{with} \\ a_\beta &= \sqrt{\frac{1}{1 - (\vec{n}_{P_{\pi^+}} \cdot \vec{n}_{P_{\pi^-}})^2}} \quad \text{and} \\ b_\beta &= -(\vec{n}_{P_{\pi^+}} \cdot \vec{n}_{P_{\pi^-}})a_\beta, \end{aligned} \quad (4.1.10)$$

649        where  $\vec{n}_{P_{\pi^+}}$  is the unit vector directed along the three-momentum of  $\pi^+$ .  
 650        Again taking the scalar products  $(\vec{\beta} \cdot \vec{n}_{P_{\pi^-}})$  and  $(\vec{\beta} \cdot \vec{\beta})$ , it is straightforward to see, that  
 651         $\vec{\beta}$  is the unit vector perpendicular to the three-momentum of  $\pi^-$ .

652     The angle  $\alpha_{\pi^-}$  coincides with the angle between the vectors  $\vec{\gamma}$  and  $\vec{\beta}$ . So, the scalar  
 653     product  $(\vec{\gamma} \cdot \vec{\beta})$  allows to determine the angle  $\alpha_{\pi^-}$  (4.1.7). The kinematic variables for the  
 654     other assignments for the first, second, and third final hadrons described above, are evaluated  
       in the similar way.

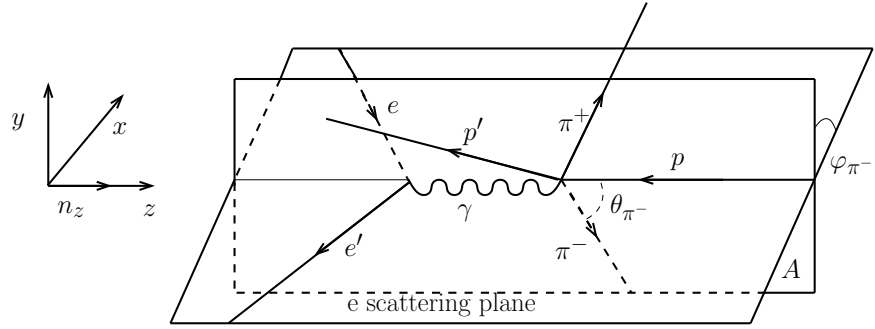


Figure 4.2: Polar ( $\theta_{\pi^-}$ ) and azimuthal ( $\varphi_{\pi^-}$ ) angles of  $\pi^-$  in the c.m. frame.

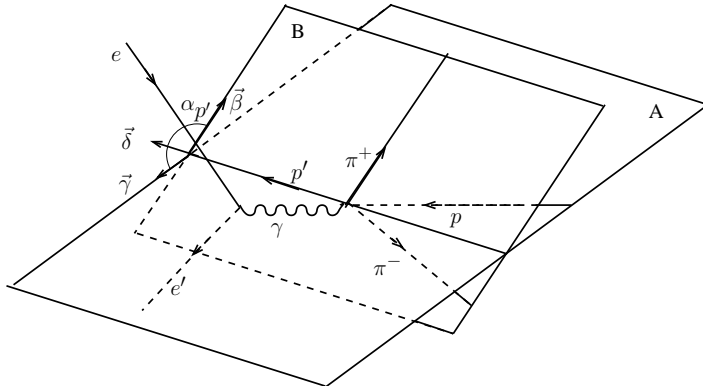


Figure 4.3: Definition of the angle  $\alpha_{p'}$  between two planes: the plane B is defined by the three-momenta of all final hadrons, while the plane A defined by the three-momenta of initial and scattered protons. The definitions of auxiliary vectors  $\vec{\beta}$ ,  $\vec{\gamma}$ ,  $\vec{\delta}$  are given in the text.

655  
 656     Further detailed information about kinematic of the reactions with three-particle final  
 657     states can be found here [33].

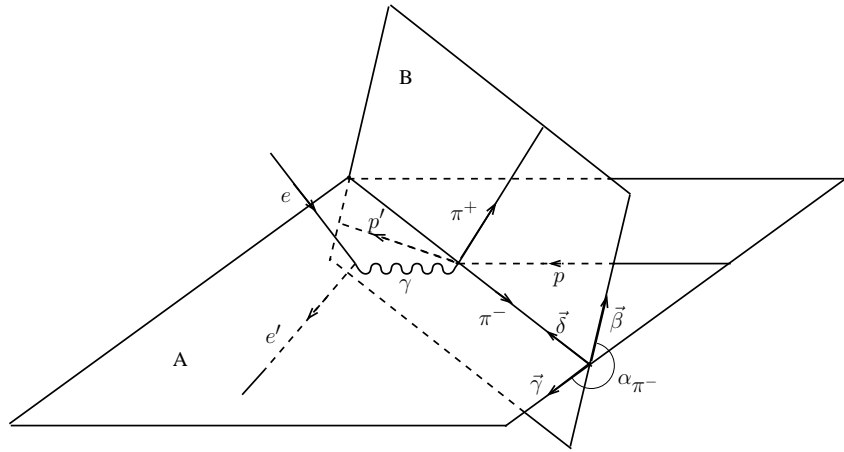


Figure 4.4: Definition of the angle  $\alpha_{\pi^-}$  between two planes: the plane B is defined by the three-momenta of all final hadrons, while the plane A defined by the three-momenta of  $\pi^-$  and initial proton. The definitions of auxiliary vectors  $\vec{\beta}$ ,  $\vec{\gamma}$ ,  $\vec{\delta}$  are given in the text.

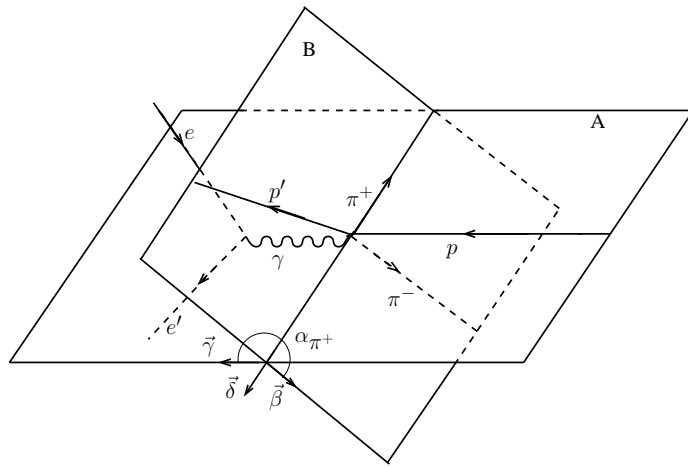


Figure 4.5: Definition of the angle  $\alpha_{\pi^+}$  between two planes: the plane B is defined by the three-momenta of all final hadrons, while the plane A defined by the three-momenta of  $\pi^+$  and initial proton. The definitions of auxiliary vectors  $\vec{\beta}$ ,  $\vec{\gamma}$ ,  $\vec{\delta}$  are given in the text.

## 658 4.2 Cross section formula

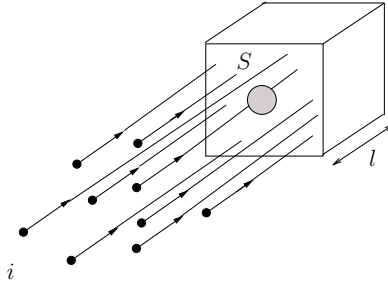


Figure 4.6: The incoming electron beam with the current  $i$  is hitting a homogeneous target with the area  $S$  and density  $\rho$ .

659 In the fixed target experiments (see Fig. 4.6) the interaction rate (the number of interactions per second) can be determined according to the following relation:

$$\frac{dN}{dt} = \frac{iN_{targ}\sigma}{S}, \quad (4.2.1)$$

661 where  $i$  is the beam current (the number of incoming electrons per second),  $N_{targ}$  is the total  
662 number of nuclei inside the target,  $S$  is the taget area,  $\sigma$  is the total cross section.

663 For  $i$  the following is true:

$$i = \frac{dN_{beam}}{dt} = \frac{1}{q_e} \frac{dQ}{dt}, \quad (4.2.2)$$

664 where  $N_{beam}$  is the number of incoming electrons,  $Q$  is the total charge that is carried by  
665 incoming electrons,  $q_e$  is the elementary charge.

666  $N_{targ}$  can be written in this way:

$$N_{targ} = \frac{mN_A}{M_m} = \frac{N_A\rho V}{M_m} = \frac{N_A\rho Sl}{M_m}, \quad (4.2.3)$$

667 where  $m$ ,  $V$ ,  $\rho$ ,  $l$  are the mass, volume, density and length of the target, respectively,  $M_m$  is  
668 the molar mass of the target material,  $N_A$  is the Avogadro constant.

669 From (4.2.1), (4.2.2) and (4.2.3) the cross section

$$\sigma = \frac{q_e \Delta N M_m}{Q l N_A \rho} = \frac{\Delta N}{L}, \quad (4.2.4)$$

670 where  $L = \frac{Q l N_A \rho}{q_e M_m}$  is the luminosity and  $Q$  is the total charge of incoming electrons accumu-  
671 lated in the Faraday cup.

672 Since this analysis is focused on the reaction  $ep \rightarrow e'p'\pi^+\pi^-$ , the quantity  $\Delta N$  in the  
 673 formula (4.2.4) is the total number of double-pion events. Liquid hydrogen is located in the  
 674 target cell, hence the number of events that correspond to the target cell walls needs to be  
 675 subtracted from the number of events that corresponds to the full target.

676 Taking into account that the charge accumulated in the Faraday cup is different for full  
 677 ( $Q_{full}$ ) and empty ( $Q_{empty}$ ) target runs the formula for the total cross section can be rewritten  
 678 as

$$\sigma = \frac{\frac{\Delta N_{full}}{Q_{full}} - \frac{\Delta N_{empty}}{Q_{empty}}}{\frac{l\rho N_A}{q_e M_m}}. \quad (4.2.5)$$

679 As it is mentioned in Sect. 4.1 the double-pion cross section depends on seven kinematical  
 680 variables. For the second set of kinematical variables (see Sect. 4.1) considering formula  
 681 (4.2.5) the seven-differential cross section can be written as

$$\frac{d\sigma}{dW dQ^2 dM_{p\pi^+} dM_{\pi^+\pi^-} d\Omega d\alpha_{\pi^-}} = \frac{1}{F \cdot R} \frac{\left( \frac{\Delta N_{full}}{Q_{full}} - \frac{\Delta N_{empty}}{Q_{empty}} \right)}{\Delta W \Delta Q^2 \Delta \tau \left( \frac{l\rho N_A}{q_e M_H} \right)}, \quad (4.2.6)$$

682 where  $\Delta N_{full}$  and  $\Delta N_{empty}$  are the numbers of events inside the seven-dimensional bin for  
 683 runs with hydrogen and empty target, respectively. Each event is weighted with the cor-  
 684 responding photoelectron correction factor given by Eq. 2.1.12.  $F = F(\Delta W, \Delta Q^2, \Delta \tau)$  is  
 685 total efficiency coming from the Monte Carlo simulation,  $R = R(\Delta W, \Delta Q^2)$  is the radiative  
 686 correction factor,  $Q_{full} = 5999.64 \mu\text{C}$  and  $Q_{empty} = 334.603 \mu\text{C}$  are the integrated Faraday  
 687 cup charges for runs with hydrogen and empty target, respectively. These charges are calcu-  
 688 lated by summing up charges of all corresponding *blocks* that are used in the analysis. See  
 689 the definition of *block* in Section 3.2.  $q_e$  is the elementary charge ( $q_e = 1.610^{-19}\text{C}$ ),  $\rho$  is the  
 690 density of liquid hydrogen ( $\rho = 0.0708 \text{ g/cm}^3$ ) at  $T = 20 \text{ K}$ ,  $l$  is the length of the target  
 691 ( $l = 2 \text{ cm}$ ),  $M_H$  is the molar density of the natural mixture of hydrogen ( $M_H = 1.00794$   
 692  $\text{g/mol}$ ),  $N_A$  is Avogadro's number ( $N_A = 6.0210^{23} \text{ mol}^{-1}$ ),  $\Delta W$  and  $\Delta Q^2$  are kinematical  
 693 bins that are determined by the electron scattering kinematics, and  $\Delta \tau$  is an element of the  
 694 hadronic five-dimensional phase space

$$\Delta \tau = \Delta M_{p\pi^+} \Delta M_{\pi^+\pi^-} \Delta(-\cos(\theta_{\pi^-})) \Delta \varphi_{\pi^-} \Delta \alpha_{\pi^-}. \quad (4.2.7)$$

695 In the single photon exchange approximation, the electron scattering cross section is  
 696 related to the hadronic cross section  $\frac{d\sigma}{dM_{p\pi^+} dM_{\pi^+\pi^-} d\Omega_{\pi^-} d\alpha_{\pi^-}}$  by

$$\frac{d\sigma}{dM_{p\pi^+} dM_{\pi^+\pi^-} d\Omega_{\pi^-} d\alpha_{\pi^-}} = \frac{1}{\Gamma_v} \frac{d\sigma}{dW dQ^2 dM_{p\pi^+} dM_{\pi^+\pi^-} d\Omega_{\pi^-} d\alpha_{\pi^-}}, \quad (4.2.8)$$

697 where  $\Gamma_v$  is virtual photon flux, given by

$$\Gamma_v = \frac{\alpha}{4\pi} \frac{1}{E_{beam}^2 M_p^2} \frac{W(W^2 - M_p^2)}{(1 - \varepsilon)Q^2}, \quad (4.2.9)$$

698 where  $\alpha$  is the fine structure constant ( $1/137$ ),  $M_p$  is the proton mass, and  $\varepsilon$  is the virtual  
699 photon transverse polarization, given by

$$\varepsilon = \left( 1 + 2 \left( 1 + \frac{\omega^2}{Q^2} \right) \tan^2 \left( \frac{\theta_{e'}}{2} \right) \right)^{-1}, \quad (4.2.10)$$

700 where  $\omega = E_{beam} - E_{scattered\ electron}$  and  $\theta_{e'}$  is the angle of the scattered electron in the lab  
701 frame.  $W$ ,  $Q^2$  and  $\theta_{e'}$  are taken in the center of the bin.

702 Limited statistics does not allow to estimate the five-differential cross section with rea-  
703 sonable accuracy. Therefore, the five-differential hadronic cross sections obtained in each  
704 bin in  $W$  and  $Q^2$  are integrated in order to obtain the single-differential cross sections.

705 The following set of the single-differential cross sections are obtained for the second sets  
706 of variables mentioned in Sect. 4.1:

$$\begin{aligned} \frac{d\sigma}{dM_{\pi^+\pi^-}} &= \int \frac{d^5\sigma}{d^5\tau} d\tau_{M_{\pi^+\pi^-}}^4; & d\tau_{M_{\pi^+\pi^-}}^4 &= dM_{\pi^+p} d\Omega_{\pi^-} d\alpha_{\pi^-} \\ \frac{d\sigma}{dM_{\pi^+p}} &= \int \frac{d^5\sigma}{d^5\tau} d\tau_{M_{\pi^+p}}^4; & d\tau_{M_{\pi^+p}}^4 &= dM_{\pi^+\pi^-} d\Omega_{\pi^-} d\alpha_{\pi^-} \\ \frac{d\sigma}{d(-\cos\theta_{\pi^-})} &= \int \frac{d^5\sigma}{d^5\tau} d\tau_{\theta_{\pi^-}}^4; & d\tau_{\theta_{\pi^-}}^4 &= dM_{\pi^+\pi^-} dM_{\pi^+p} d\varphi_{\pi^-} d\alpha_{\pi^-} \\ \frac{d\sigma}{d\alpha_{\pi^-}} &= \int \frac{d^5\sigma}{d^5\tau} d\tau_{\alpha_{\pi^-}}^4; & d\tau_{\alpha_{\pi^-}}^4 &= dM_{\pi^+\pi^-} dM_{\pi^+p} d\Omega_{\pi^-} \end{aligned} \quad (4.2.11)$$

with  $d^5\tau = dM_{\pi^+\pi^-} dM_{\pi^+p} d\Omega_{\pi^-} d\alpha_{\pi^-}$ .

707 For the two other sets of variables from Sect. 4.1 the single-differential cross sections can be  
708 obtained in a similar way.

709 In the actual cross section calculations the integrals in (4.2.11) are substituted by respec-  
710 tive sums over the five-dimensional kinematical grid of hadronic cross sections.

711 To evaluate the absolute statistical error of the five-differential hadronic cross sections  
712 the following error propagation approach is used:

$$\delta_{stat}(M_{p\pi^+}, M_{\pi^+\pi^-}, \theta_{\pi^-}, \varphi_{\pi^-}, \alpha_{\pi^-}) = \frac{1}{F \cdot R} \frac{1}{\Gamma_v} \sqrt{\left( \frac{\Delta N_{full}}{Q_{full}^2} + \frac{\Delta N_{empty}}{Q_{empty}^2} \right)} \quad (4.2.12)$$

713 Another source of statistical fluctuations is connected to the limited statistics in the Monte  
714 Carlo simulation. From (4.2.6) it is clear that the uncertainty in the efficiency  $F$  is affecting

715 the cross section value. The definition of efficiency factor  $F$  is simple:

$$F = \frac{N_{rec}}{N_{gen}}, \quad (4.2.13)$$

716 where  $N_{gen}$  and  $N_{rec}$  are the numbers of Monte Carlo generated and reconstructed events,  
717 respectively.

718 Due to the fact that  $N_{gen}$  and  $N_{rec}$  are not independent the special approach needs to  
719 be applied in order to calculate the statistical error of efficiency. This approach is described  
720 in [34] and neglecting the events migration between the bins it gives the following expression  
721 for the absolute statistical error in  $F$

$$\delta(F) = \sqrt{\frac{(N_{gen} - N_{rec})N_{rec}}{N_{gen}^3}}. \quad (4.2.14)$$

722 It needs to be mentioned that kinematical cells where  $N_{rec} >= N_{gen}$  are treated as empty  
723 cells with no efficiency. Such cells are very rare and usually located near the edges of the  
724 invariant mass distributions where the cross section is close to zero.

725 The absolute error on the cross section due to the limited Monte Carlo statistic is given  
726 by

$$\delta_{stat,MC} = \frac{d\sigma}{dM_{\pi^+\pi^-} dM_{\pi^+p} d\Omega_{\pi^-} d\alpha_{\pi^-}} \left( \frac{\delta(F)}{F} \right) \quad (4.2.15)$$

727 Finally two statistical errors that come from fluctuation in the data and from the Monte  
728 Carlo are combined quadratically, so the total absolute statistical error is given by

$$\delta_{stat,tot} = \sqrt{\delta_{stat,MC}^2 + \delta_{stat}^2}. \quad (4.2.16)$$

### 729 4.3 Radiative corrections

730 The radiative corrections are done using the new double-pion event generator (see Iu. Sko-  
731 rodumina wiki page [35] and Sect 4.4). For that purpose double-pion events are generated  
732 with and without radiative effects. After that radiative correction factor  $R$  in formula (4.2.6)  
733 is determined by

$$R = \frac{N_{rad}^{2D}}{N_{norad}^{2D}}, \quad (4.3.1)$$

734 where  $N_{rad}^{2D}$  and  $N_{norad}^{2D}$  are the numbers of generated events in each  $(W, Q^2)$  bin with and  
735 without radiative effects, respectively. The quantity one over  $R$  is plotted on the left side of  
736 Fig. 4.7 as a function of  $W$  for various  $Q^2$  bins. As it can be seen in Fig. 4.7 the dependence  
737 of the radiative correction factor on  $Q^2$  is rather small. So, for the actual cross section  
738 calculations the factor  $R$  is averaged over all  $Q^2$  bins (see right side of Fig. 4.7). The

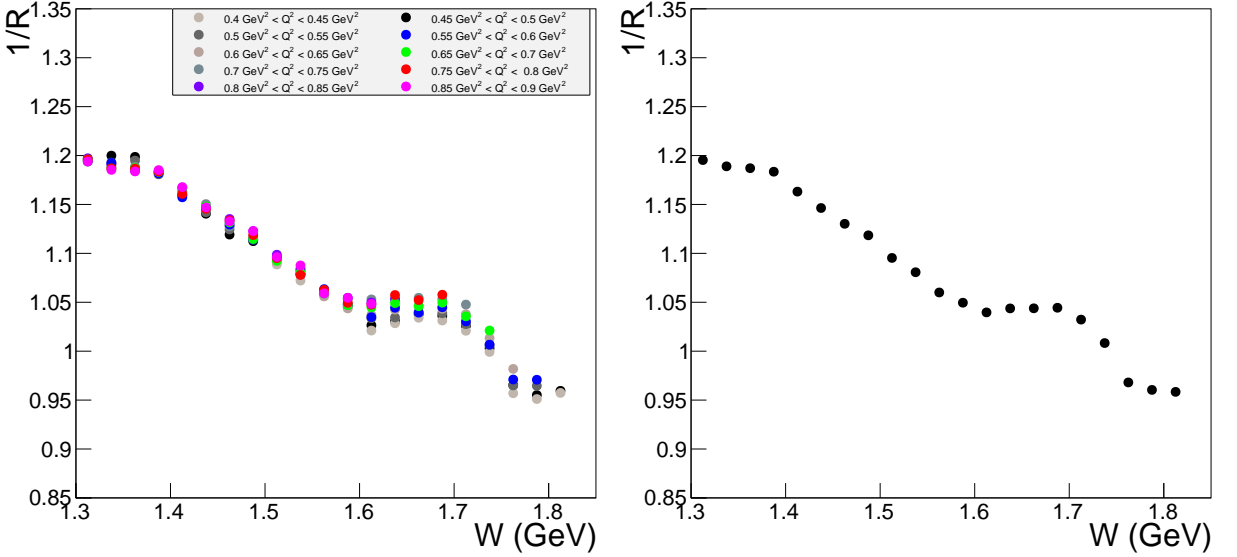


Figure 4.7: One over radiative correction factor (see formula 4.2.6) as function of  $W$ , for various bins over  $Q^2$  (left plot) and averaged over all  $Q^2$  bins (right plot).

739 statistical uncertainties associated with the number of generated events are also small and  
 740 not seen in Fig. 4.7.

741 It should be noted that to account for radiative effects, the new double-pion event gen-  
 742 erator uses the well known approach taken from Mo and Tsai [31]. In this approach the soft  
 743 part is evaluated explicitly, while for the calculation of the hard part the "inclusive" hadronic  
 744 tensor is used. The applicability of this approximation for the hard part of radiative effects  
 745 is subject of special attention. The single-differential double-pion cross sections (4.2.11)  
 746 obtained in this analysis represent the over four variables integrated five-differential cross  
 747 sections. This integration considerably reduces the influence of the final hadron kinematics  
 748 on the radiative correction factor. Therefore, the "inclusive" Mo and Tsai procedure is in  
 749 the case of double-pion cross sections more applicable than in a case of non-integrated cross  
 750 sections that are typically obtained for instance in the single-pion data analysis.

751 It also should be mentioned that this correction should be applied before the empty cells  
 752 (see Sect. 4.5) are filled, since the cross sections that are used for the purpose of filling empty  
 753 cells are already corrected for radiative effects.

## 754 4.4 Efficiency evaluation

755 For the efficiency calculation the Monte Carlo event generator of the Genova group is used.  
 756 This event generator uses the JM05 model [36] for double-pion channel. Although the cross

sections on which the event generator is based do not include the latest modifications of the JM model [7–9], it describes the data well enough to use it for the purpose of the efficiency evaluation.

To take into account the multi-pion background, three-pion events are generated simultaneously with the double-pion ones, the relative weight of these two channels is determined according to their integral cross sections at the photon point, see Fig. 4.8. The event generator does not assume any model for the channel  $ep \rightarrow e'p'\pi^+\pi^-\pi^0$ , so for this channel phase space distributions are generated. It needs to be mentioned that even at high  $W$  (around 1.8 GeV) three-pion background contributes only few percent to the double-pion events that survive after the exclusivity cut (see Sect. 3.4).

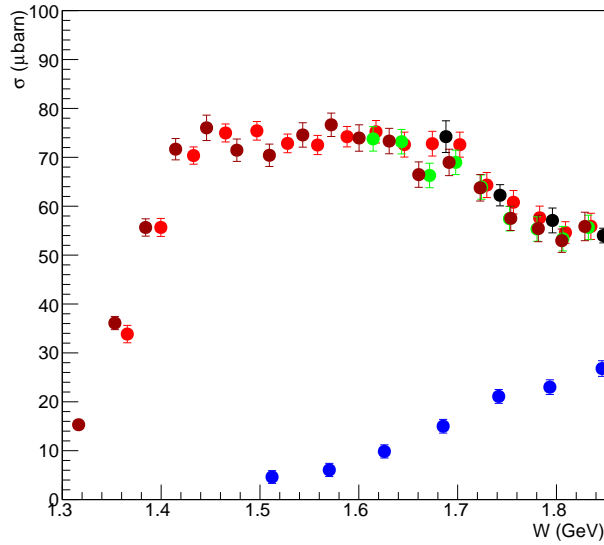


Figure 4.8: Integral cross sections of the reactions  $ep \rightarrow e'p'\pi^+\pi^-$  and  $ep \rightarrow e'p'\pi^+\pi^-\pi^0$  at the photon point. Black and red circles are double-pion data from [32]. Green and brown circles are double-pion data from [37]. Blue circles are three-pion data from [38].

All generated events are passed through GSIM, GPP and RECSIS. The parameters for the simulation are taken to be the same as in [39]. After applying all cuts and corrections described above, the reconstructed events are compared with the data. As it is seen on the left side of Fig. 4.9 MC reconstructed events reproduce the data rather well.

On the right side of Fig. 4.9 the average efficiency in five-dimensional kinematical cell is shown as functions of the hadron variables that describe the double-pion final state. No distributions show any significant efficiency variation.

The efficiency in some five-dimensional cells is not determined precisely enough, this leads to the fact that the cross sections obtained in them are not reliable. These cells should be excluded from the analysis and treated as empty cells (see Sect. 4.5). In order to determine

777 the criterion for cell exclusion the distribution shown in Fig. 4.10 is produced. This figure  
 778 shows the relative efficiency error (absolute efficiency error is given by 4.2.14) that is plotted  
 779 versus efficiency, color code in this figure represents the number of five-dimensional cells. As  
 780 it is seen in Fig. 4.10 cells with relative efficiency errors greater than 30% are clustered along  
 781 horizontal stripes. This effect can be explained taking into account that efficiency is obtained  
 782 by division of two integer numbers, and it indicates too small statistics of generated events  
 783 that in turn leads to higher efficiency errors. Moreover these horizontal stripes contain many  
 784 cells with extremely small efficiency values that one can not count on anyway. Therefore, the  
 785 five-dimensional cells that are located above the horizontal red line in Fig. 4.10 are excluded  
 786 from the analysis and treated as empty cells (see Sect. 4.5).

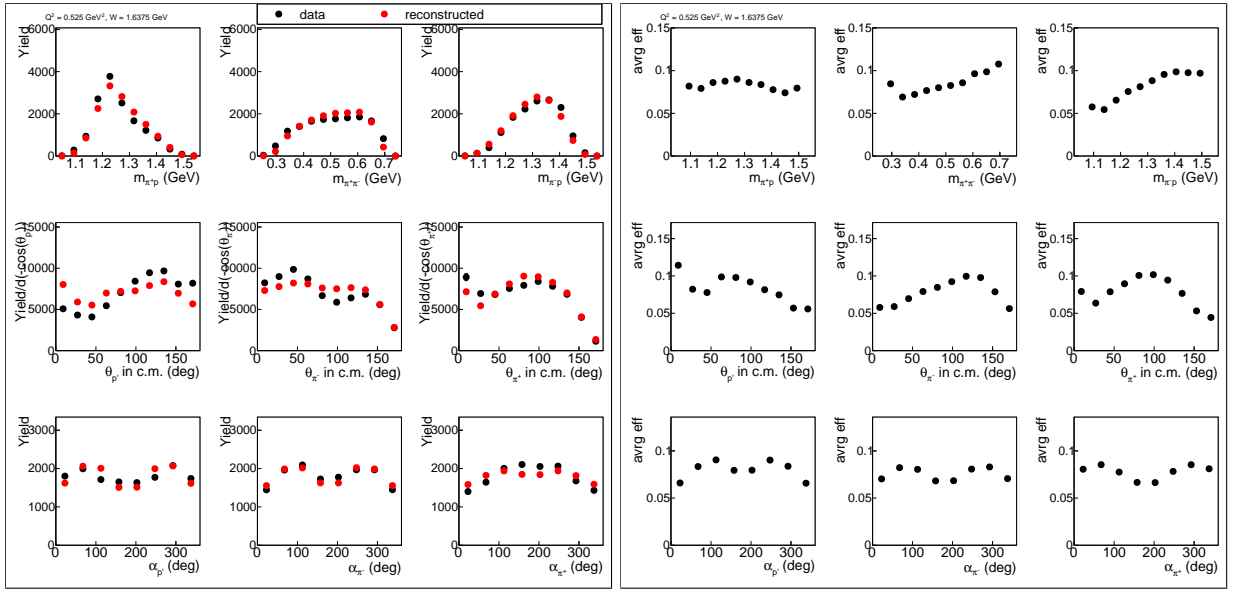


Figure 4.9: Plots in the left frame show the comparison of data and reconstructed MC yields as functions of various hadronic variables that describe the double-pion final state. Plots in the right frame show the average efficiency in the five-dimensional kinematical cell as functions of the final state hadronic variables. All distributions are given for one particular bin in  $W$  and  $Q^2$  ( $W = 1.6375 \text{ GeV}$ ,  $Q^2 = 0.525 \text{ GeV}^2$ ).

## 787 4.5 Filling kinematical cells with zero acceptance

788 Since the CLAS detector does not cover full  $4\pi$  solid angle, there are some blind areas  
 789 or so-called "empty cells" in the kinematic phase space of the double-pion production. In  
 790 the case when fully differential cross sections are obtained (for example in single pion  
 791 production analyses) the presence of these cells is not a problem of big importance. Due to  
 792 the statistical limitations in the double-pion analyses only the single-differential cross sections

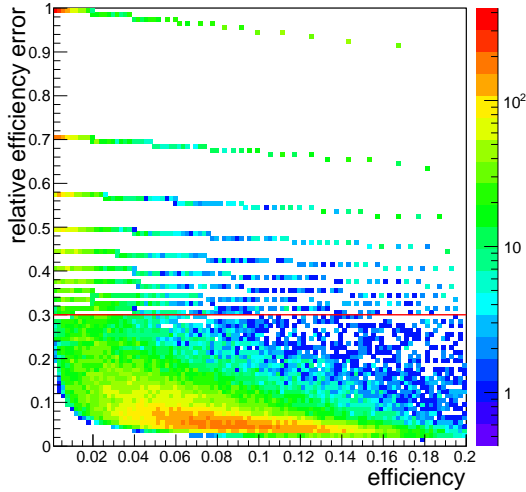


Figure 4.10: Relative efficiency error versus efficiency for one particular bin in  $W$  and  $Q^2$  ( $W = 1.6375$  GeV,  $Q^2 = 0.525$  GeV $^2$ ). Color code shows the number of five-dimensional cells.

793 can be obtained. It means that the five-differential cross sections need to be integrated over  
 794 four variables (see formulae 4.2.11). To obtain correct integrals, some assumptions on the  
 795 cross sections in the empty cells are needed. It makes the problem of filling empty cells a  
 796 point of special attention.

797 The map of the empty cells is determined by the Monte Carlo simulation. A cell is  
 798 treated as empty, if it contains generated events, but does not contain any reconstructed  
 799 events. One should not confuse these cells with those that contain both generated and  
 800 reconstructed events, but do not contain data. The latter do not contain real events due to  
 801 the limited experiment duration, and should not be filled since normalization on the charge  
 802 in Faraday cup is applied.

803 To consider contributions from empty cells to the integrals (4.2.11) in detail model as-  
 804 sumptions on the cross sections in these cells are needed. Recently for the purpose of the  
 805 development of new double-pion event generator [35] a special procedure that allows to ob-  
 806 tain the five-differential double-pion cross sections in the given kinematical cell was worked  
 807 out. This procedure employs the five-differential cross sections from the recent version of  
 808 the JM15 model fit to all results on charged double pion photo- and electroproduction cross  
 809 sections from CLAS (both published and preliminary [1, 6, 7, 40]). In the area not yet  
 810 covered by CLAS data an additional extrapolation technique was applied, that included  
 811 additional world data on  $W$  dependencies of double-pion photoproduction integrated cross  
 812 sections [32, 37]. The set of the cross sections obtained using this procedure was used for  
 813 the purpose of filling empty cells in this analysis.

814 In Fig. 4.11 the single-differential cross sections are plotted for the two cases: when empty  
 815 cells are not filled (red circles) and when empty cells are filled by the way described above

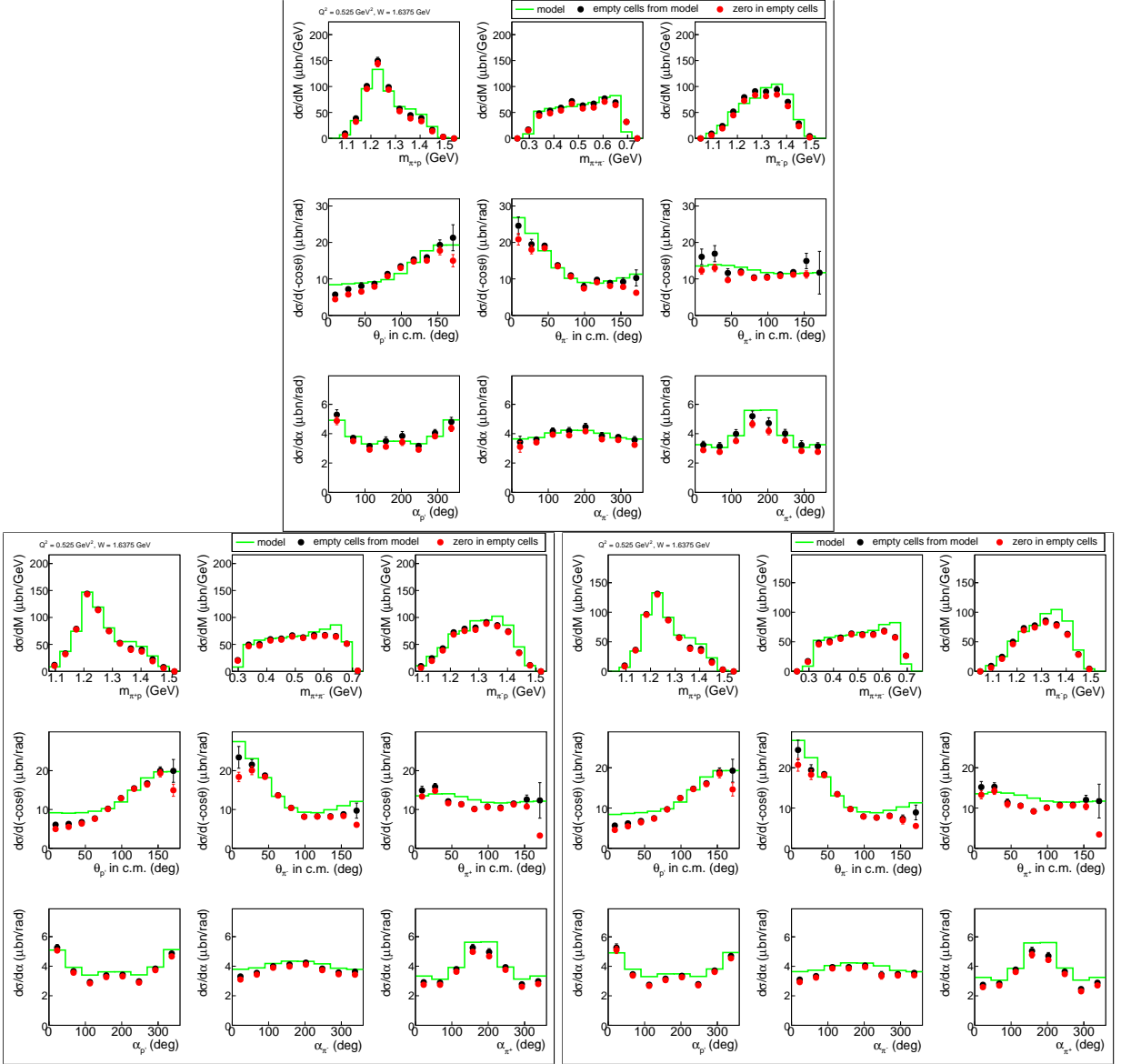


Figure 4.11: Comparison of various ways of combining topologies. Plots in the top frame are for the case when the cross sections are obtained using the topology where  $\pi^-$  is missing combined with the exclusive topology. Plots in the bottom left frame are for the case when the cross sections are obtained using the sum of data and reconstructed events for all four topologies. Plots in the bottom right frame are for the case when the cross sections are obtained using the selection of five-dimensional cells based on the maximum efficiency. See text for more details. In all plots the red circles are for the cross sections with unfilled empty cells and the black circles are for the cross sections with filled empty cells. Green curves show the cross sections that are used for the purpose of filling empty cells. All distributions are given for one particular bin in  $W$  and  $Q^2$  ( $W = 1.6375 \text{ GeV}$ ,  $Q^2 = 0.525 \text{ GeV}^2$ ).

816 (black circles). The cross sections that are used to fill empty cells are shown by the green  
817 curves. The plot in the top frame of Fig. 4.11 corresponds to the topology where  $\pi^-$  is missing  
818 combined with the exclusive topology, while the two plots in the bottom frames correspond  
819 to different ways of combining of all available topologies (ways in which the topologies may  
820 be combined are described in more detail in Sect. 4.6).

821 The plot in the left bottom frame in Fig. 4.11 corresponds to the method of the topologies  
822 combination that is selected to be the best. As it can be seen in the left bottom frame in  
823 Fig. 4.11 the contribution from empty cells to the total cross sections is reasonably small.  
824 Although the cross sections that are used to fill empty cells describe the data well an ad-  
825 dditional 50% relative error is assigned to the part of the cross section that comes from the  
826 empty cell contributions. For finally obtained cross sections (shown by black circles) this  
827 additional error is combined with the total statistical one.

## 828 4.6 Combination of various topologies

829 It is mentioned in Sect. 3.4 that the topology where  $\pi^-$  is missing combined with the exclusive  
830 one accounts about 80% of all double-pion events. In previously published analyses [6, 41]  
831 only these two topologies were used to obtain final cross sections.

832 In this analysis it is found that the use of only the combination of the exclusive and  
833  $\pi^-$  missing topologies leads to significant contributions from empty cells to the total cross  
834 sections in some phasespace regions (see plot in the top frame of Fig. 4.11). Moreover, the  
835 last point in  $\theta_{\pi^+}$  angular distribution does not contain data at all and the cross section in this  
836 point is totally determined by the procedure of filling empty cells as described in Sect. 4.5.

837 Hence to minimize the part of the cross section that comes from filling of the empty cells  
838 and therefore the model dependence of the obtained cross sections, it was decided to use all  
839 available topologies.

840 There are two methods in which topologies can be combined. One of them is chosen as  
841 preferable and used to obtain the final cross sections. In this method data events for all  
842 topologies are summed up in each five-dimensional kinematical cell. The same is done for  
843 the reconstructed events, while the number of generated events remains the same. Then  
844 the cross sections are calculated in a usual way. The cross sections for the case when all  
845 topologies are combined by this method are shown in the bottom left frame of Fig. 4.11.  
846 One can see that the usage of this method allows to minimize the part of the cross section  
847 that comes from the empty cells contributions in comparison with the case when only the  
848 exclusive and  $\pi^-$  missing topologies are used. Moreover even the last point in  $\theta_{\pi^+}$  angular  
849 distribution now is partially determined by data and therefore less model dependent.

850 Another way to combine topologies is used to check the consistency of the results. In this  
851 way in each five-dimensional kinematical cell reconstructed and data events are taken from

852 the topology that has maximum efficiency, while the number of generated events remains the  
853 same. The cross sections that are obtained using this method are shown in the bottom right  
854 frame of Fig. 4.11. Although this method gives almost the same result as the previous one,  
855 it has several shortcomings. One of them is slightly bigger contribution from empty cells.  
856 Another one is the fact that this method does not allow to use the whole available statistics  
857 of the data. As a result the error of the obtained cross sections becomes a little bit higher  
858 than in the previous method. That is why this method is not chosen as a primary one. The  
859 difference between the cross sections obtained by the two methods described above is used  
860 as part of the systematical error of the integrated cross sections (see Sect. 6.2).

861 Finally it needs to be mentioned that independently of the way the cross sections are  
862 calculated (see all plots in Fig. 4.11), the final cross sections obtained after filling the empty  
863 cells are very close to each other. That indicates the stability and reliability of the cross  
864 section extraction procedure.

865 **Chapter 5**

866 **Correction for binning effects**

867 Since the bins in which the cross sections are obtained have finite sizes, the cross section  
868 values can be distorted due to the averaging within the bins. For instance, if there is a  
869 sharp peak in the middle of a bin, then the average value of the cross section in that bin  
870 will always be smaller than the peak value. Any non-linear behavior of the cross section will  
871 likely result in an offset of the obtained value. There are two ways to deal with this issue.  
872 Either one uses the corrected values of the kinematical quantities associated with the bin,  
873 instead of the central values or one calculates the correction to the cross section in the center  
874 of the bin. In this analysis the second method is chosen, in order to keep the initial binning  
875 over kinematical variables. For that purpose some model assumption about the cross section  
876 behavior is needed. The ratio of the model value at the center of the bin to the model value  
877 averaged within the bin is considered as a multiplicative correction factor, and the corrected  
878 cross section is found as

$$\begin{aligned}\sigma_{corr} &= \sigma_{uncorr} \times C_{bin} \quad \text{with} \\ C_{bin} &= \frac{\sigma_{model,cntr}}{\sigma_{model,avg}},\end{aligned}\tag{5.0.1}$$

879 where  $\sigma_{uncorr}$  is the experimental cross section value before binning corrections,  $\sigma_{model,cntr}$   
880 is the cross section from the model in the center of the data bin, and  $\sigma_{model,avg}$  is the cross  
881 section from the model averaged in data bin.

882 In the first step the corrections are applied to all single-differential cross sections. For  
883 the model cross sections the cubical spline approximation is chosen. The results are shown  
884 in Fig. 5.1. The black and red points in this figure stand for the cross sections before  
885 and after binning corrections, respectively, while the curves correspond to the model. For  
886 the invariant masses and  $\theta$  angular distributions splines are forced to pass through the  
887 intermediate points that are obtained by averaging of two neighboring cross section points.  
888 This method reduces the splines sensitivity to accidental cross section fluctuations. For the  
889  $\alpha$  distributions another method is chosen. As it seen in Fig. 4.11 the obtained  $\alpha$  distributions  
890 are slightly asymmetrical. However after the integration over  $\varphi$ , the cross section must be

891 symmetrical with respect to the  $\alpha$  angle. Therefore, for  $\alpha$  distributions it was decided to  
 892 average the cross section values in the points that are symmetrical with respect to  $\alpha = 180^\circ$ .  
 893 After that all  $\alpha$  distributions become ideally symmetrical and their statistical errors become  
 894 smaller. Then  $\alpha$  distributions are fit with cubical splines and the binning corection procedure  
 895 described above is applied.

896 After that the corrected single-differential cross sections are integrated and corrected to  
 897 the  $Q^2$  dependence inside the  $Q^2$  bins and the  $W$  dependence inside the  $W$  bins. In Fig. 5.2  
 898 integrated cross sections are shown as functions of  $Q^2$  (left plot) and  $W$  (right plot) before  
 899 (black points) and after (red points) binning corrections. To fit the  $Q^2$  dependencies a  
 900 second order polynom is chosen, while for  $W$  distributions cubical splines are the best choice  
 901 (splines are forced to pass through the intermediate points that are obtained by averaging two  
 902 neighboring cross section points). These assumptions for  $Q^2$  and  $W$  cross sections behaviors  
 903 are shown by the curves in Fig. 5.2.

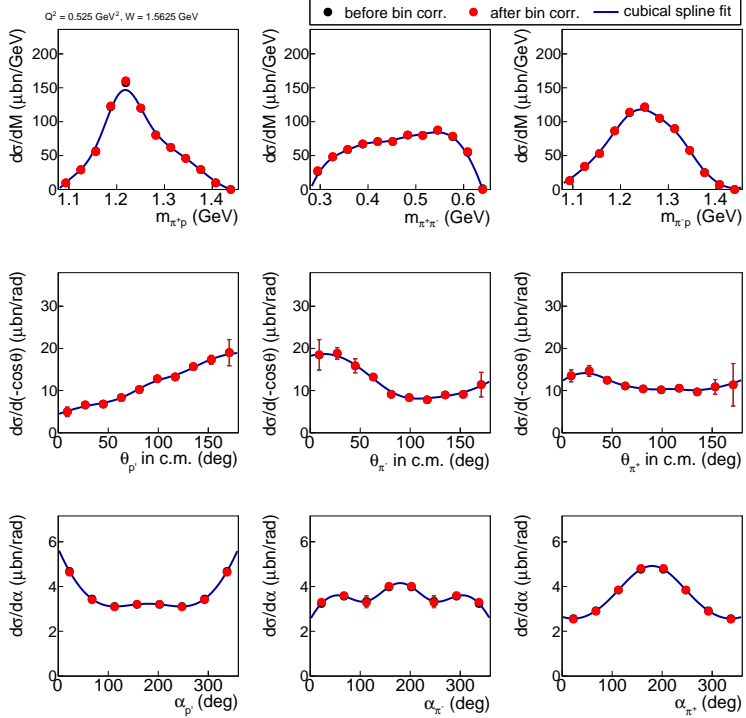


Figure 5.1: The single-differential cross sections as functions of the final hadron variables for one particular bin in  $W$  and  $Q^2$  ( $W = 1.5625 \text{ GeV}$ ,  $Q^2 = 0.525 \text{ GeV}^2$ ) before (black points) and after (red points) the binning corrections. Curves stand for the cubical spline approximation.

904 Since in this analysis the detailed binning over all kinematical variables is chosen, the  
 905 effect of the binning correction is rather small ( $\sim 1\%$ ) and only in some points at low  $W$   
 906 it can rise up to 4%. That is why in the Figs. 5.1 and 5.2 the black points (before the  
 907 correction) are almost completely covered up by the red ones (after the correction).

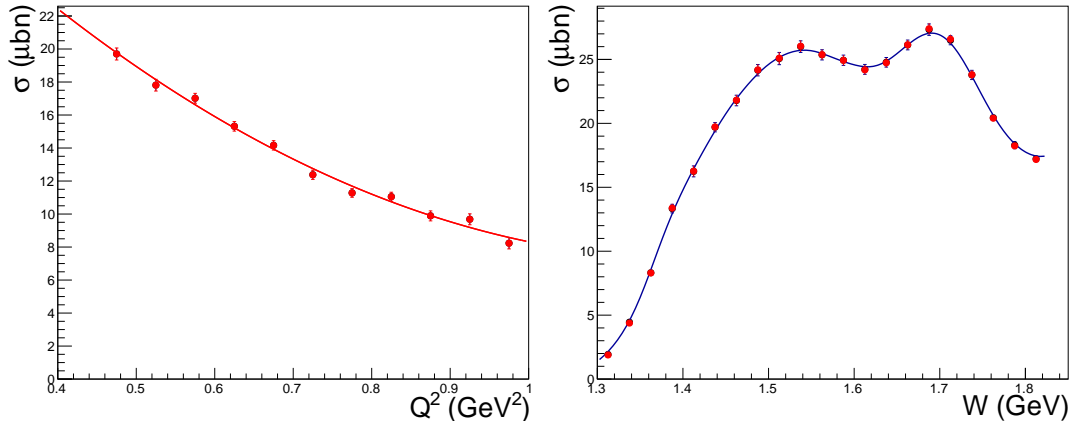


Figure 5.2:  $Q^2$  dependence of integral cross section at  $W = 1.4625 \text{ GeV}$  (left plot) and  $W$  dependence of integral cross section at  $Q^2 = 0.475 \text{ GeV}^2$  (right plot). On both plots black and red points correspond to the cross sections before and after the binning corrections, respectively. The curve on the left plot represents the second order polinomial fit, while the curve on the right plot correspond to the cubical spline approximation.

<sub>908</sub> **Chapter 6**

<sub>909</sub> **Systematical errors**

<sub>910</sub> **6.1 Errors due to normalization, electron identifica-**  
<sub>911</sub> **tion, and electron detection efficiency**

<sub>912</sub> One of the main sources of systematical errors in this experiment is the uncertainty in  
<sub>913</sub> the normalization. This can arise from miscalibrations of the Faraday cup, target density  
<sub>914</sub> instabilities, and errors in determining the target length and its temperature, DAQ live-time,  
<sub>915</sub> and other factors. However, the presence of the elastic events in the data set allows to check  
<sub>916</sub> the normalization of the cross sections by comparing the elastic cross sections to the world  
<sub>917</sub> data. In this way one can combine normalization, electron detection, electron tracking,  
<sub>918</sub> and electron identification errors into one global uncertainty factor. In Fig. 6.1 the ratio of  
<sub>919</sub> the measured elastic cross section to a parametrization of the elastic cross sections [42] is  
<sub>920</sub> shown. The parametrized cross sections are "radiated" and the elastic cross sections from  
<sub>921</sub> the CLAS data are not corrected for radiative effects. As it is seen in Fig. 6.1, all the points  
<sub>922</sub> are within the green lines that indicate  $\pm 5\%$  offsets. This procedure allows to assign a 3%  
<sub>923</sub> global uncertainty due to normalization, electron identification, and electron efficiency.

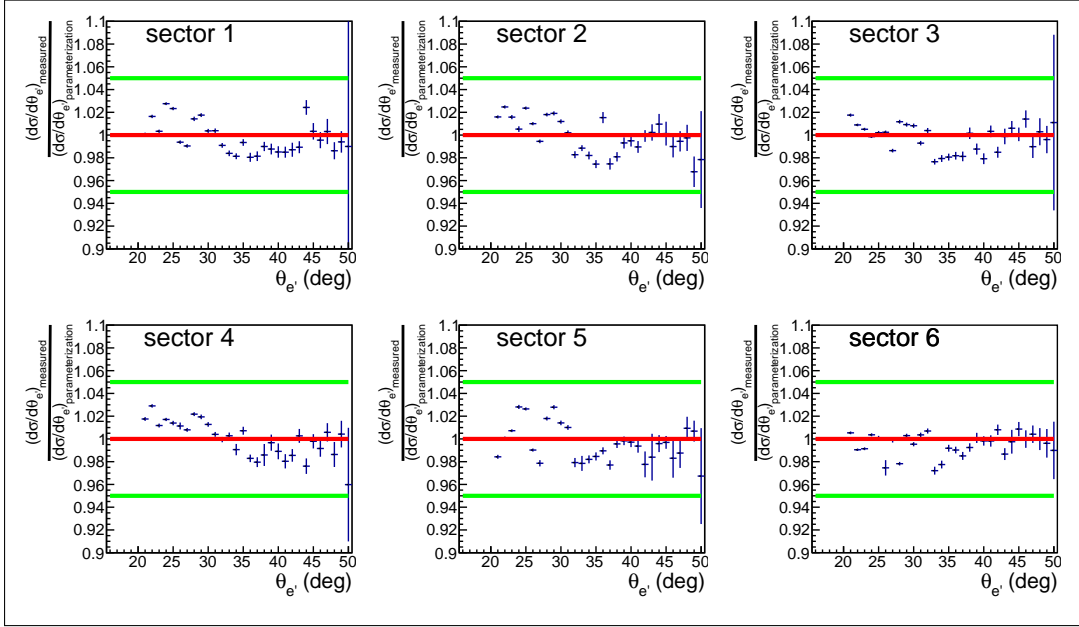


Figure 6.1: Ratio of the elastic cross section to the parametrization [42], plotted versus  $\theta_{e'}$  angle of the electron in the lab frame for the six CLAS sectors. Red lines correspond to unity and green lines indicate a  $\pm 5\%$  deviation from the parametrization.

## 924 6.2 Errors due to the different ways of combining 925 topologies

926 In this analysis two ways of combining topologies are used (see Sect. 4.6). The integrated  
927 cross sections obtained in these two ways are slightly different. As in the case of the integration  
928 over different kinematical grids, this difference is interpreted as systematical error.  
929 Since different topologies correspond to the different registered final hadrons (and therefore  
930 to the different hadron cut combinations) this systematical error includes partially the error  
931 due to the shapes of the cuts that are used in the analysis. The error is calculated for each  
932 bin in  $W$  and  $Q^2$  and typically is of the order of 2%.

## 933 6.3 Errors due to the integration over different final 934 hadron variables

935 As it is mentioned in Sect. 4.1 three sets of kinematical variables are used in this analysis. The  
936 cross sections obtained by integration over these three kinematical grids should be the same.  
937 However, it is found that they are slightly different due to the fact that data and efficiency  
938 propagate differently to the different kinematical grids. This difference is interpreted as

939 systematical error and computed for each bin in  $W$  and  $Q^2$ . This systematic effect varies  
940 depending on the bin in  $W$  and  $Q^2$  and is typically of the order of 5%.

## 941 6.4 Systematical error summary

942 As final integrated cross sections, the cross sections that are averaged over three grids of the  
943 kinematical variables are reported (see Fig. 6.2). In Fig. 6.2 the systematical uncertainties  
944 are shown as the red bands at the bottom of each plot. This uncertainties include the errors  
945 due to the effects mentioned above and extra 5% global error due to the inclusive radiative  
946 corrections procedure (see Sect. 4.3). To obtain the red bands all the errors are summed up  
947 in quadrature.

948 The statistical cross section uncertainties are typically smaller than the systematical ones.  
949 The total uncertainty is obtained as the sum of the systematical and statistical ones and is  
950 shown by the hatched red areas in Fig. 6.2.

951 The typical values of the integral systematical errors with their sources are presented in  
952 Tab. 6.1.

Error source	Error value
Normalization, electron id, and electron detection efficiency	3%
Different ways of combining topologies	$\sim 2\%$
Integration over different final hadron variables	$\sim 5\%$
Radiative corrections	5%

Table 6.1: The typical values of the integral systematical errors.

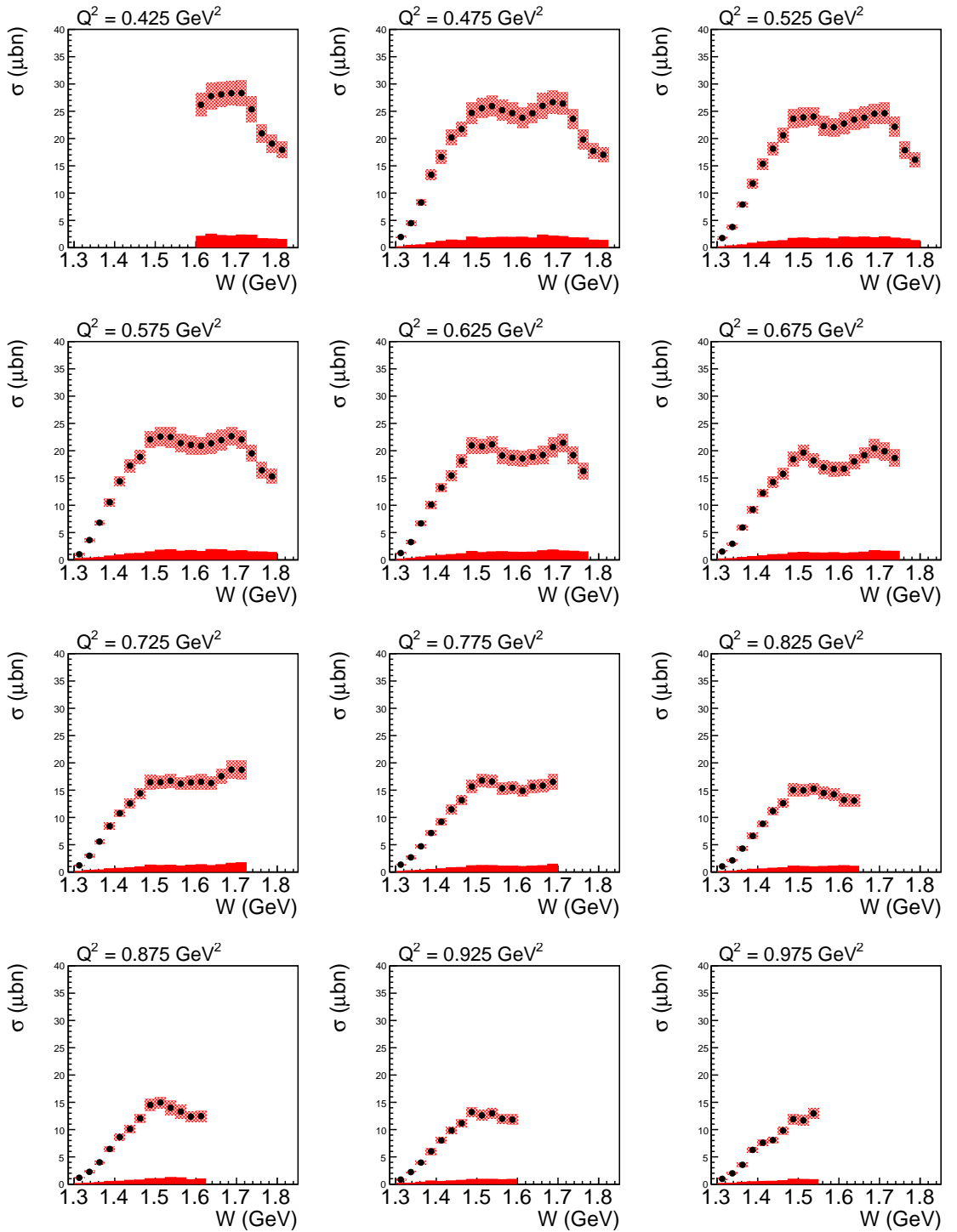


Figure 6.2: Systematical errors of the integrated cross sections. The plots show  $W$  dependencies of the integrated cross section in various bins in  $Q^2$ . The systematical uncertainties are shown as the red bands at the bottom of each plot. The total cross section uncertainty (both statistical and systematical ones summed up in quadrature) is shown by the hatched red areas.

<sub>953</sub> **Chapter 7**

<sub>954</sub> **Conclusions**

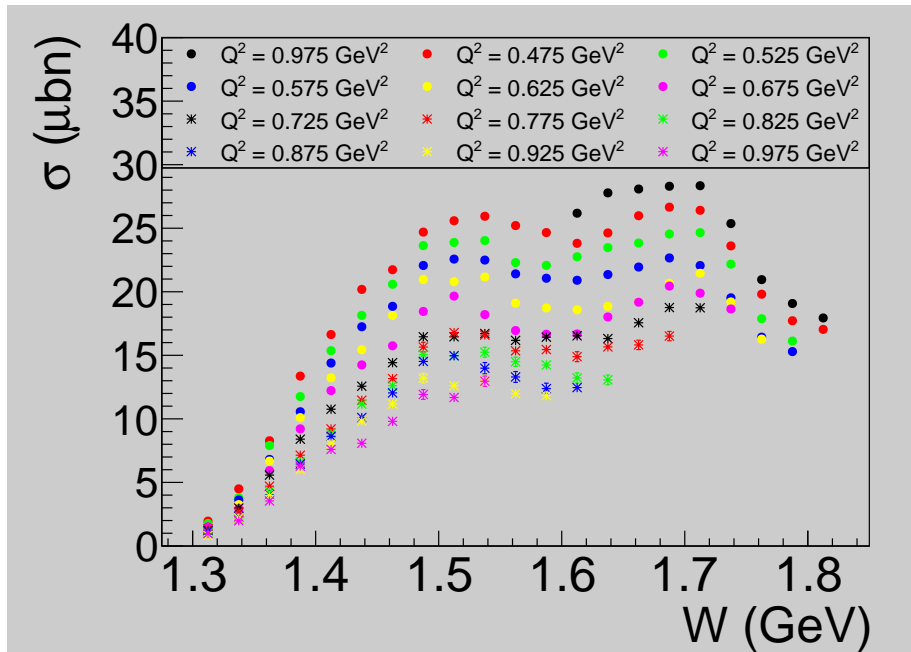


Figure 7.1:  $W$  dependencies of the integrated cross sections for various bins in  $Q^2$ . The statistical errors are small and invisible under the symbols.

- <sub>955</sub> • The complete set of the single-differential (see appendix A) and integrated cross sections (see Fig. 7.1) for the reaction  $\gamma_vp \rightarrow p\pi^+\pi^-$  is obtained in the range of  $W$  from <sub>956</sub> 1.3 GeV to 1.825 GeV and  $Q^2$  from 0.45  $\text{GeV}^2$  to 1  $\text{GeV}^2$ . The  $Q^2$  binning of the cross sections in the kinematical area of high-lying nucleon resonances is six times finer than <sub>957</sub> in previously available data.  
<sub>958</sub>

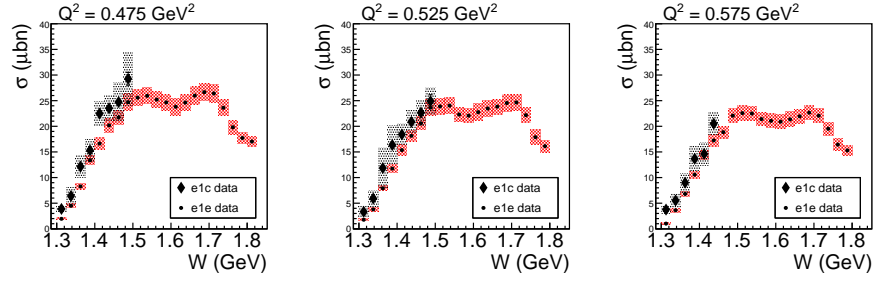


Figure 7.2:  $W$  dependencies of the obtained in this analysis cross sections (e1e dataset) in comparison with the cross sections from [6] (e1c dataset) for three bins in  $Q^2$ . Hatched areas correspond to the total uncertainties (sistemtical and statistical).

- 960 • The comparison of the obtained cross sections with the available ones [6] shows the  
961 reasonable agreement within the statistical uncertainties (see Fig. 7.2). It needs to be  
962 mentioned that this comparison is not fully justified since the cross sections from [6]  
963 and this analysis are obtained with different beam energies.
- 964 • The fit of these data by the meson-baryon reaction model JM [7–9] will provide for the  
965 first time information on the  $Q^2$  evolution of high-lying resonances with very detailed  
966 binning.

<sup>967</sup> **Appendix A: Measured cross sections**

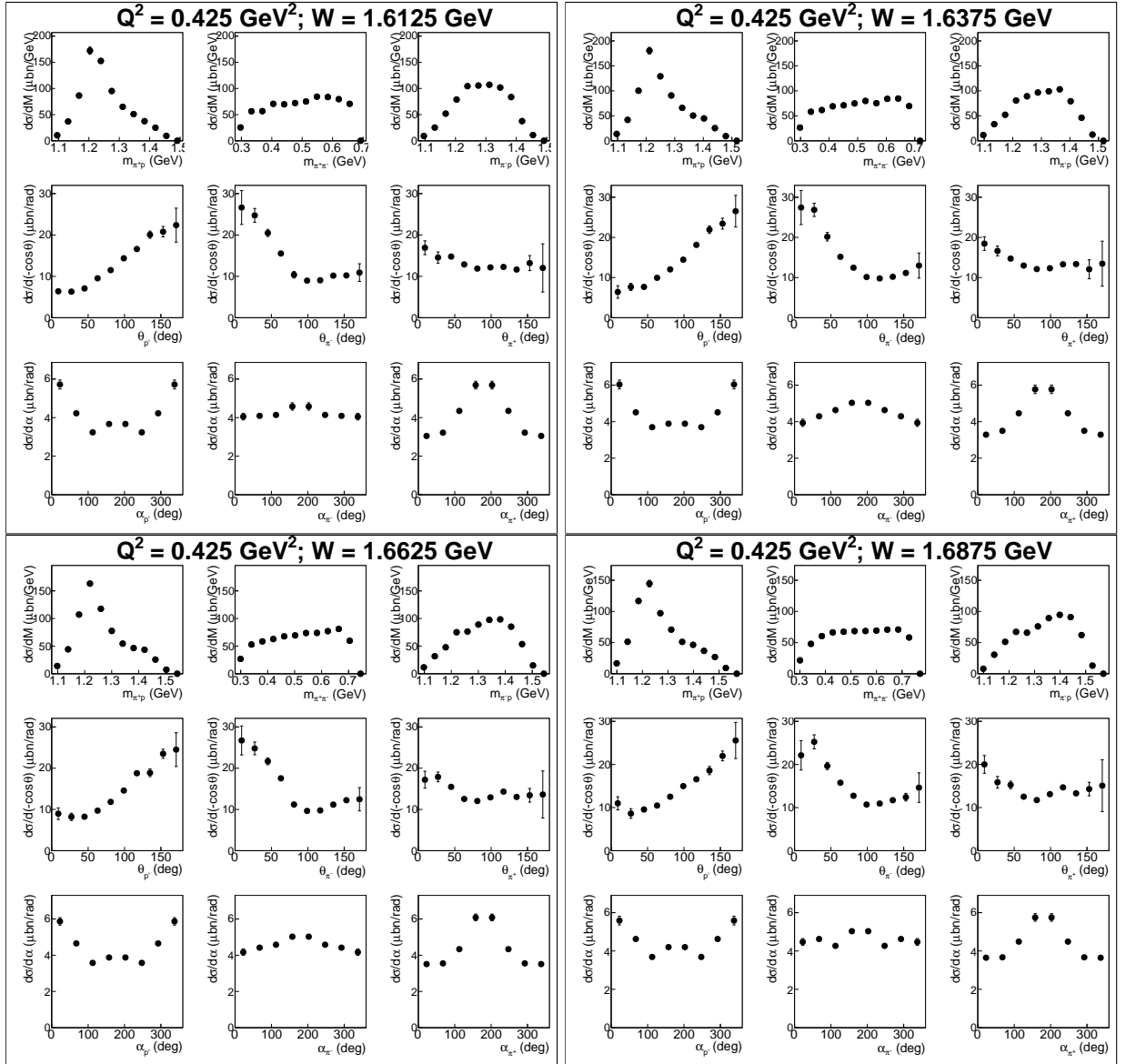


Figure A.1:

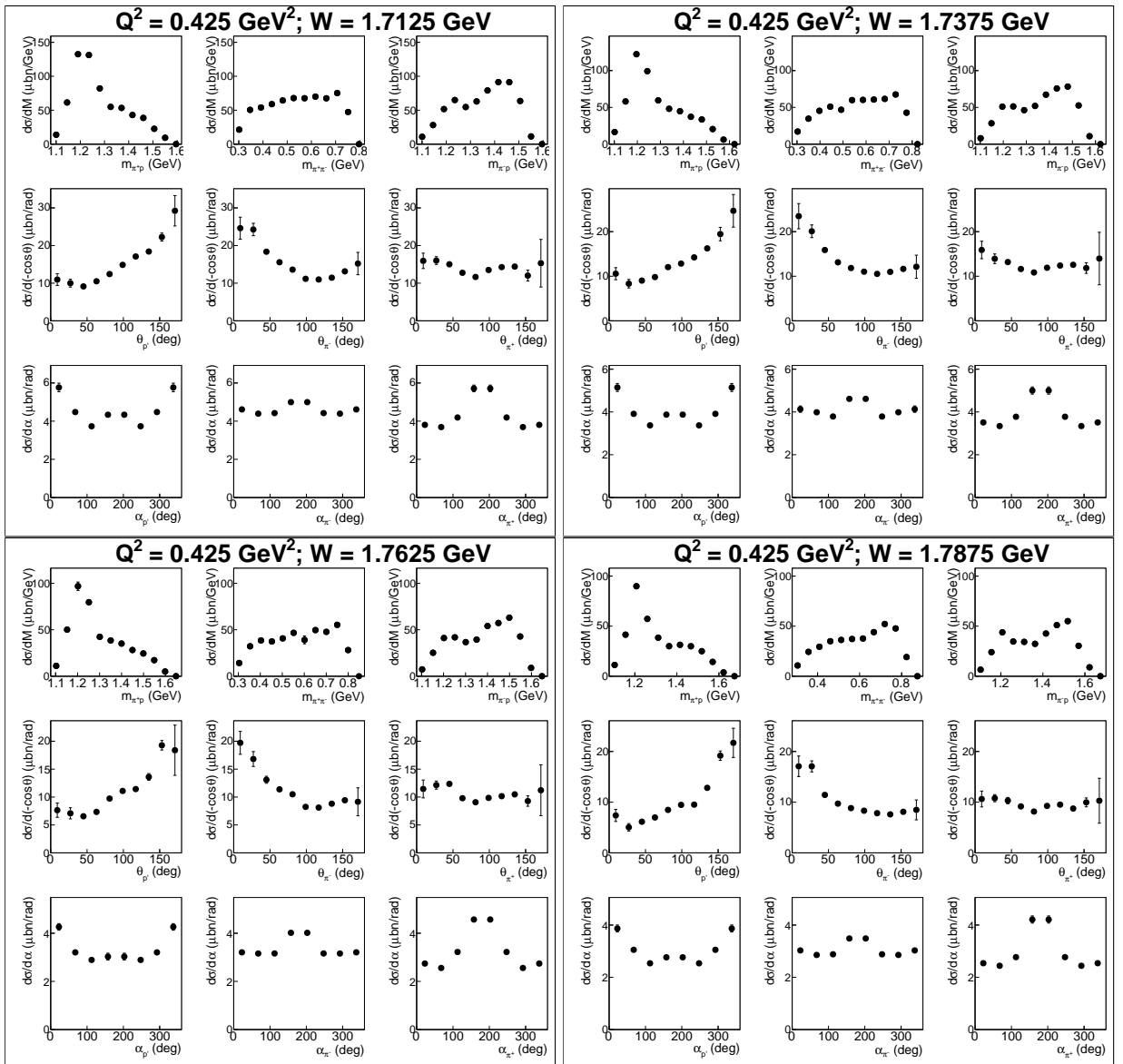


Figure A.2:

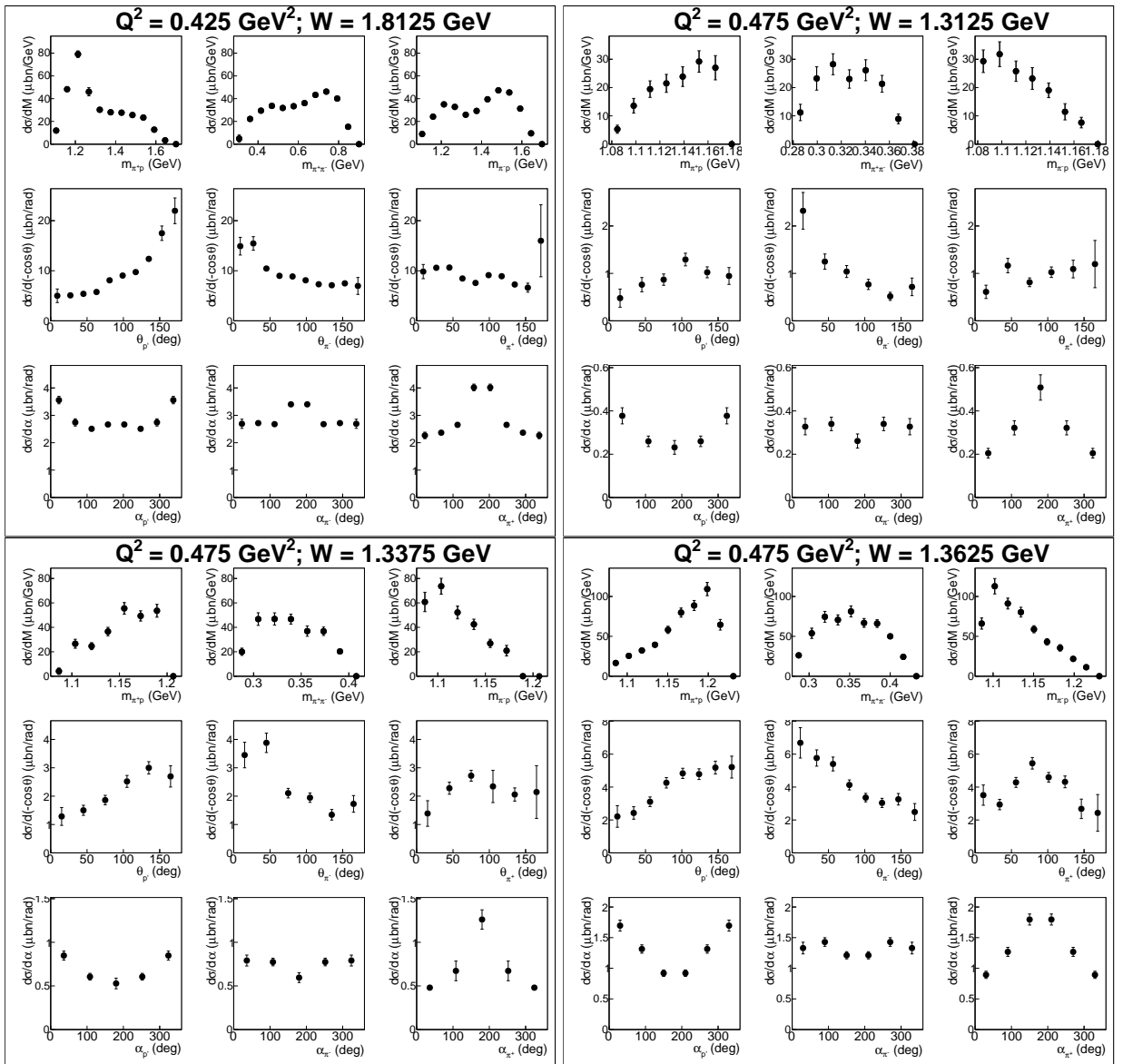


Figure A.3:

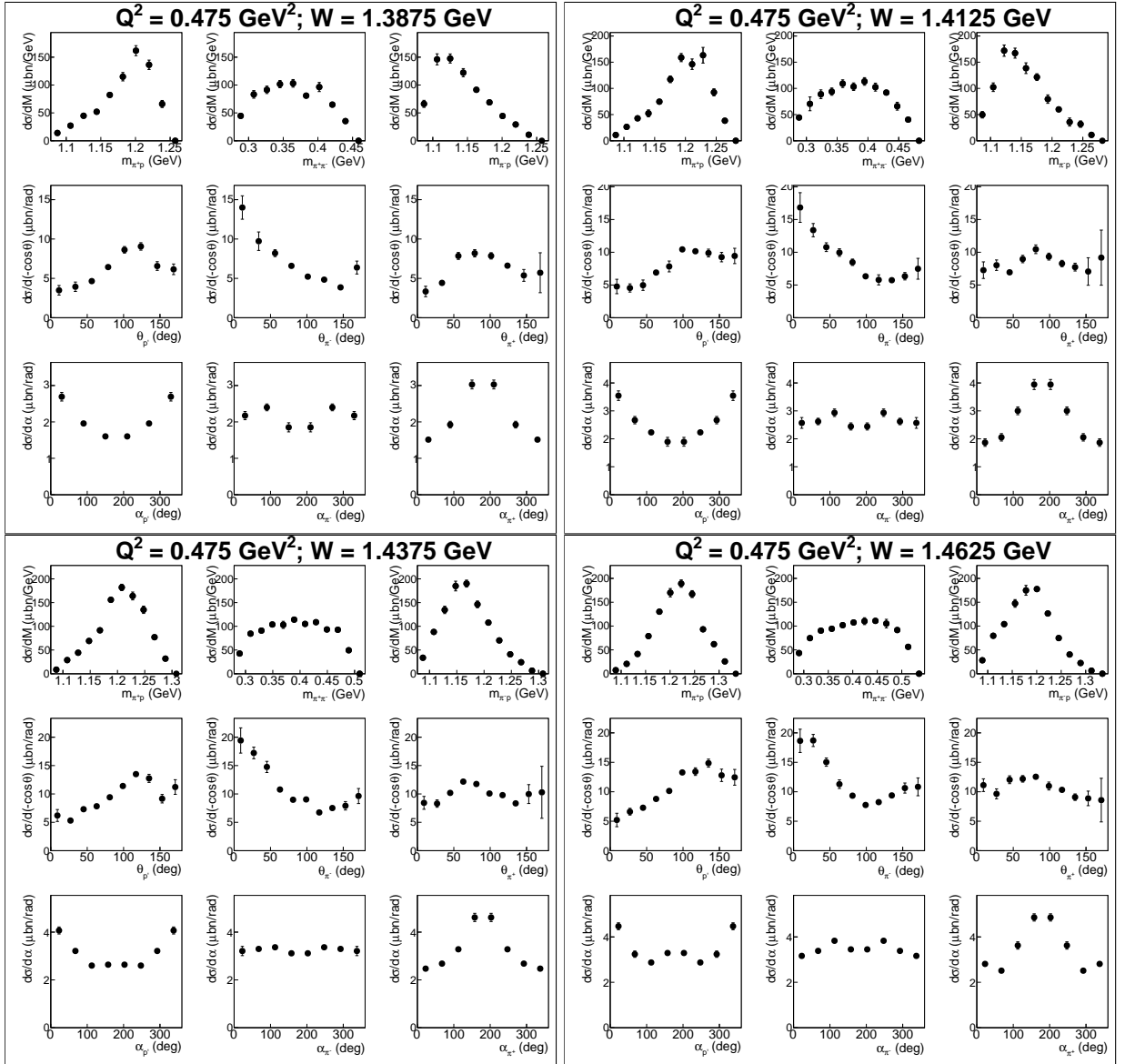


Figure A.4:

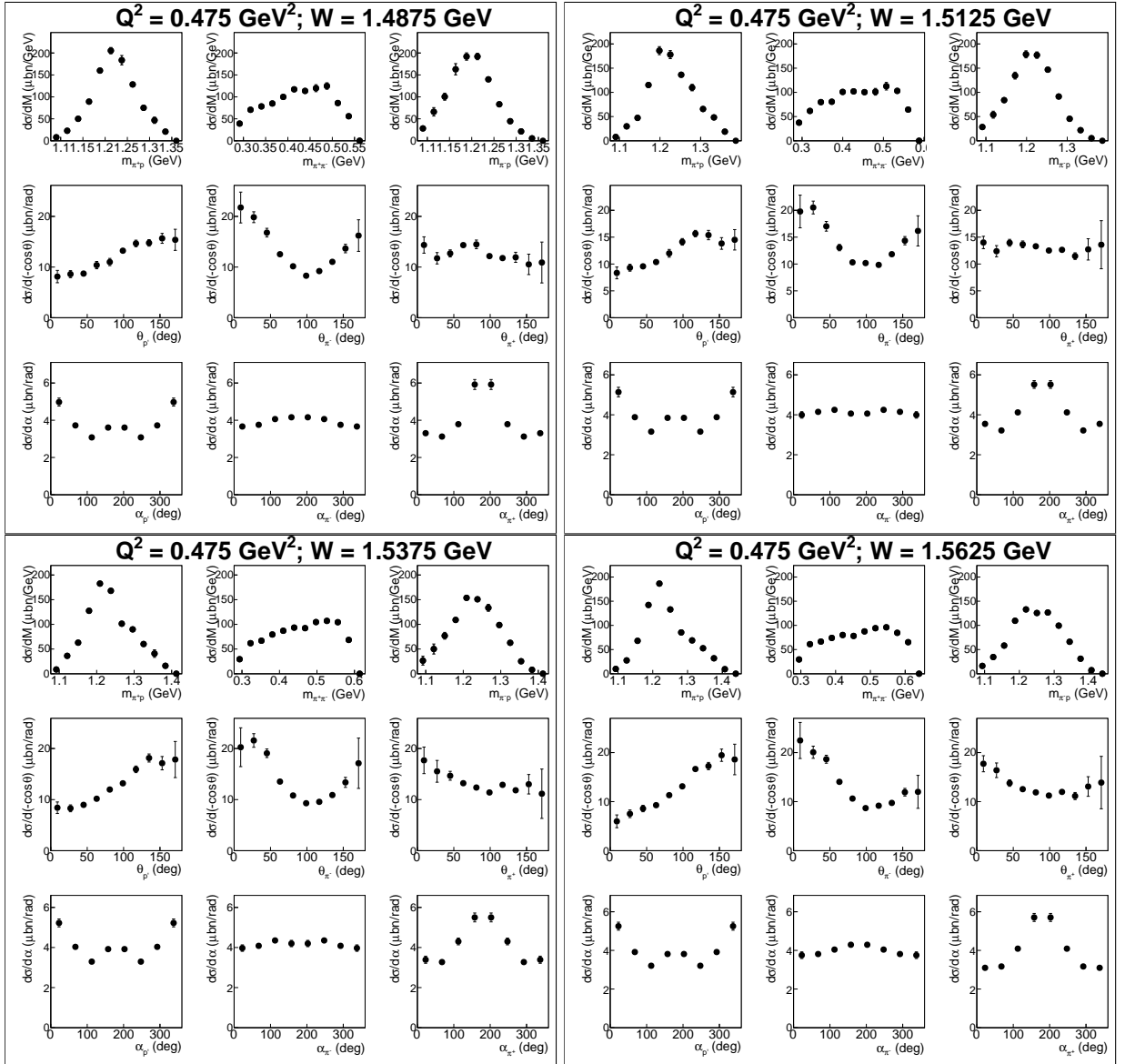


Figure A.5:

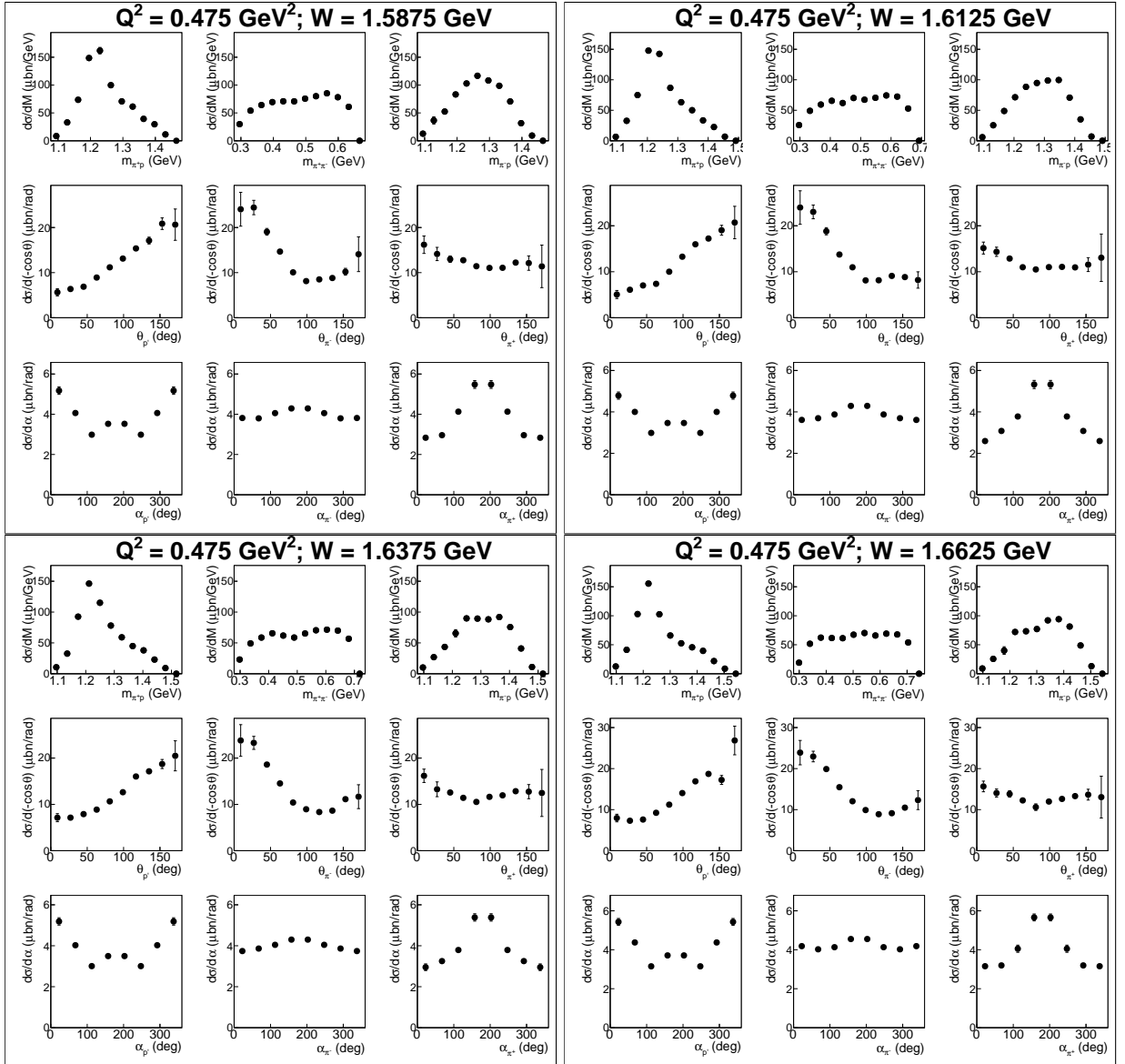


Figure A.6:

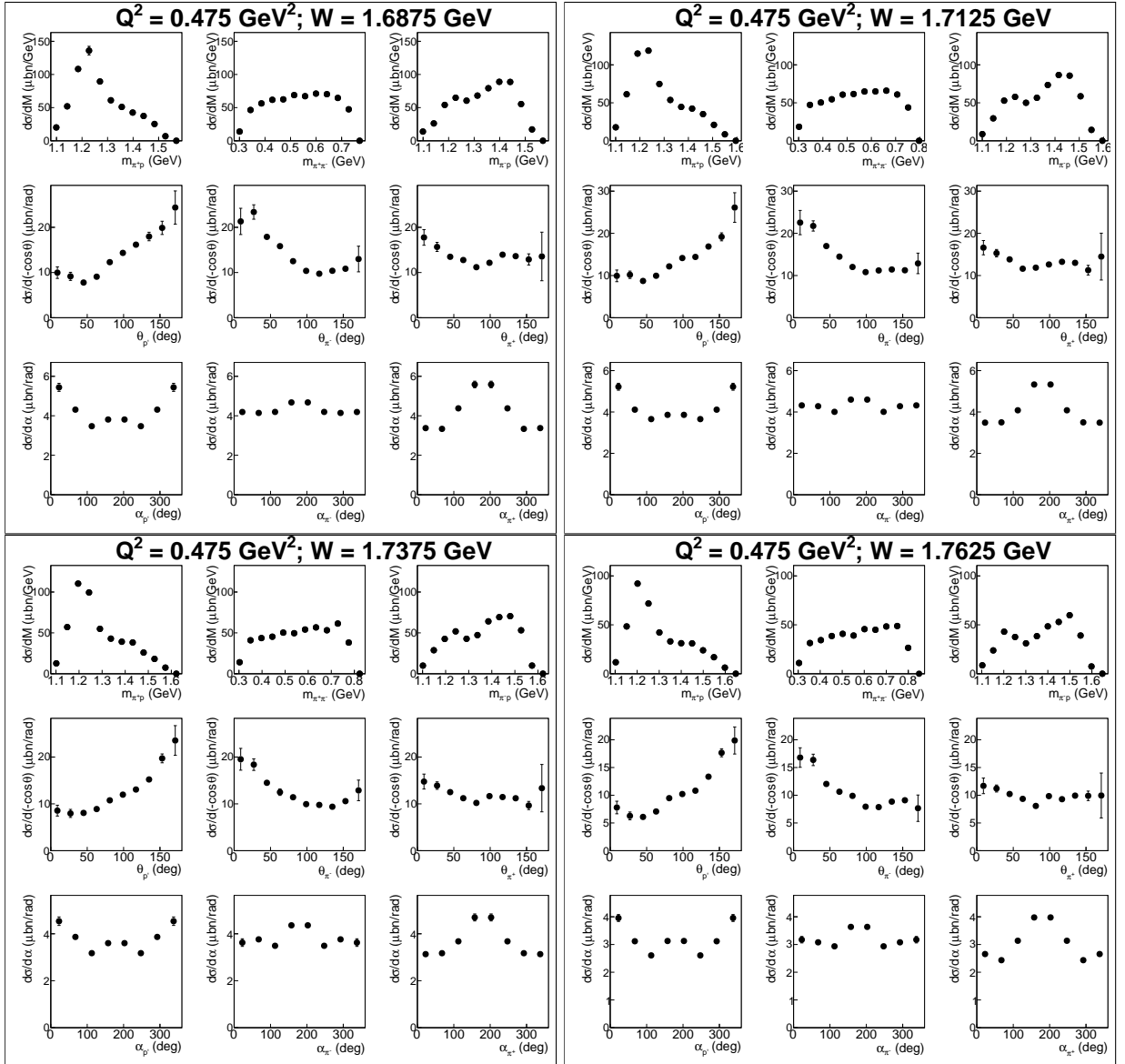


Figure A.7:

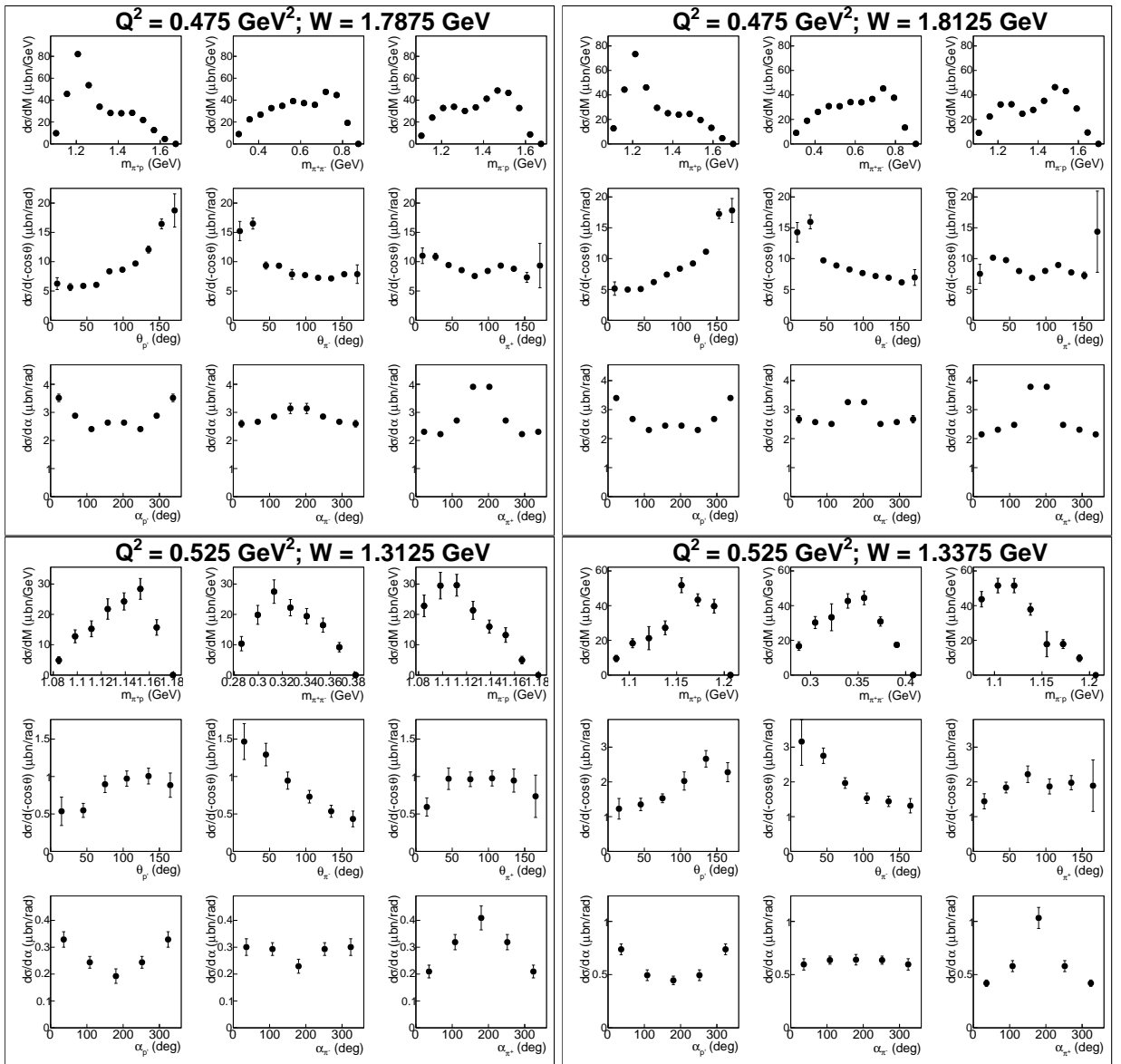


Figure A.8:

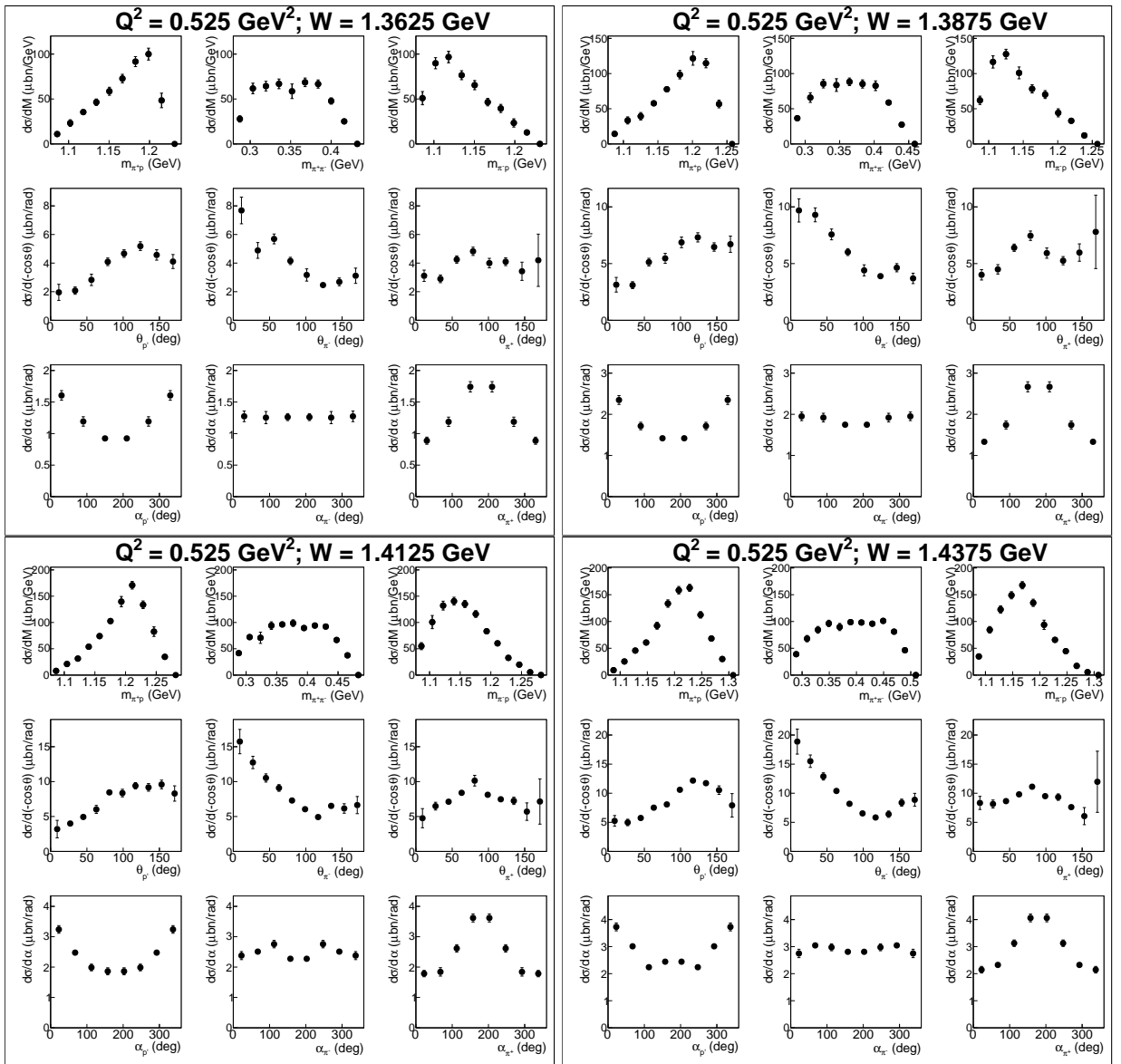


Figure A.9:

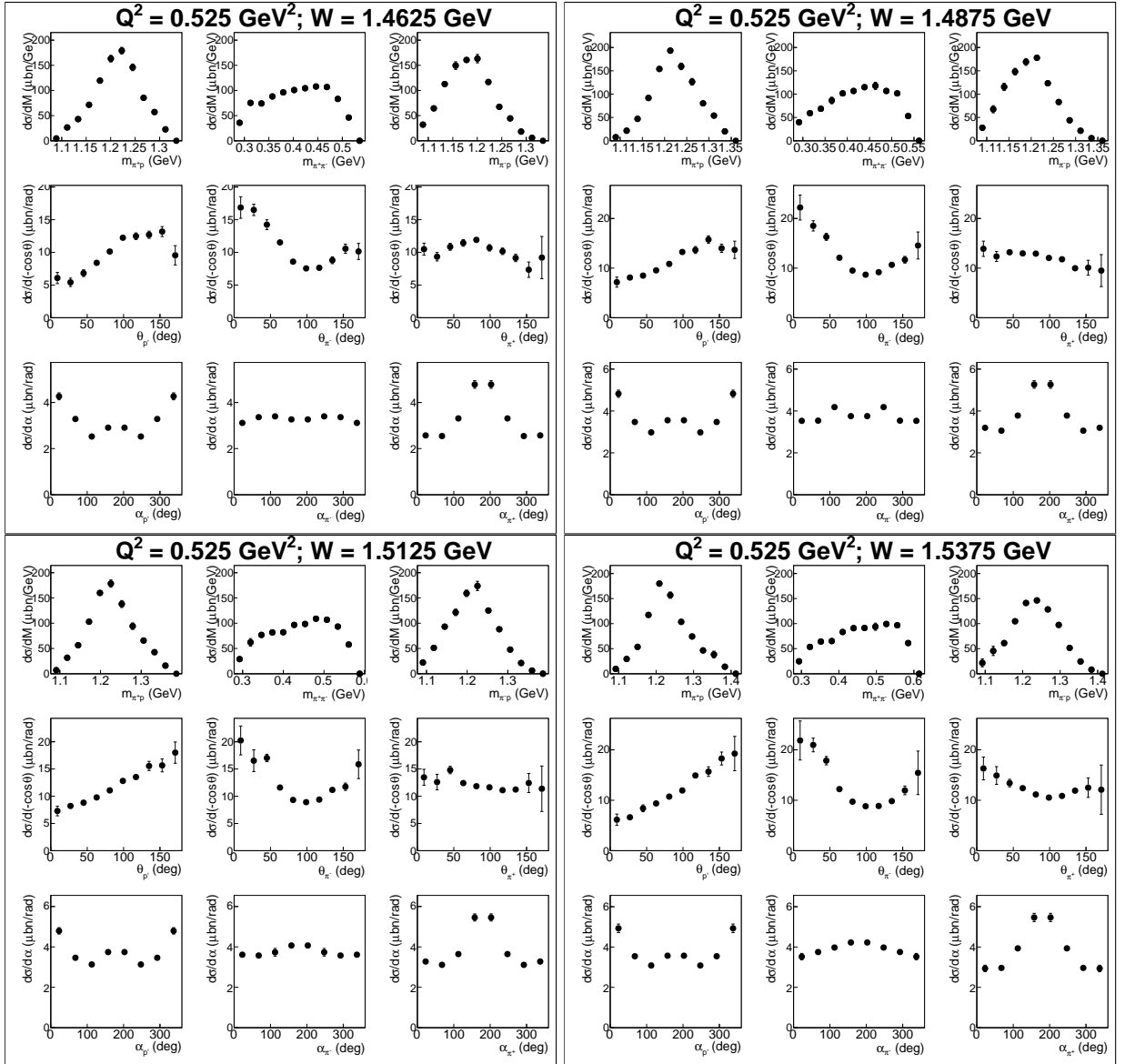


Figure A.10:

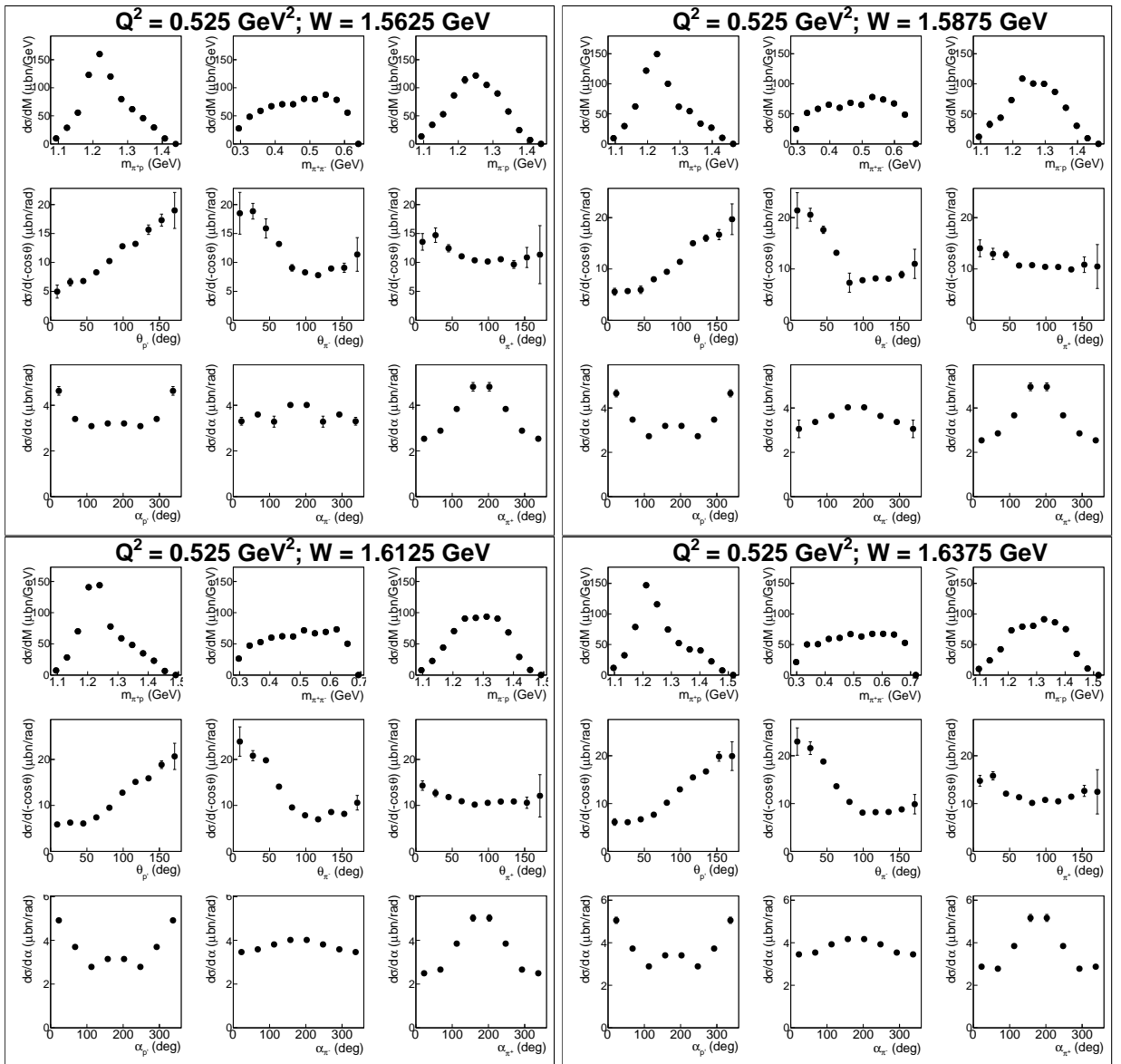


Figure A.11:

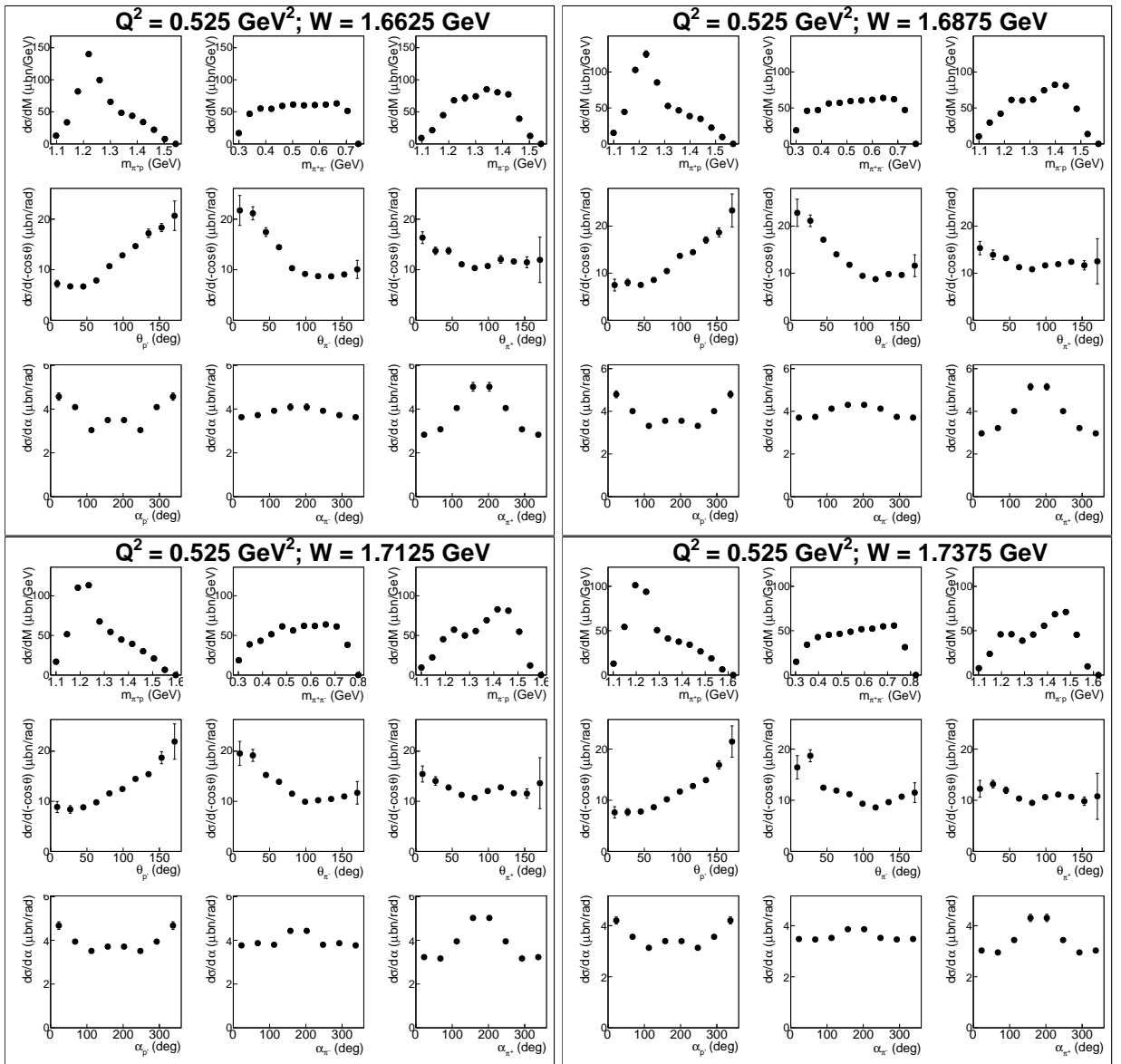


Figure A.12:

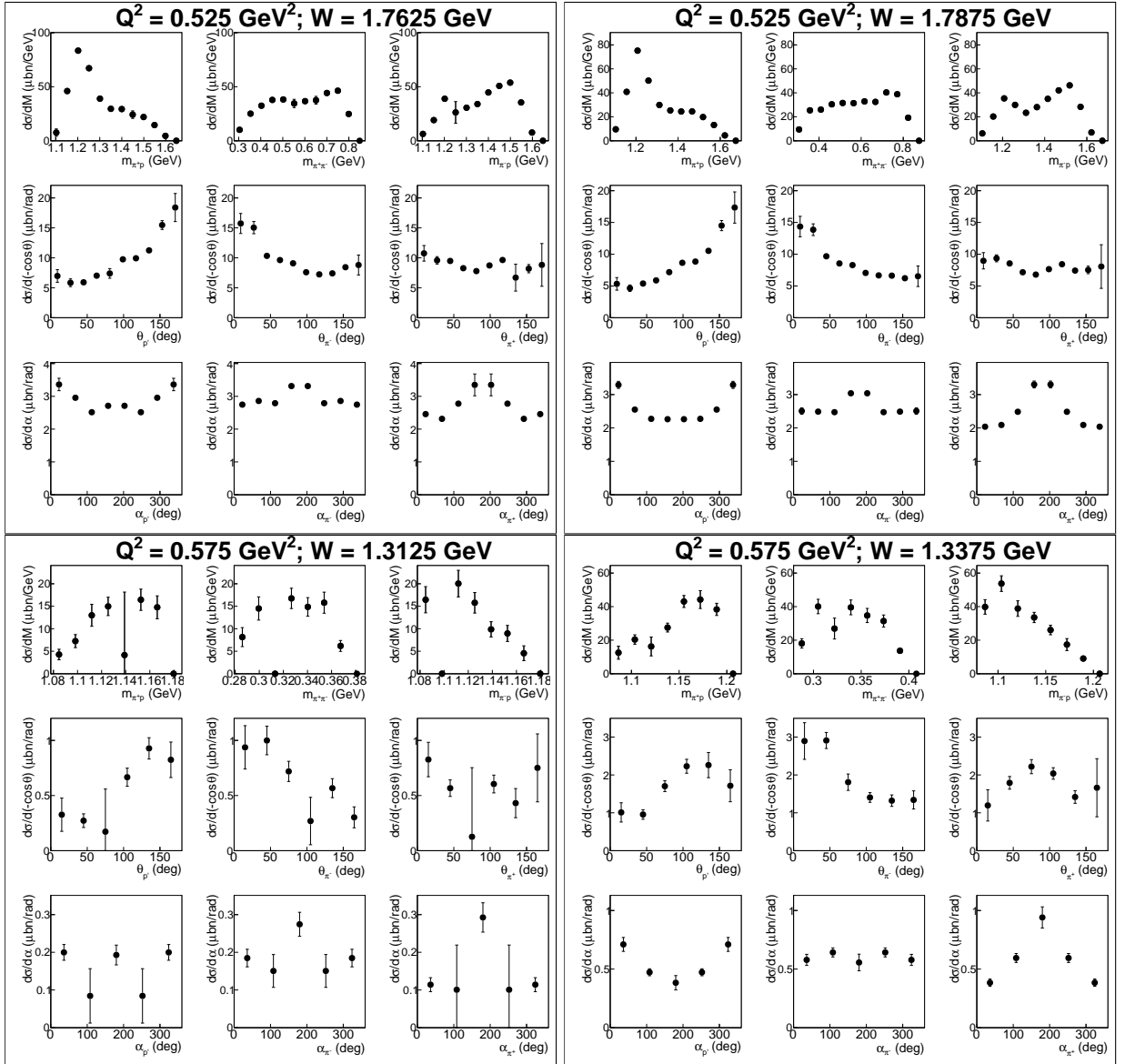


Figure A.13:

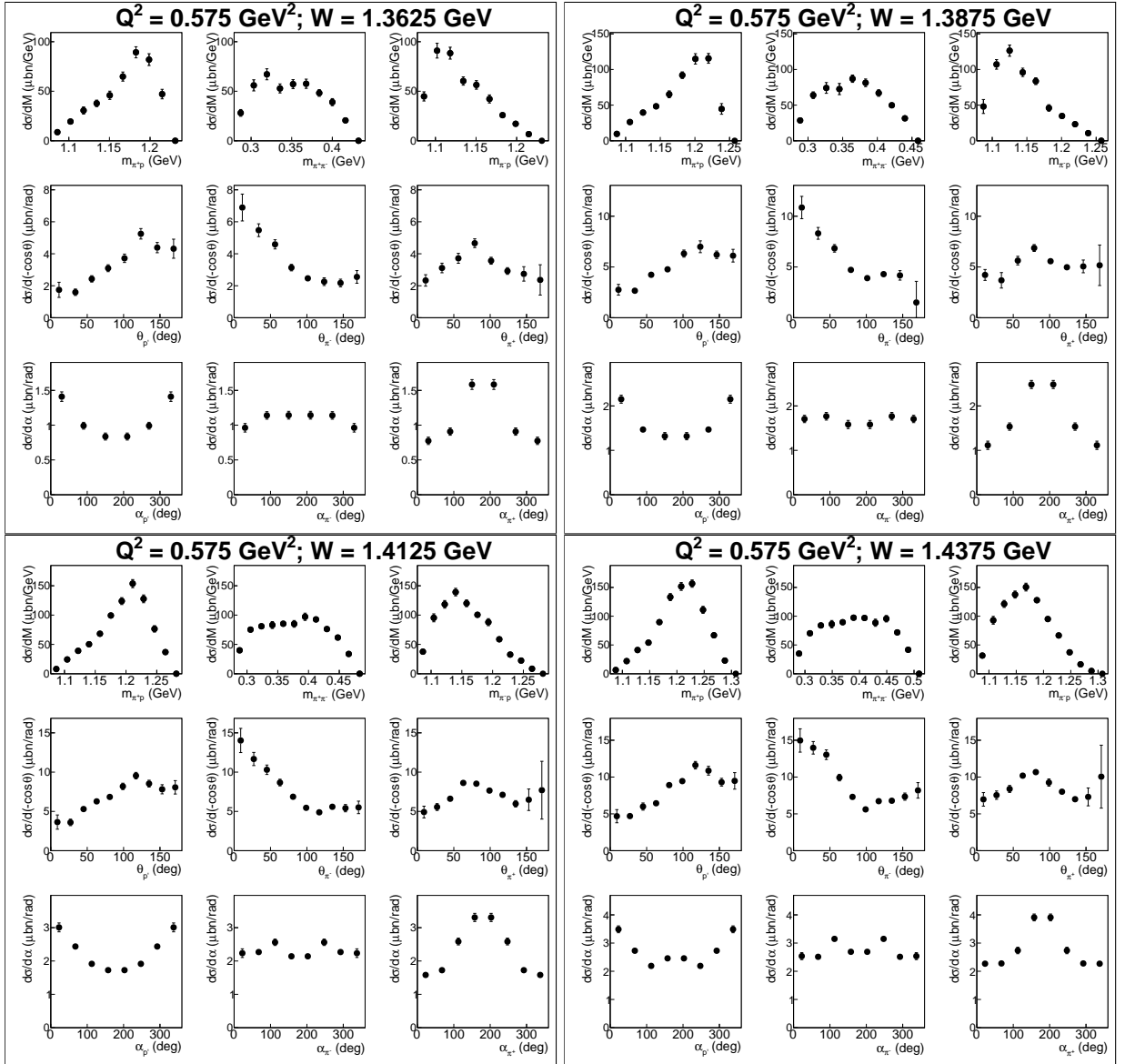


Figure A.14:

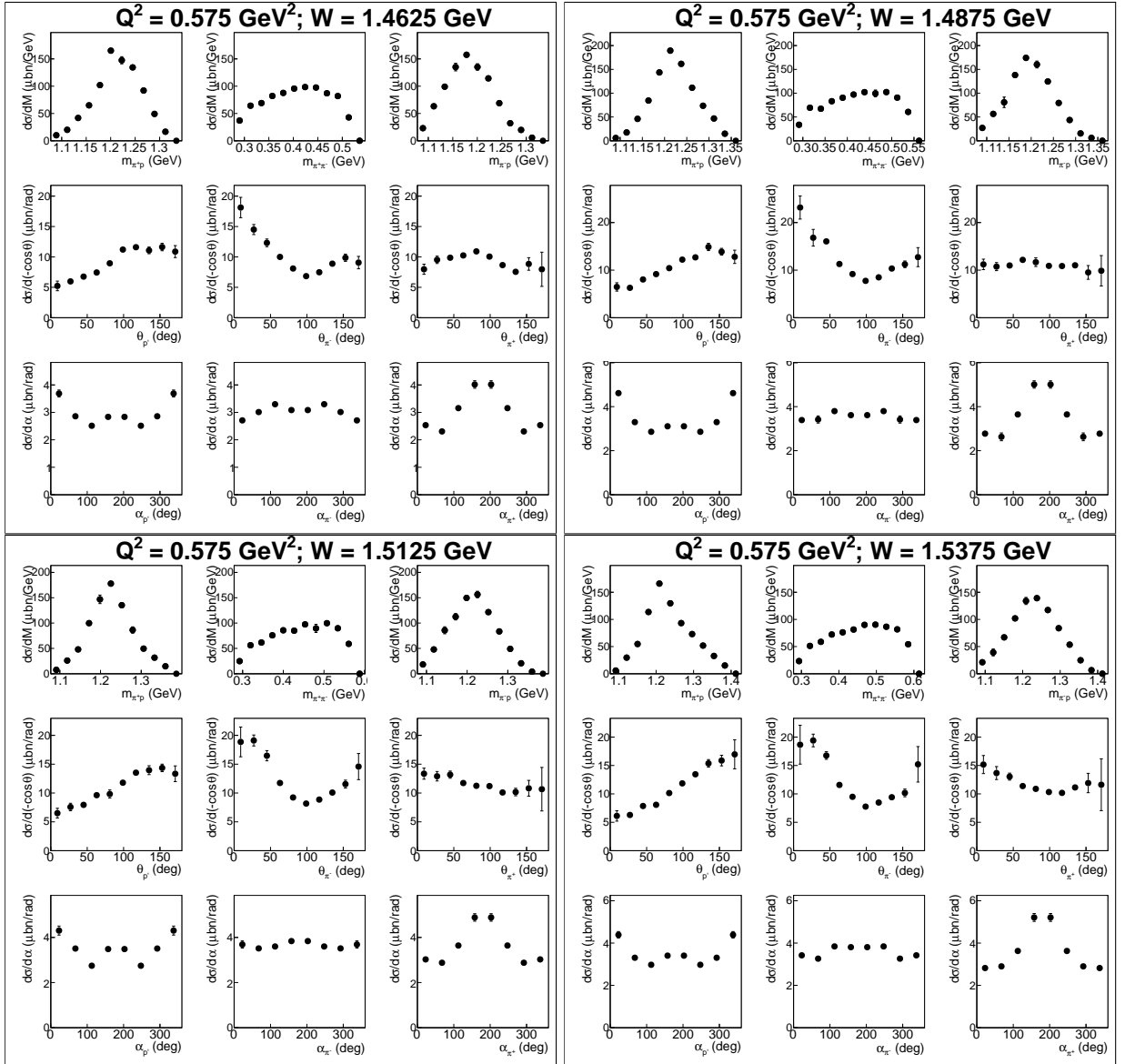


Figure A.15:

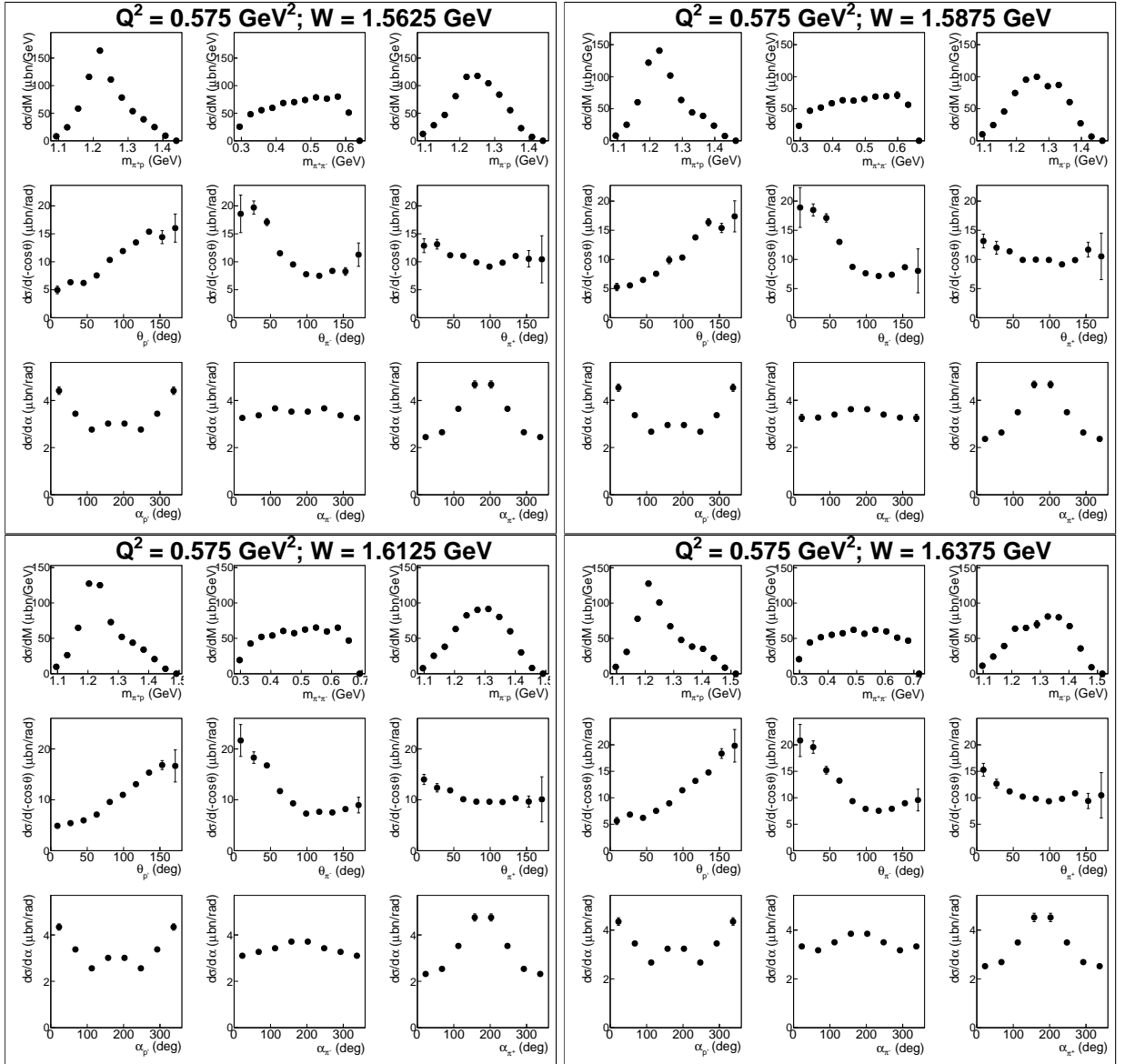


Figure A.16:

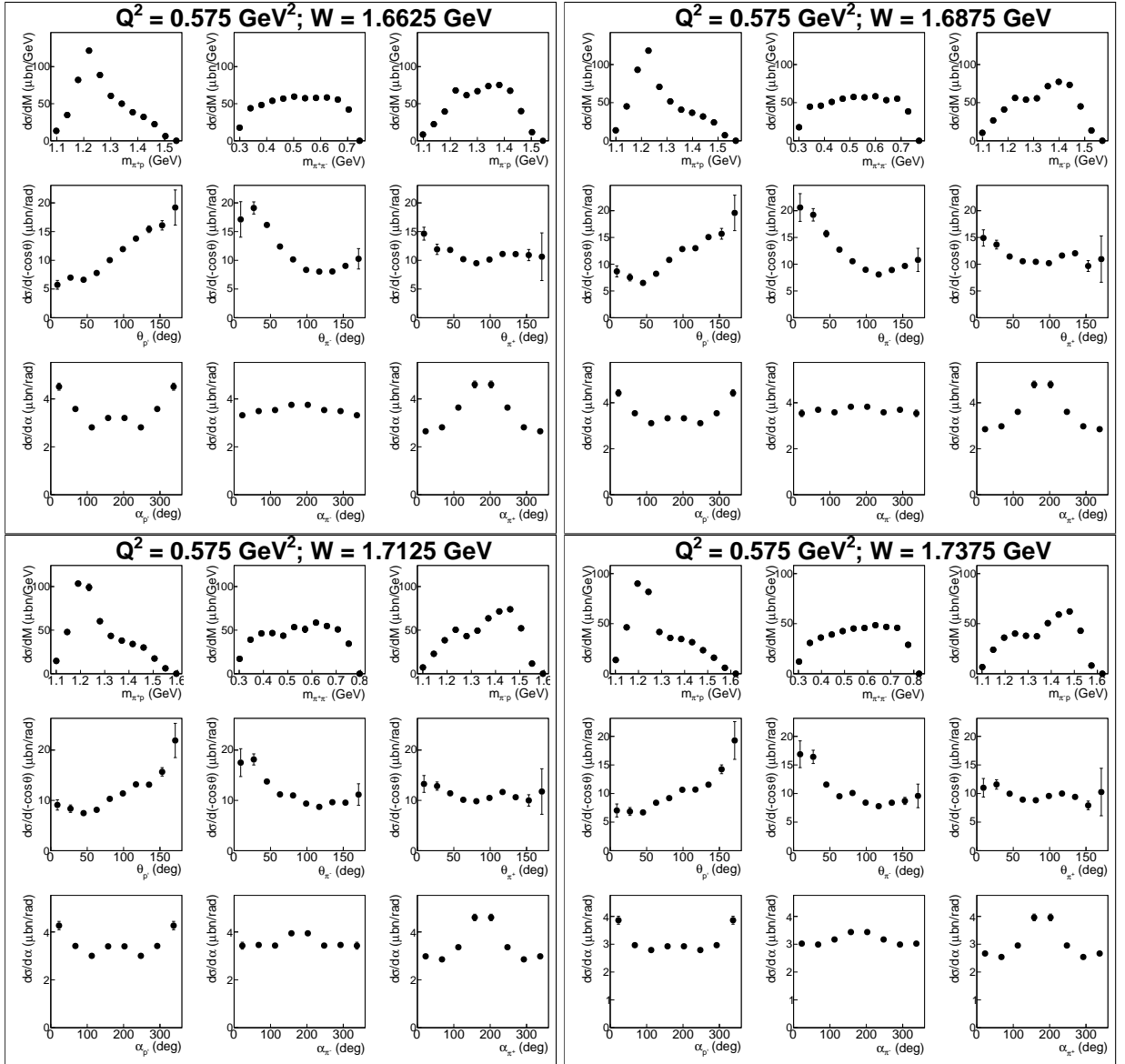


Figure A.17:

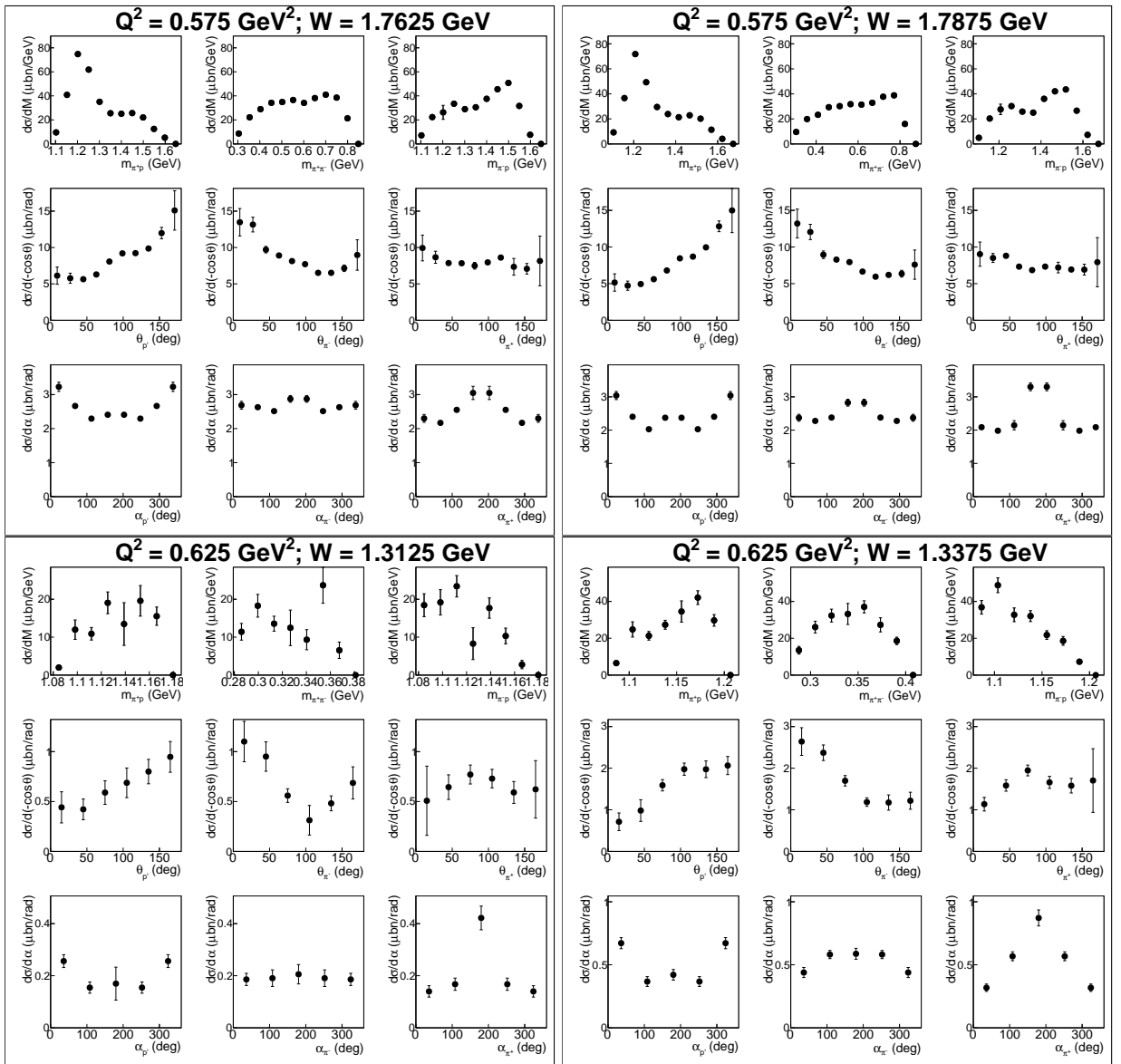


Figure A.18:

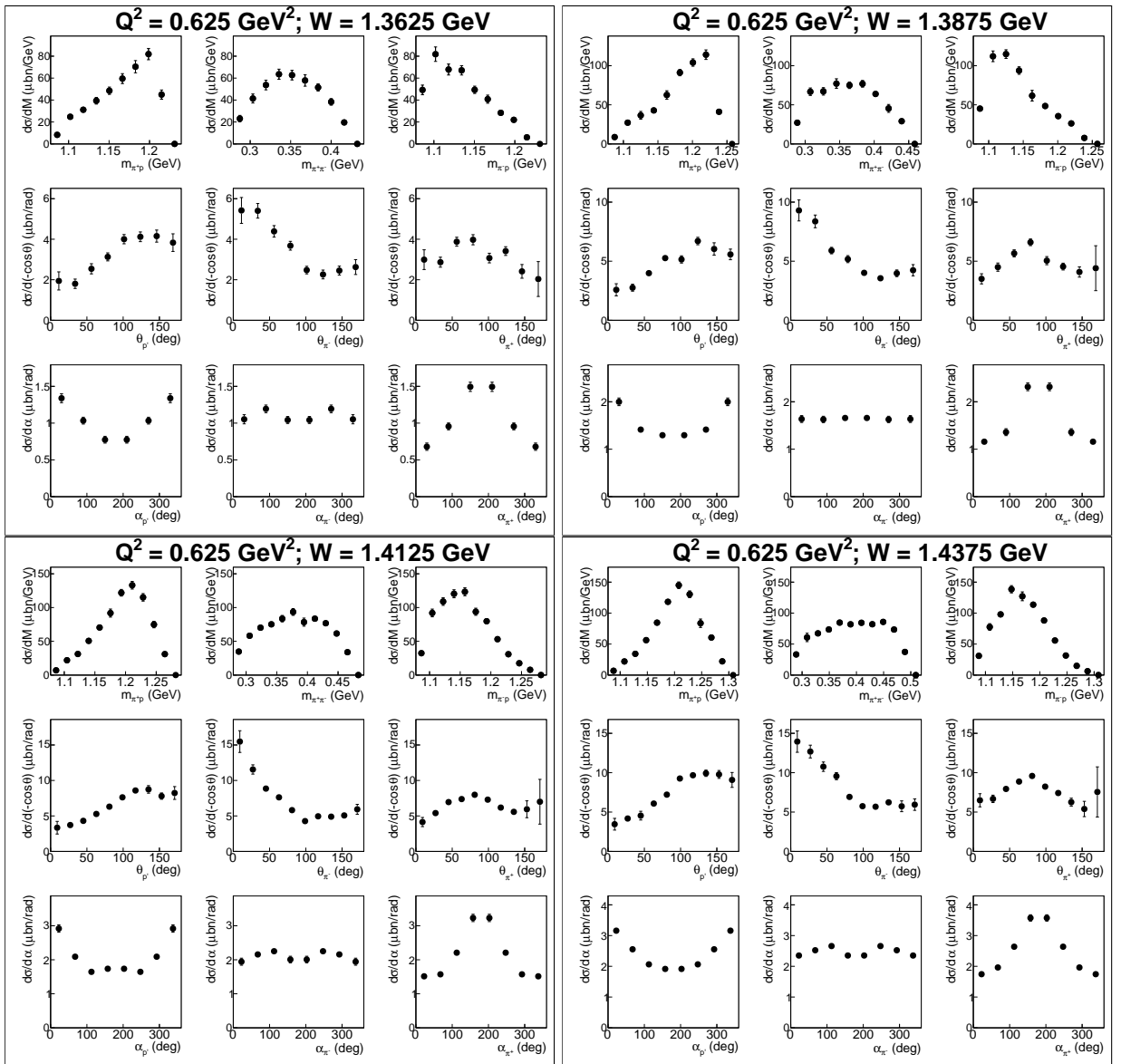


Figure A.19:

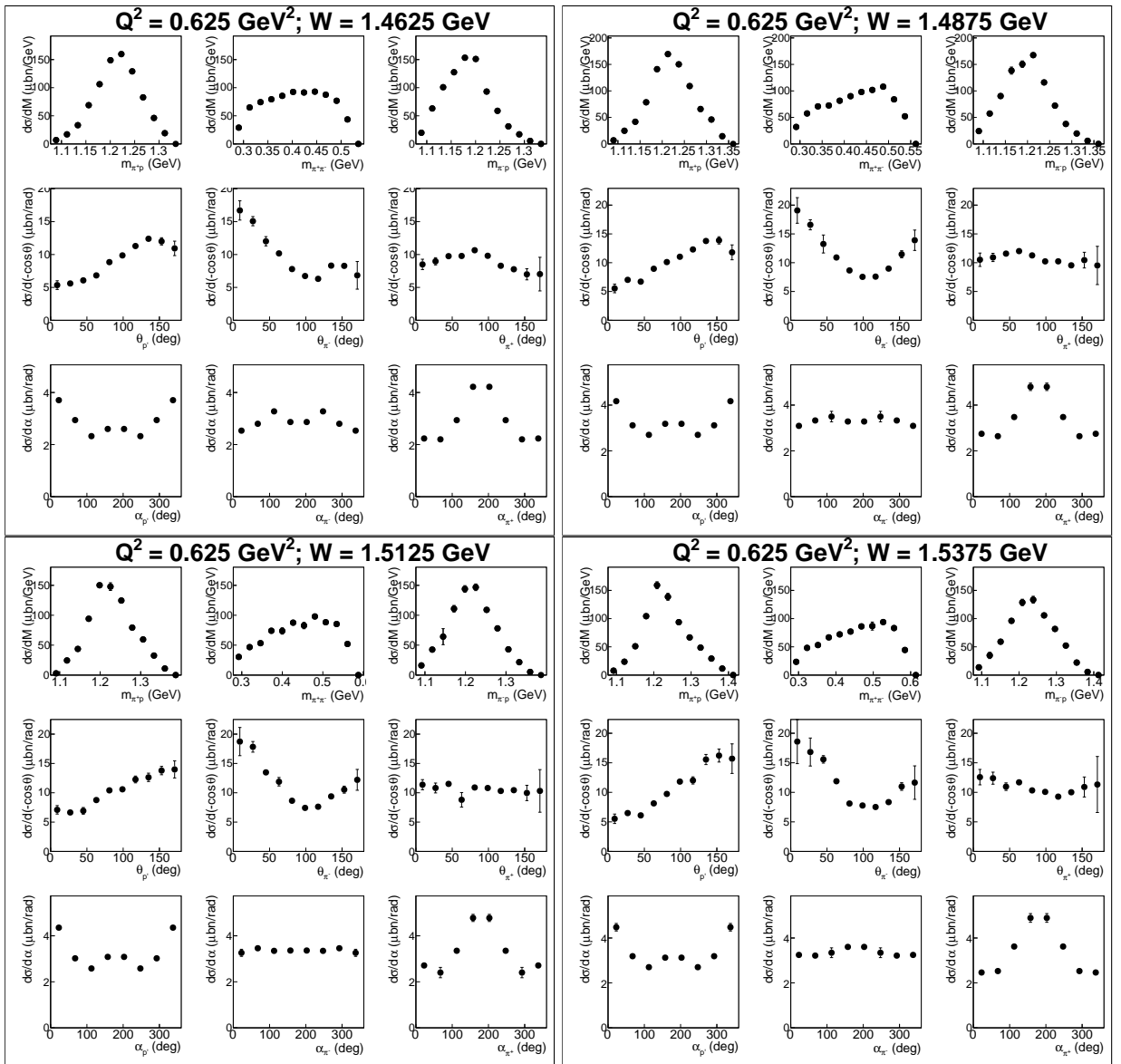


Figure A.20:

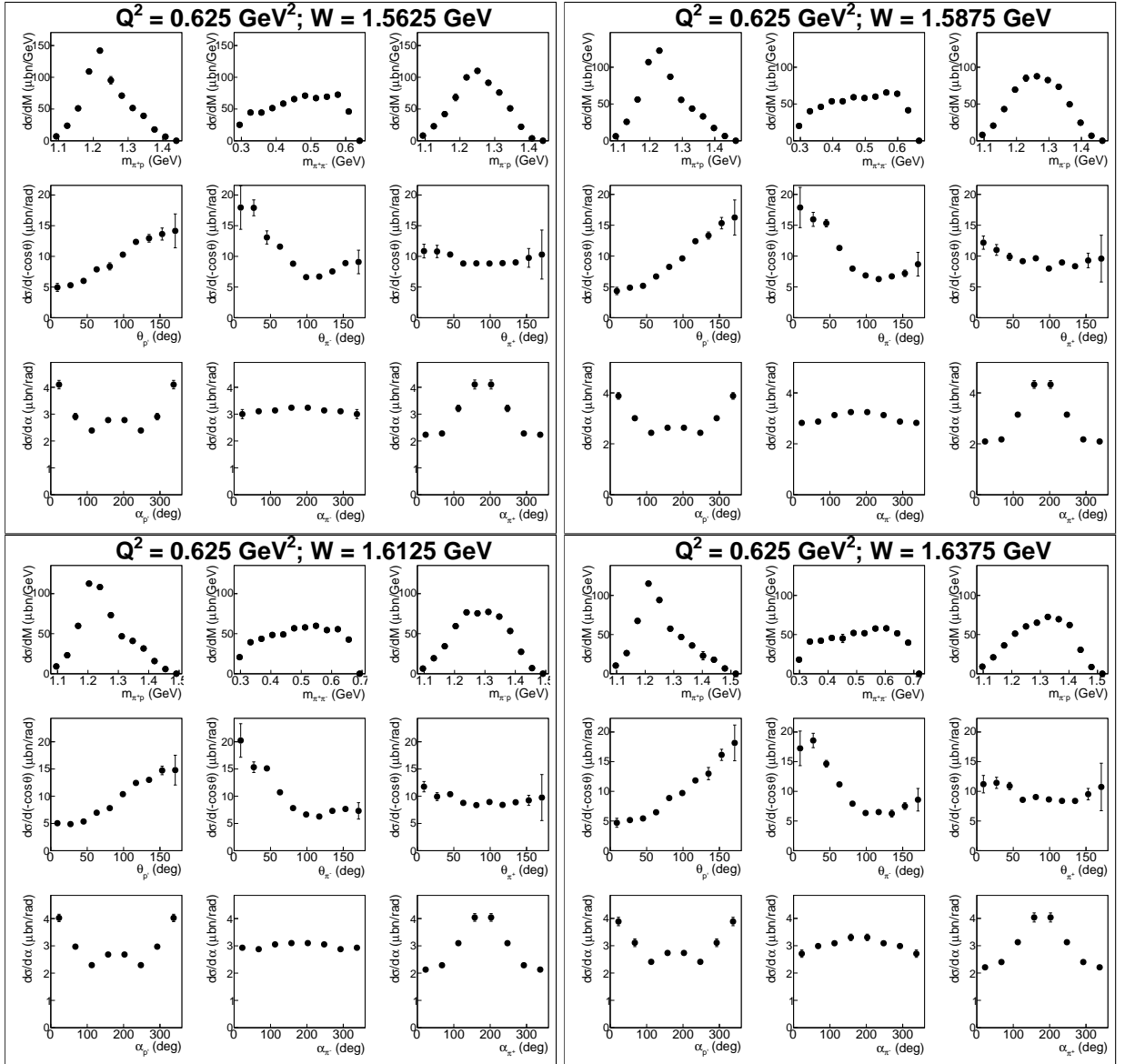


Figure A.21:

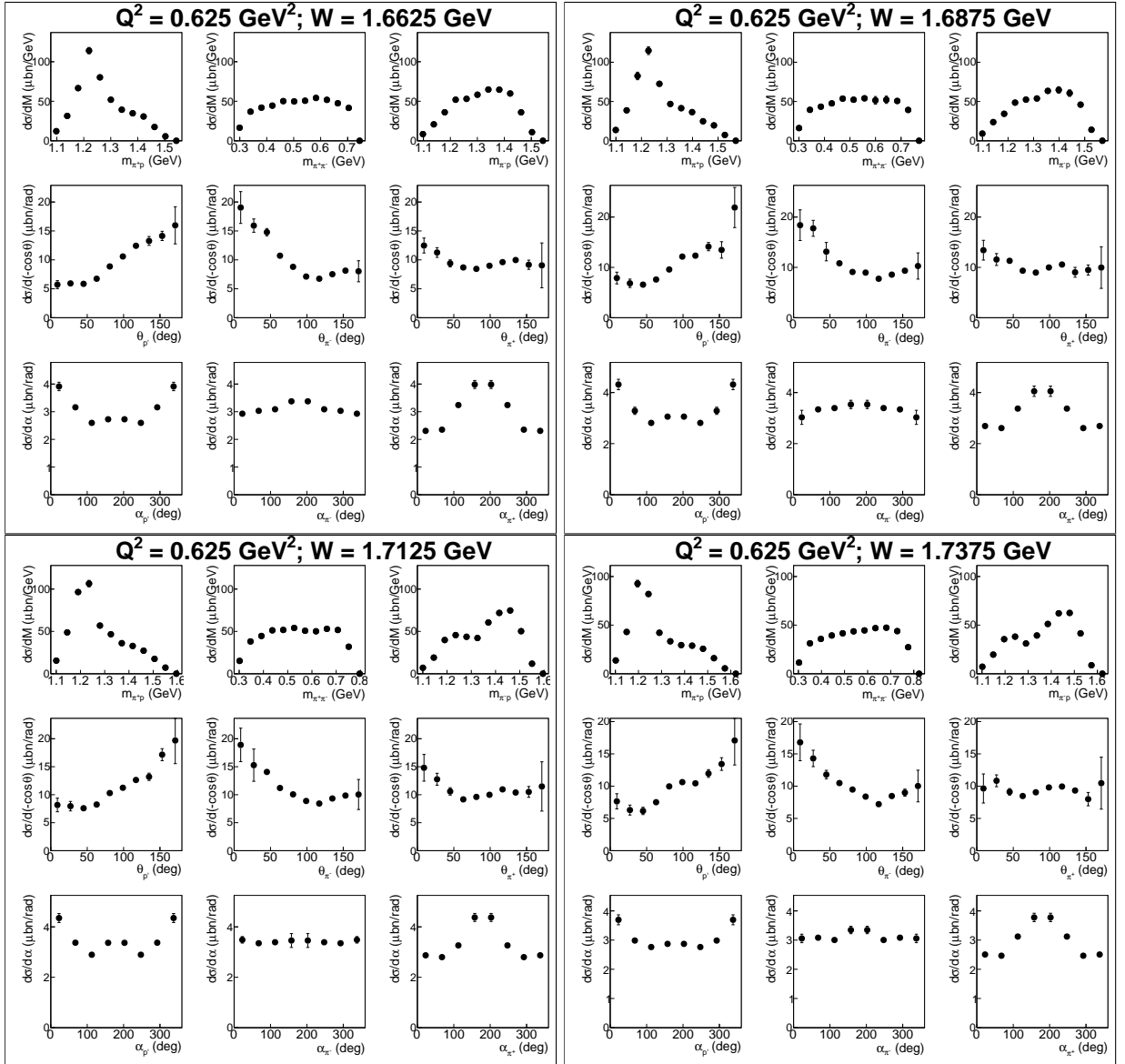


Figure A.22:

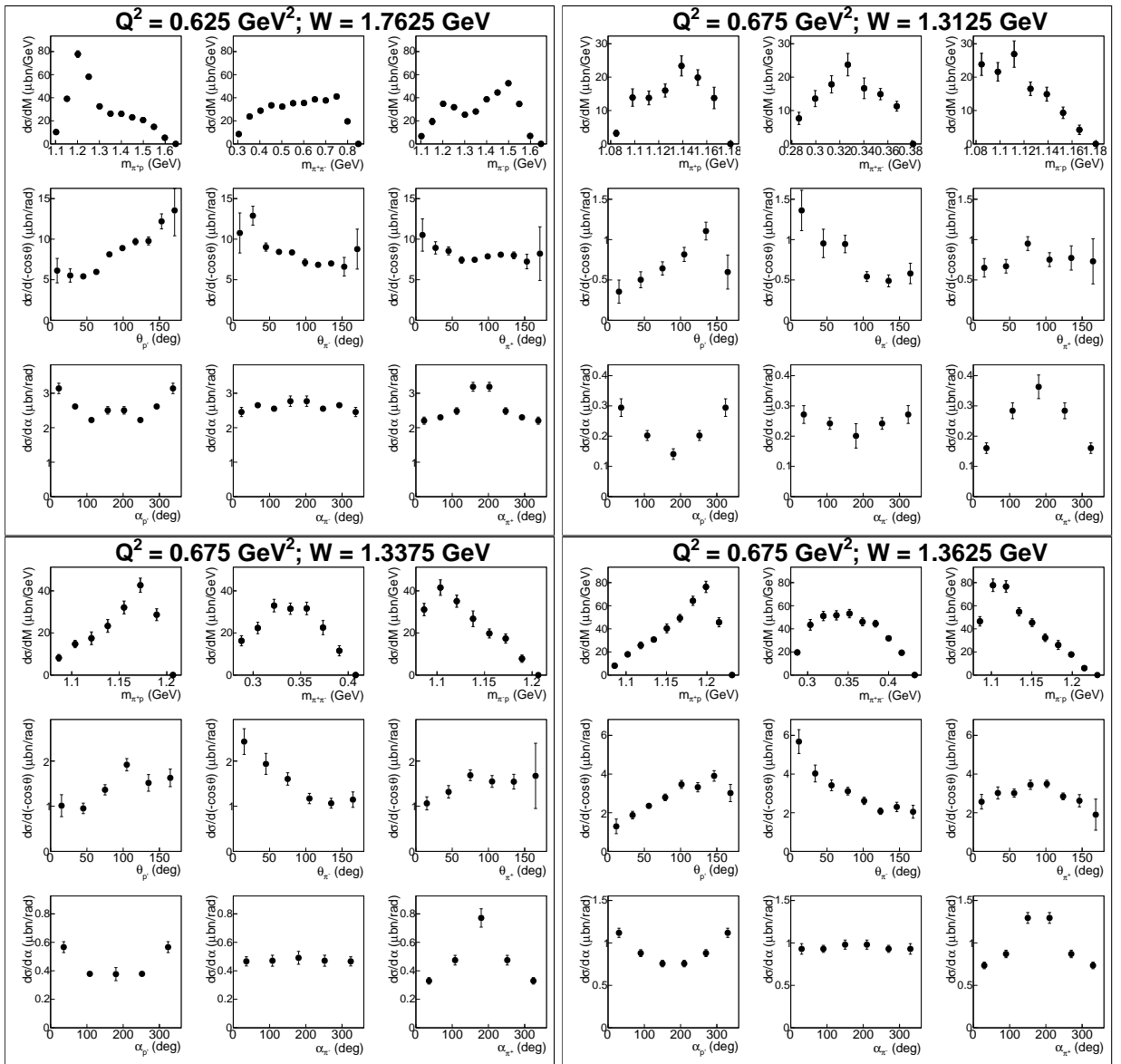


Figure A.23:

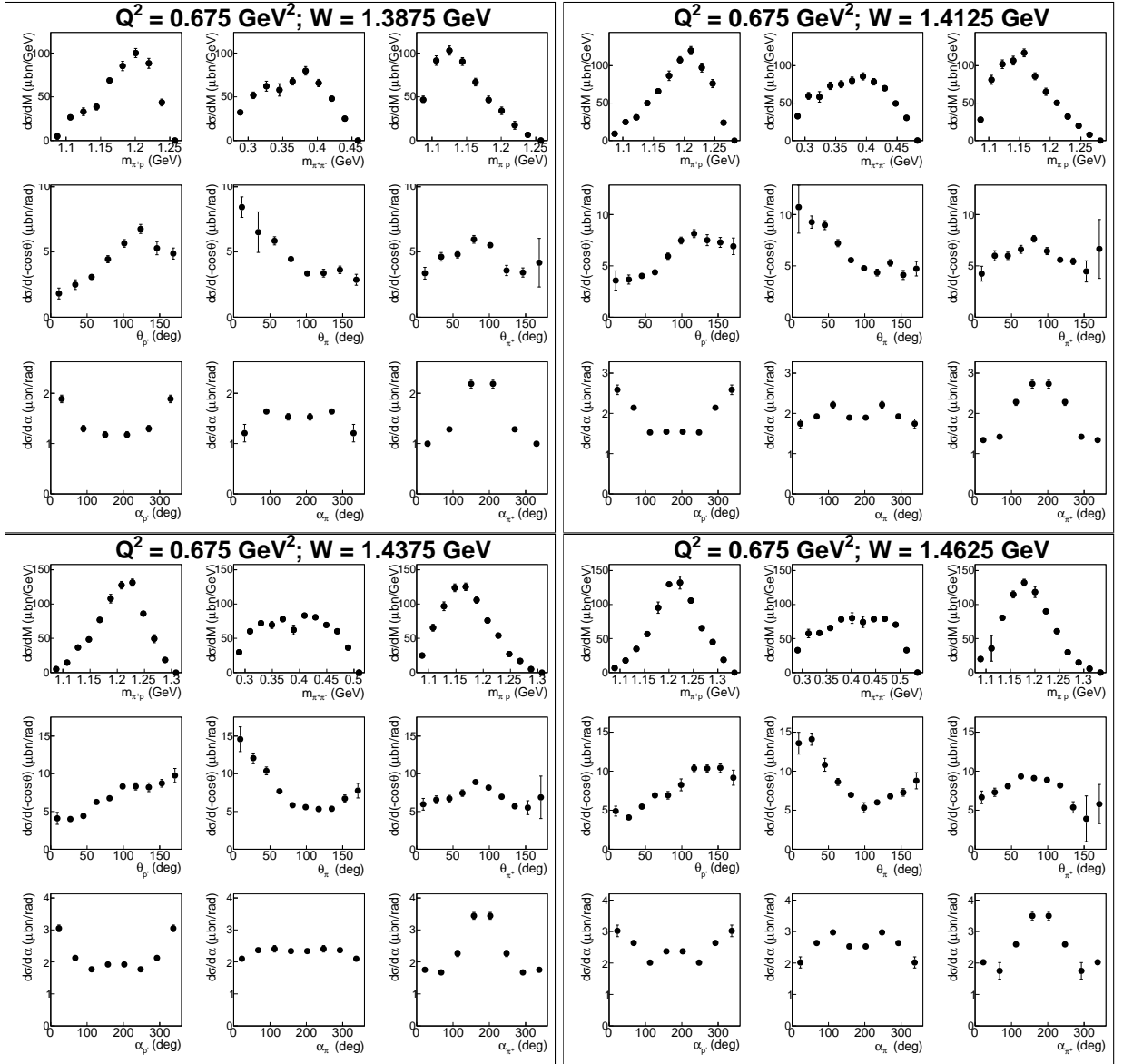


Figure A.24:

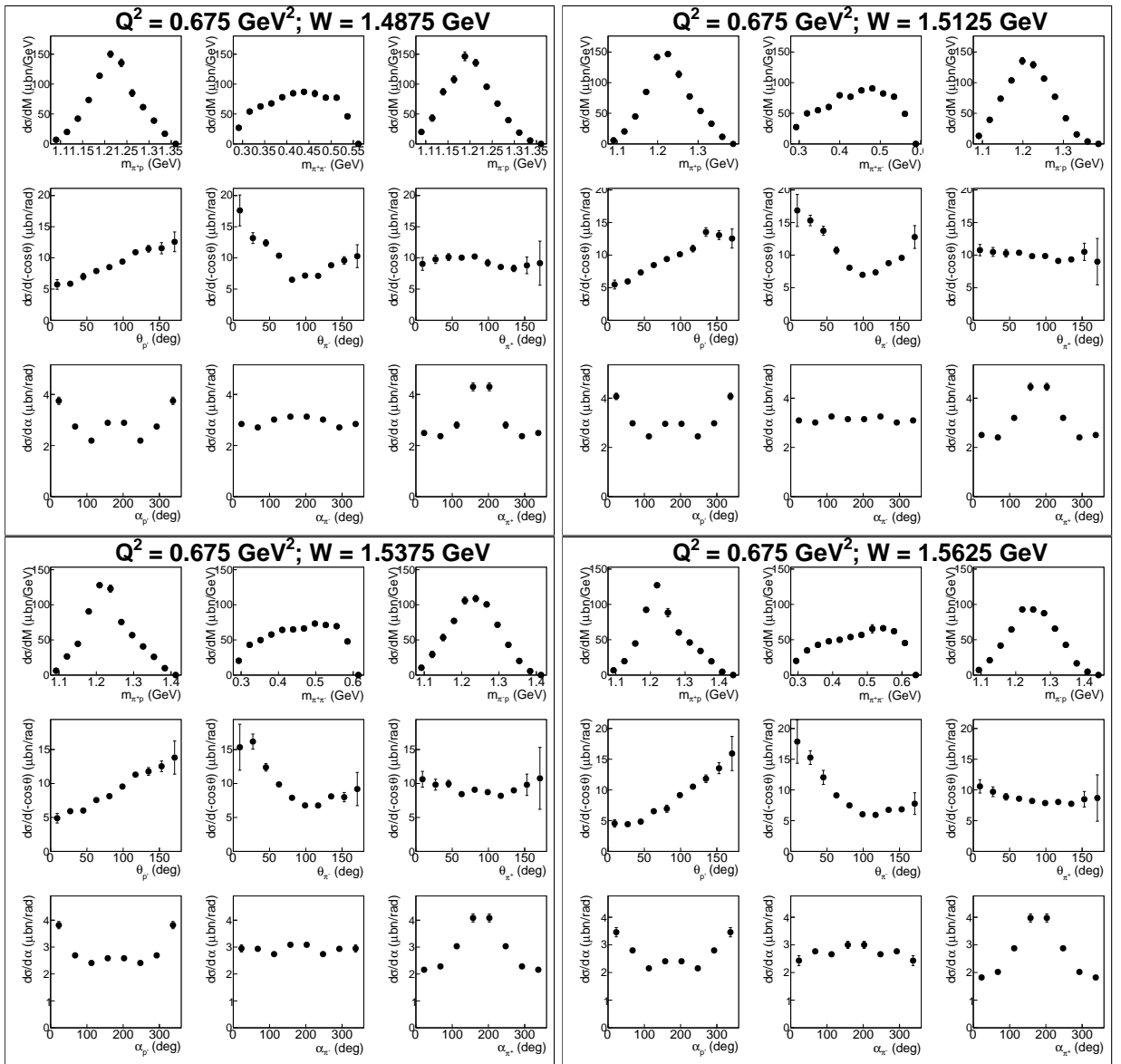


Figure A.25:

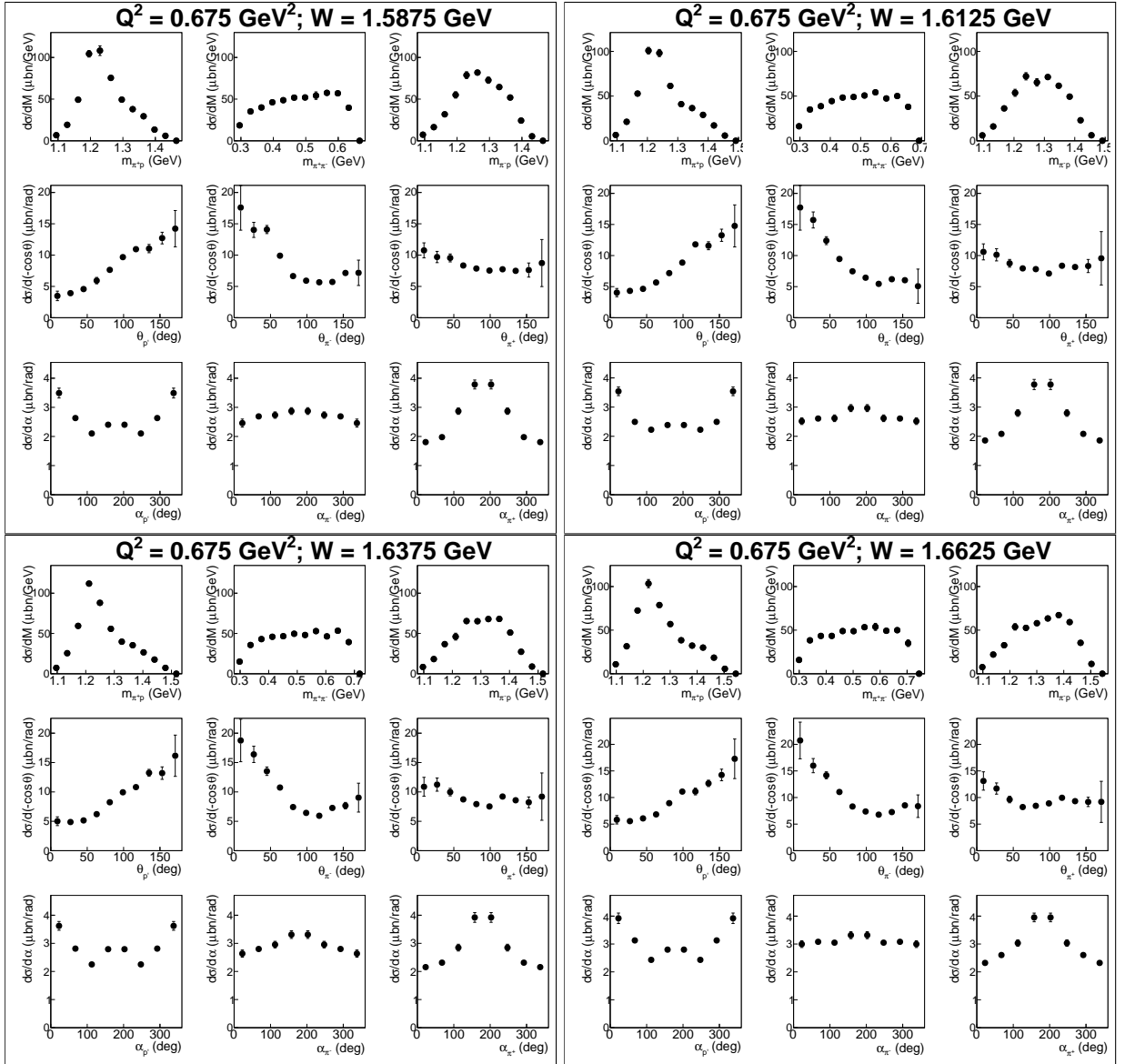


Figure A.26:

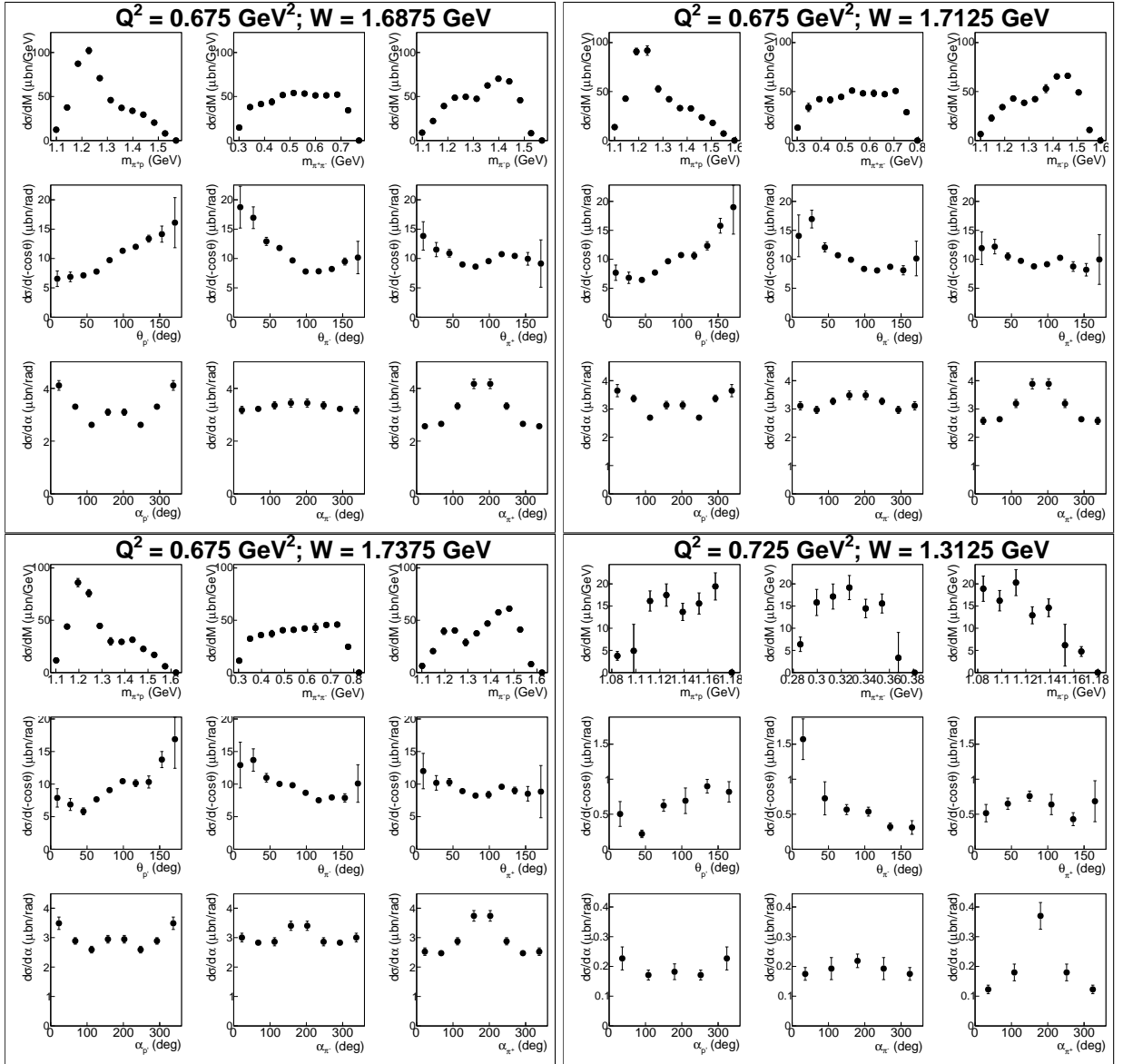


Figure A.27:

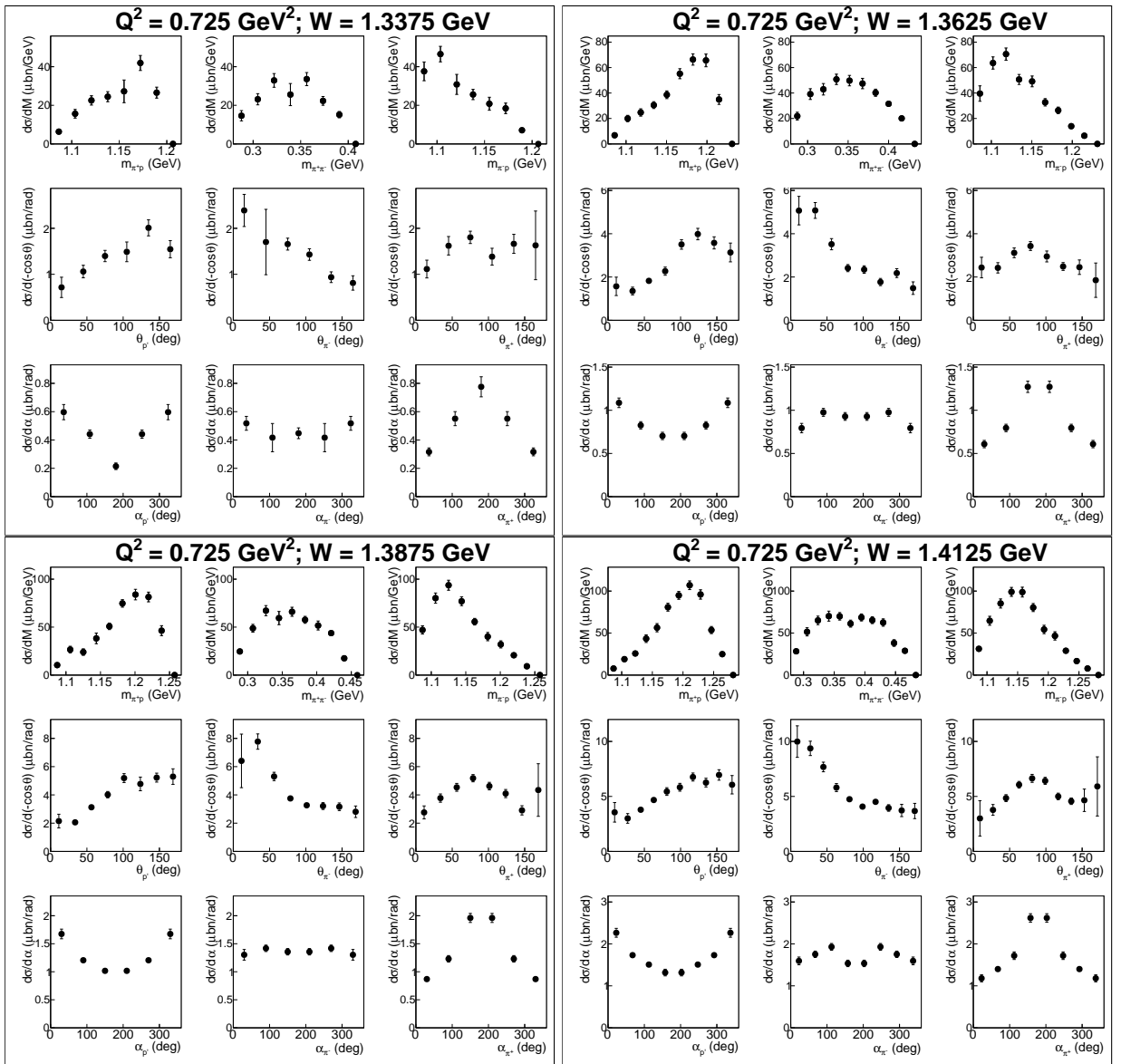


Figure A.28:

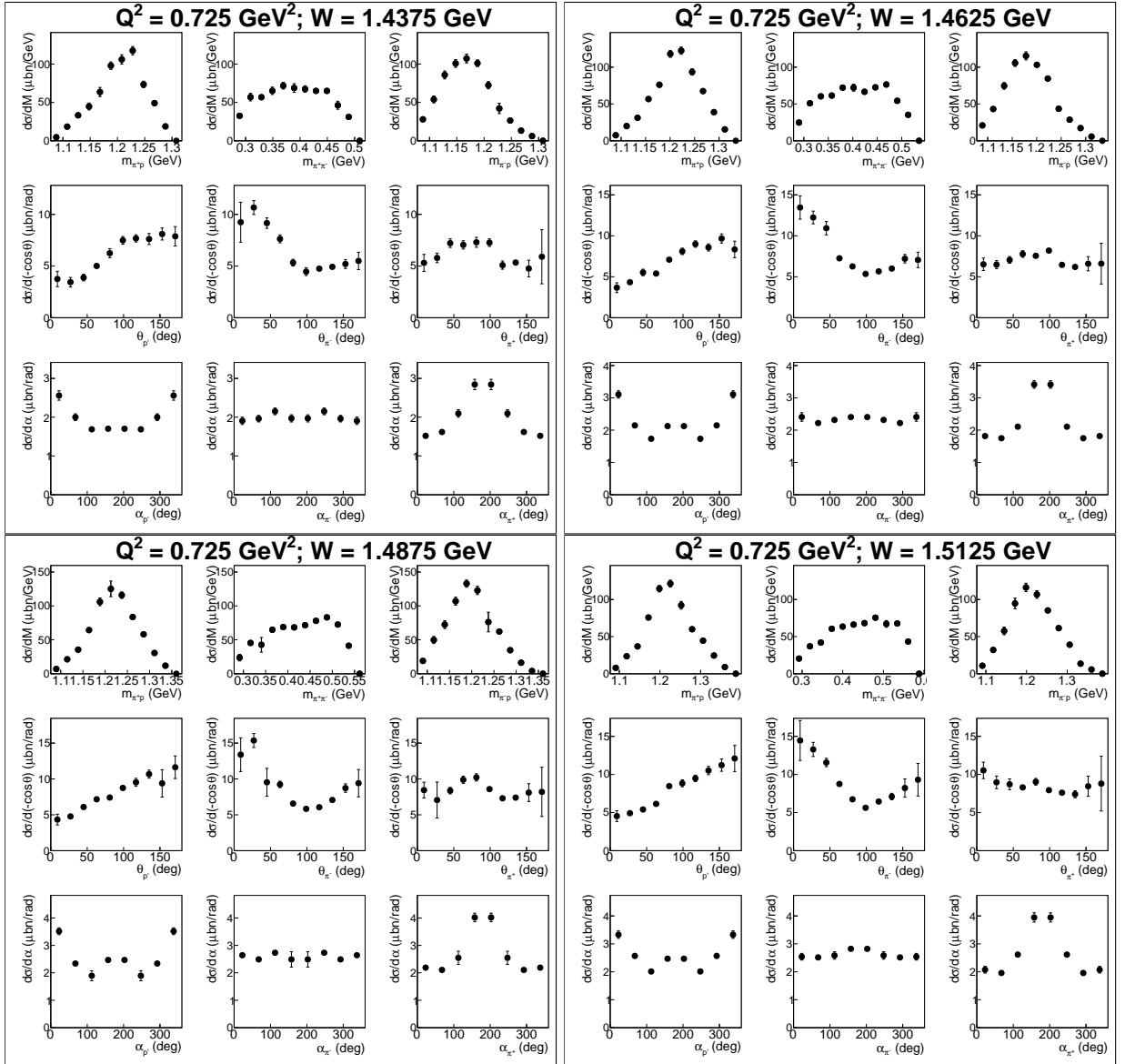


Figure A.29:

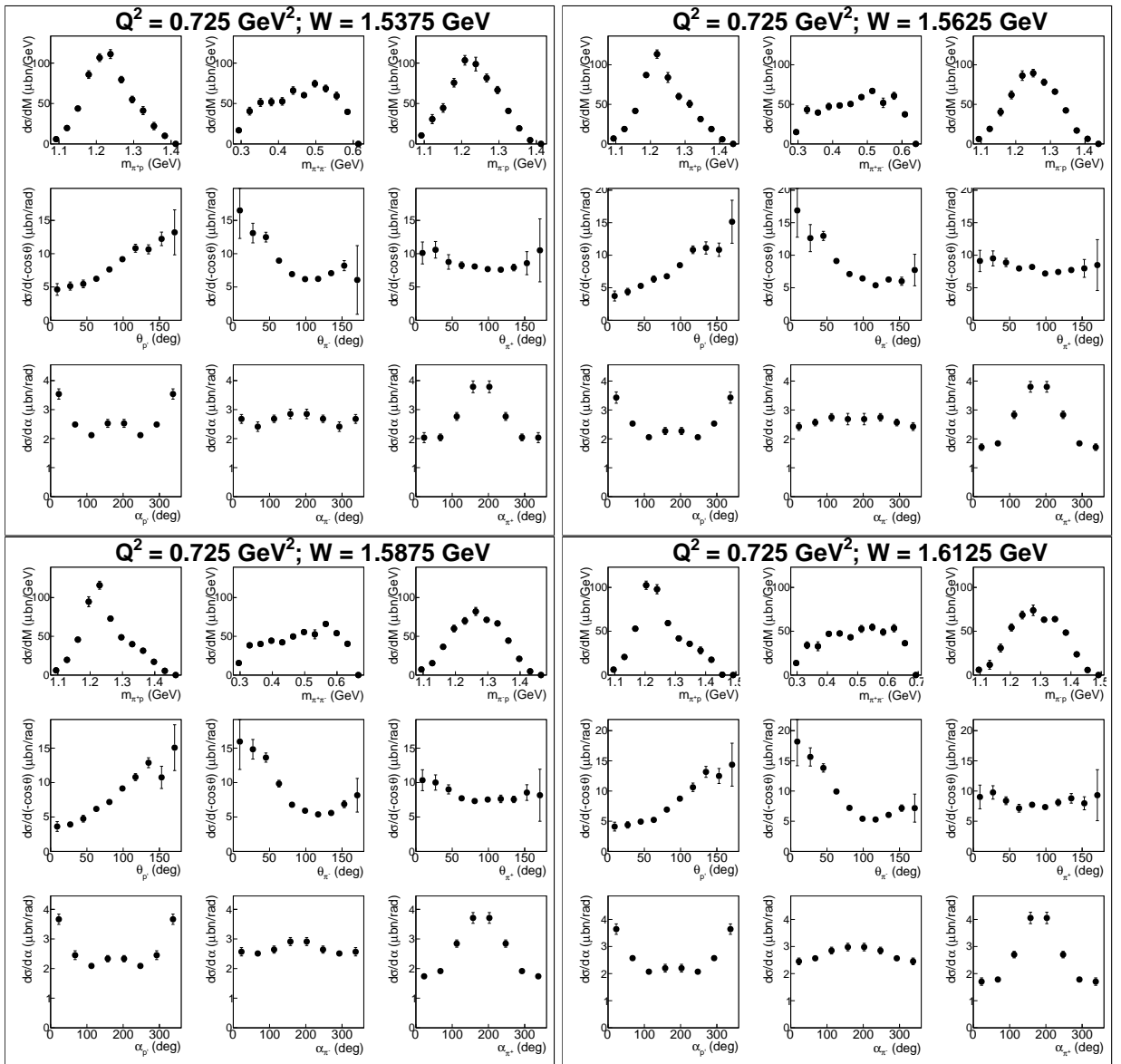


Figure A.30:

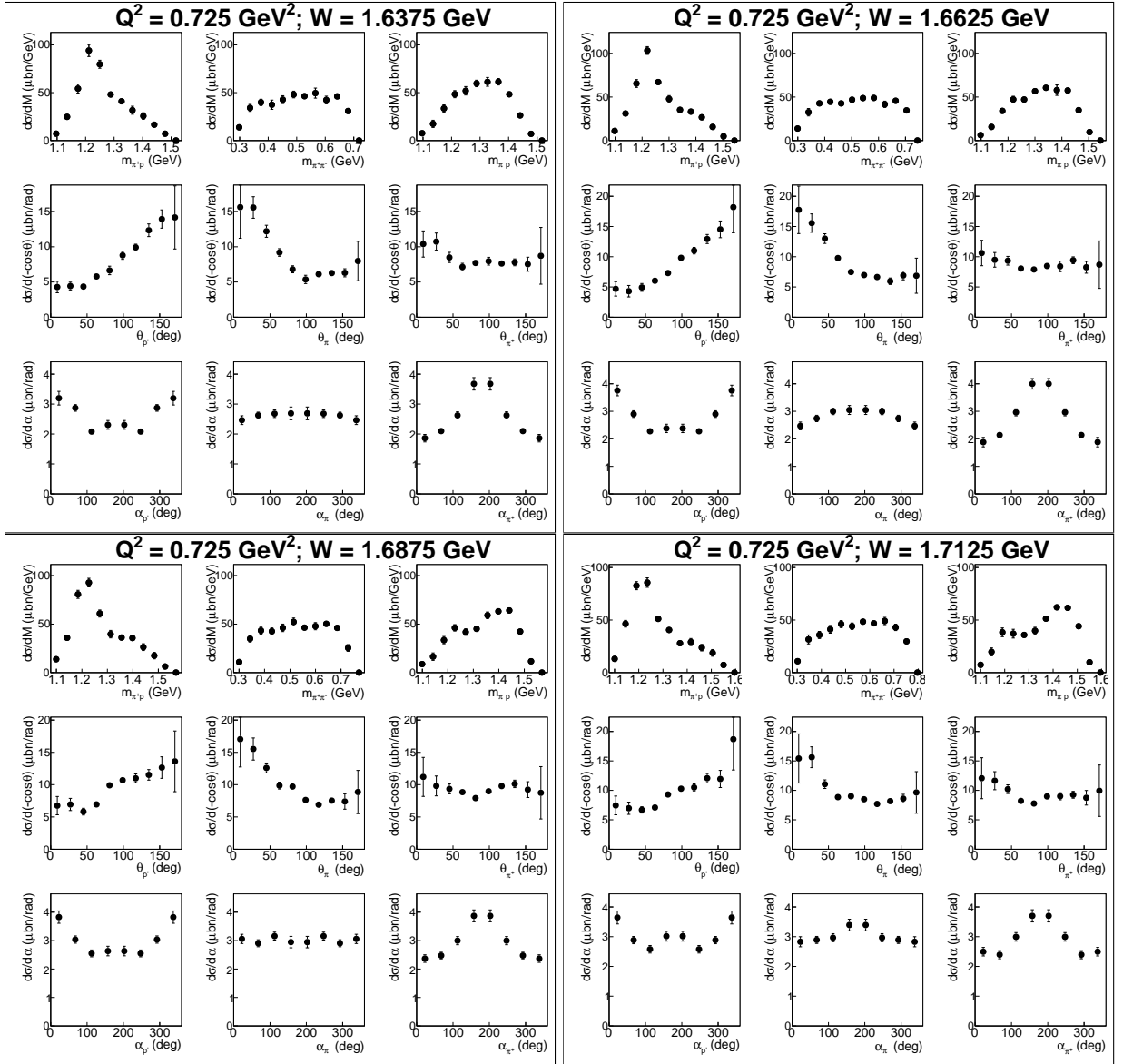


Figure A.31:

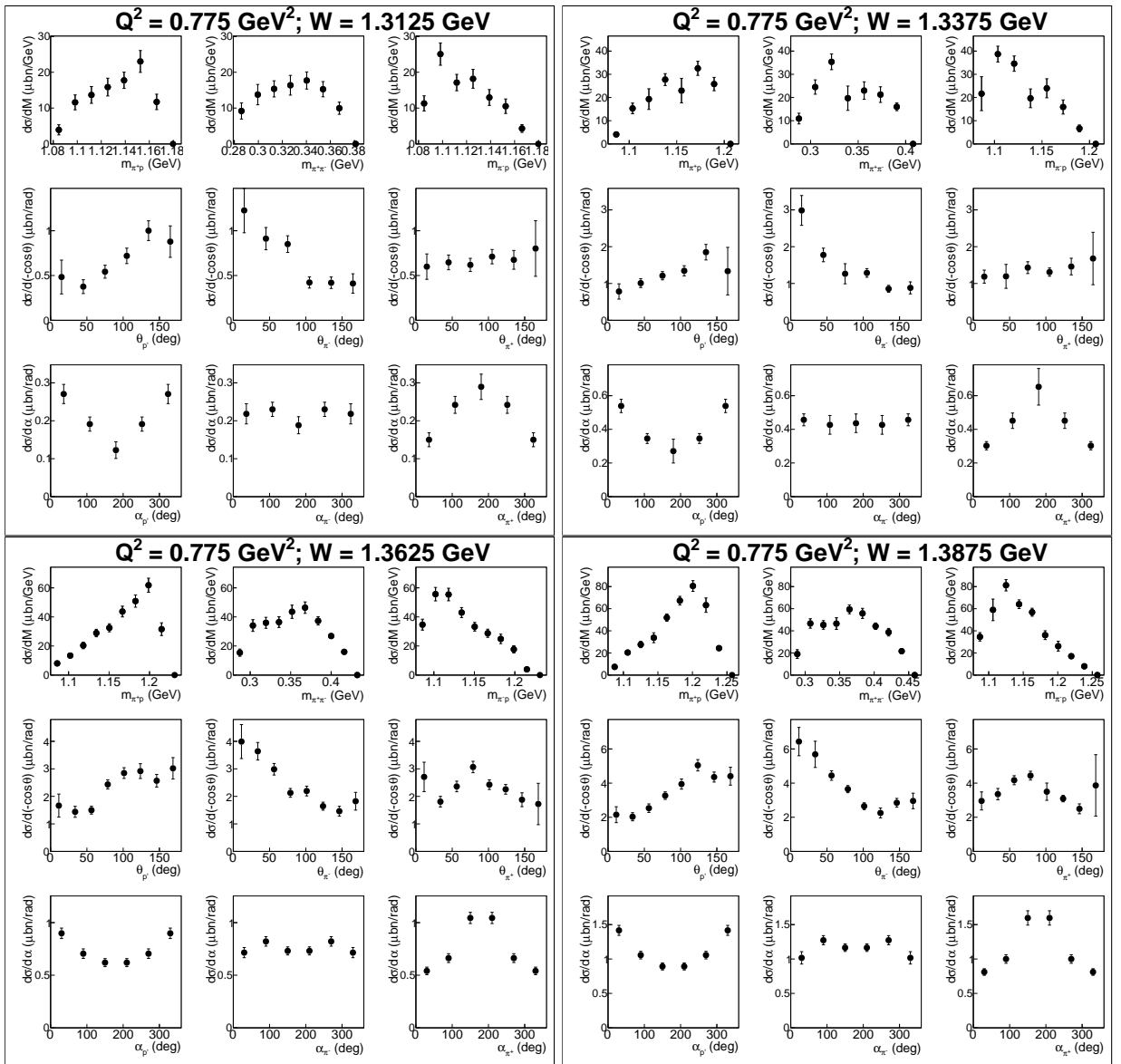


Figure A.32:

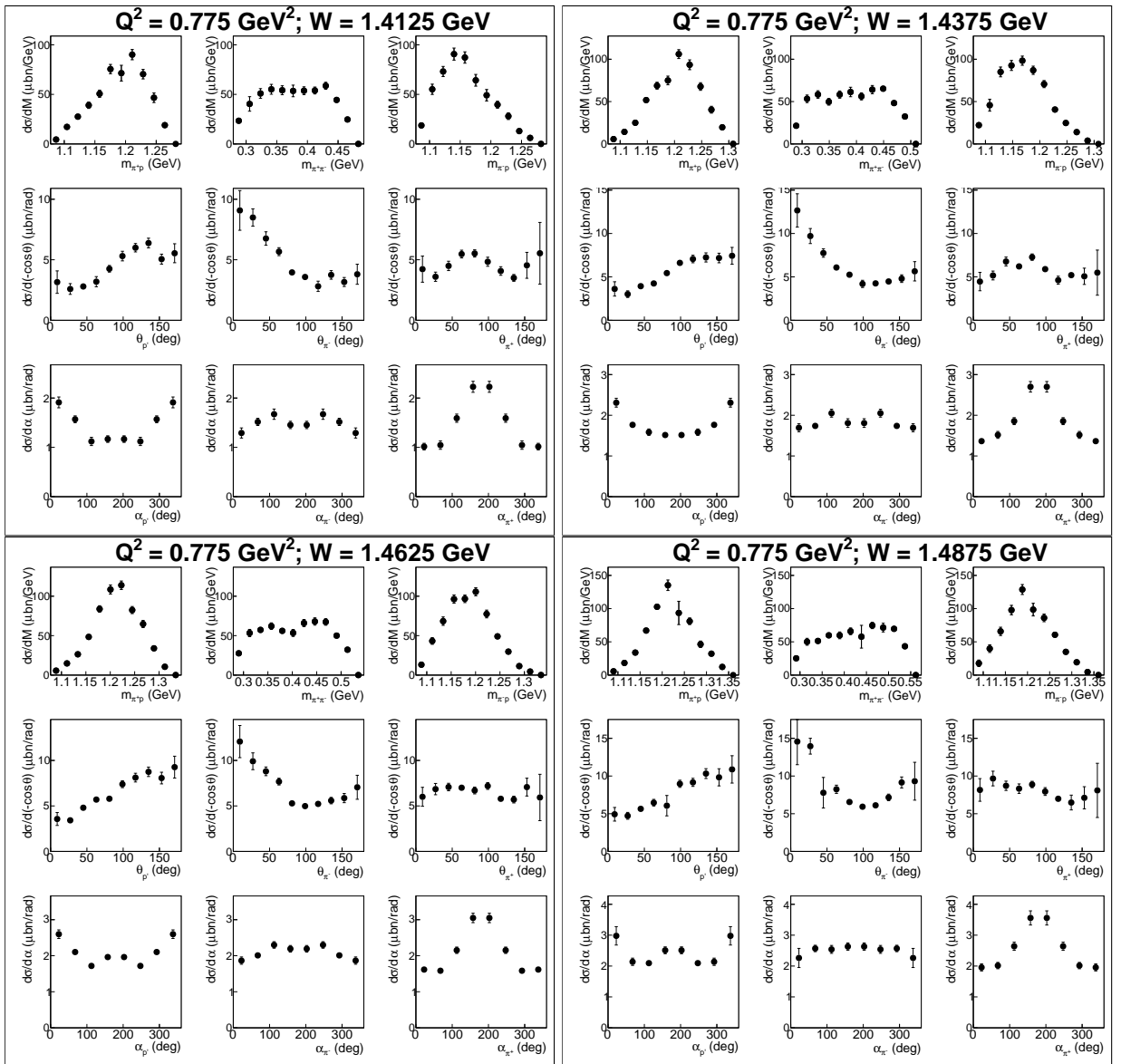


Figure A.33:

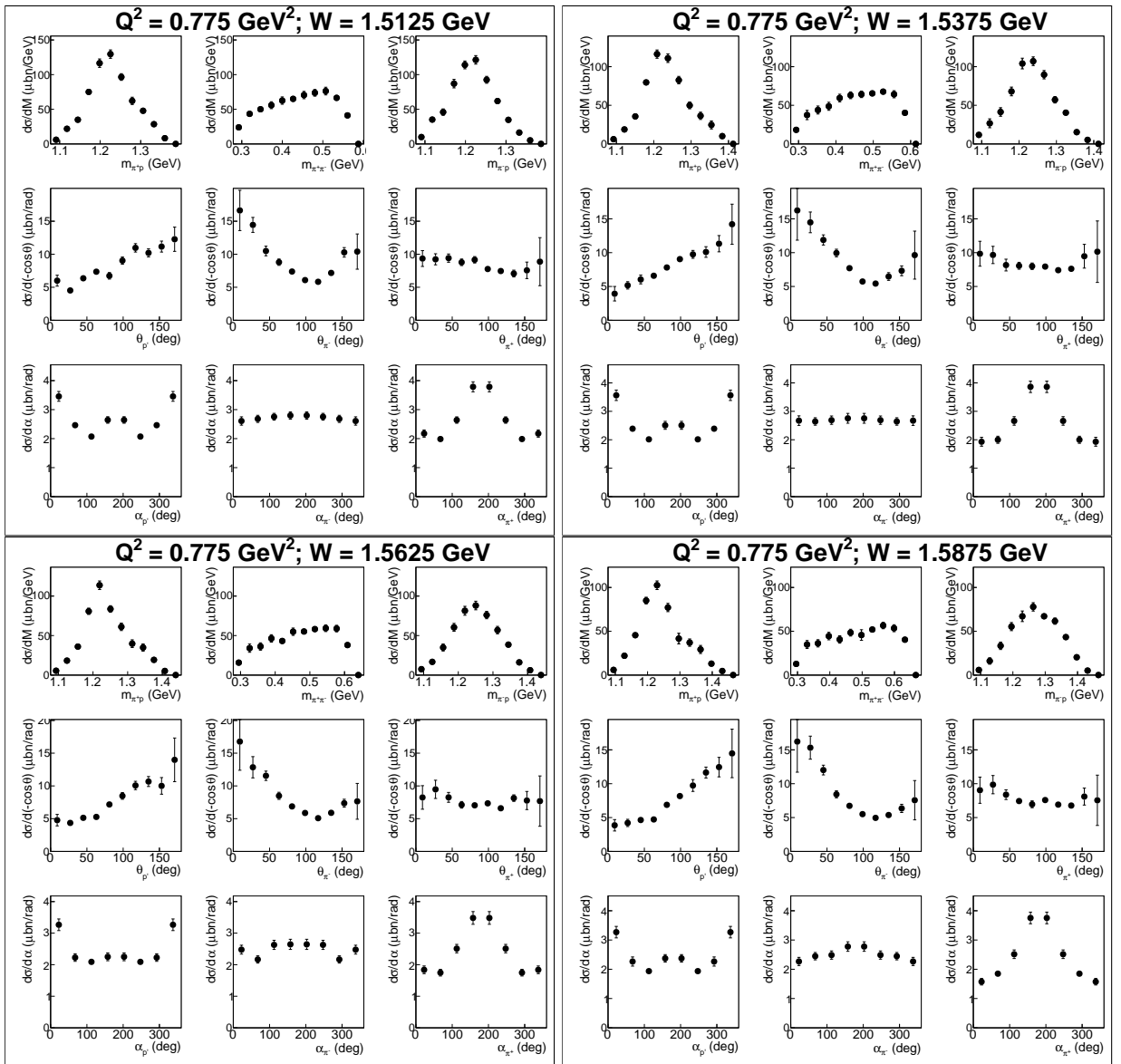


Figure A.34:

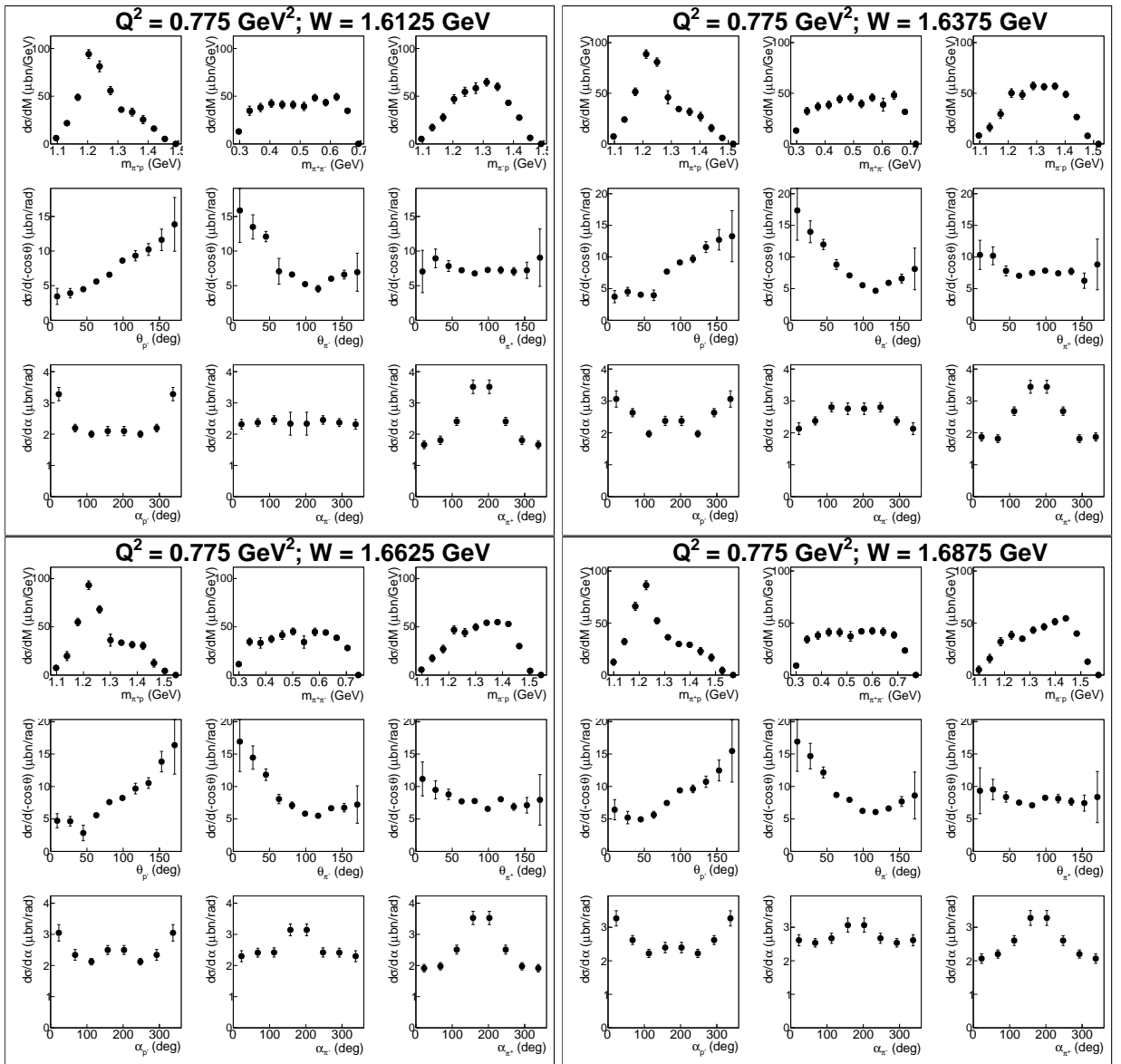


Figure A.35:

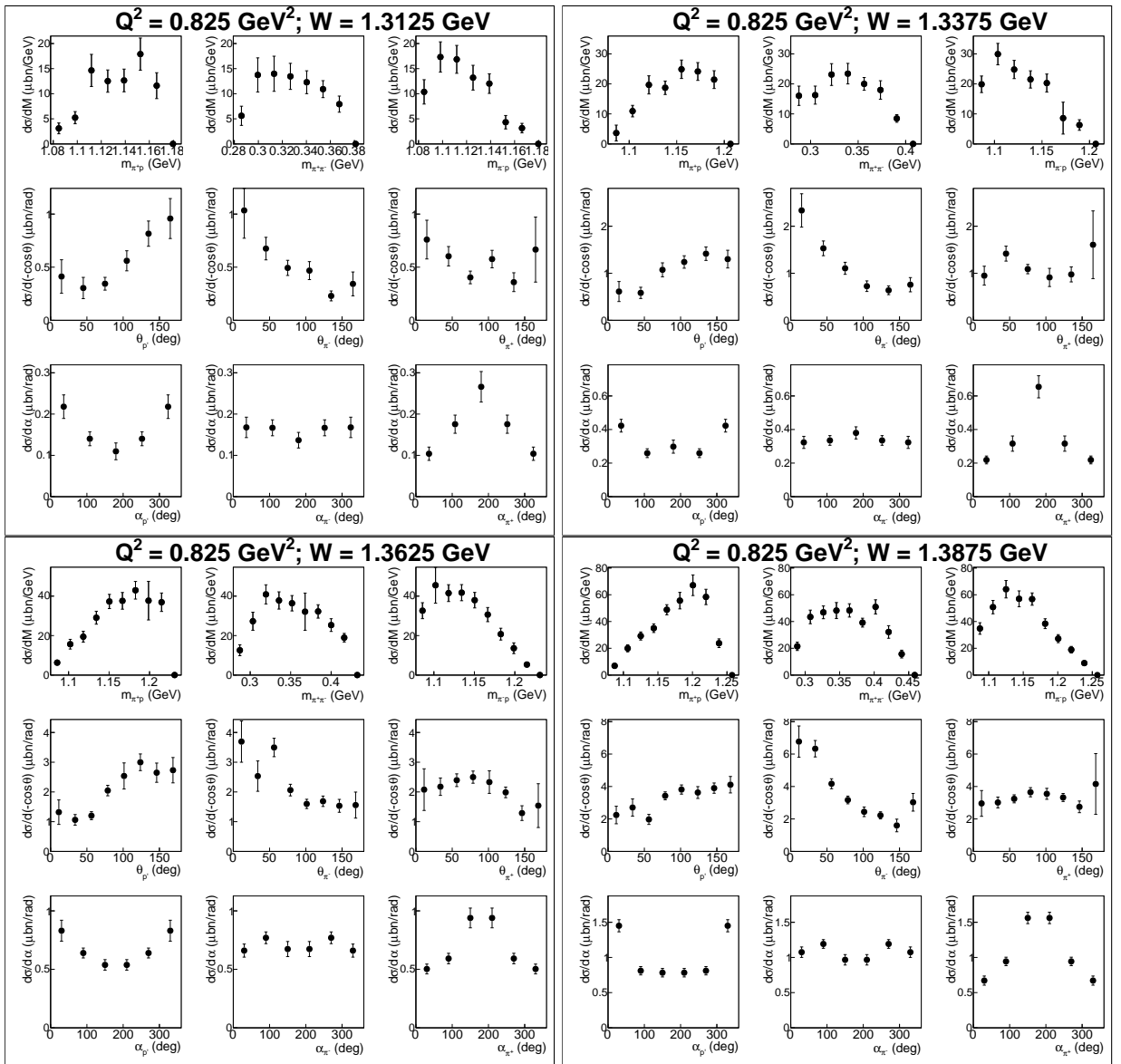


Figure A.36:

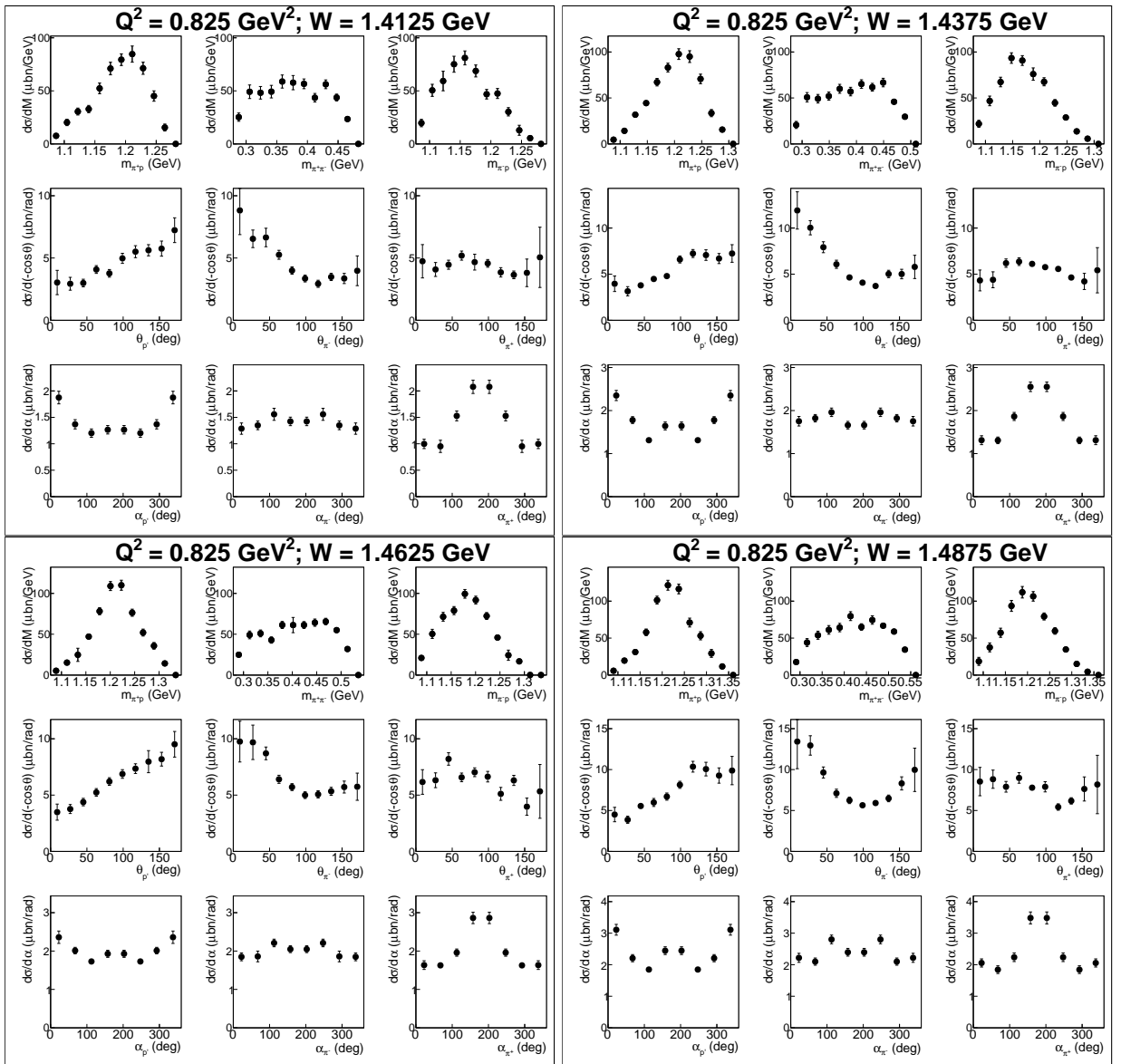


Figure A.37:

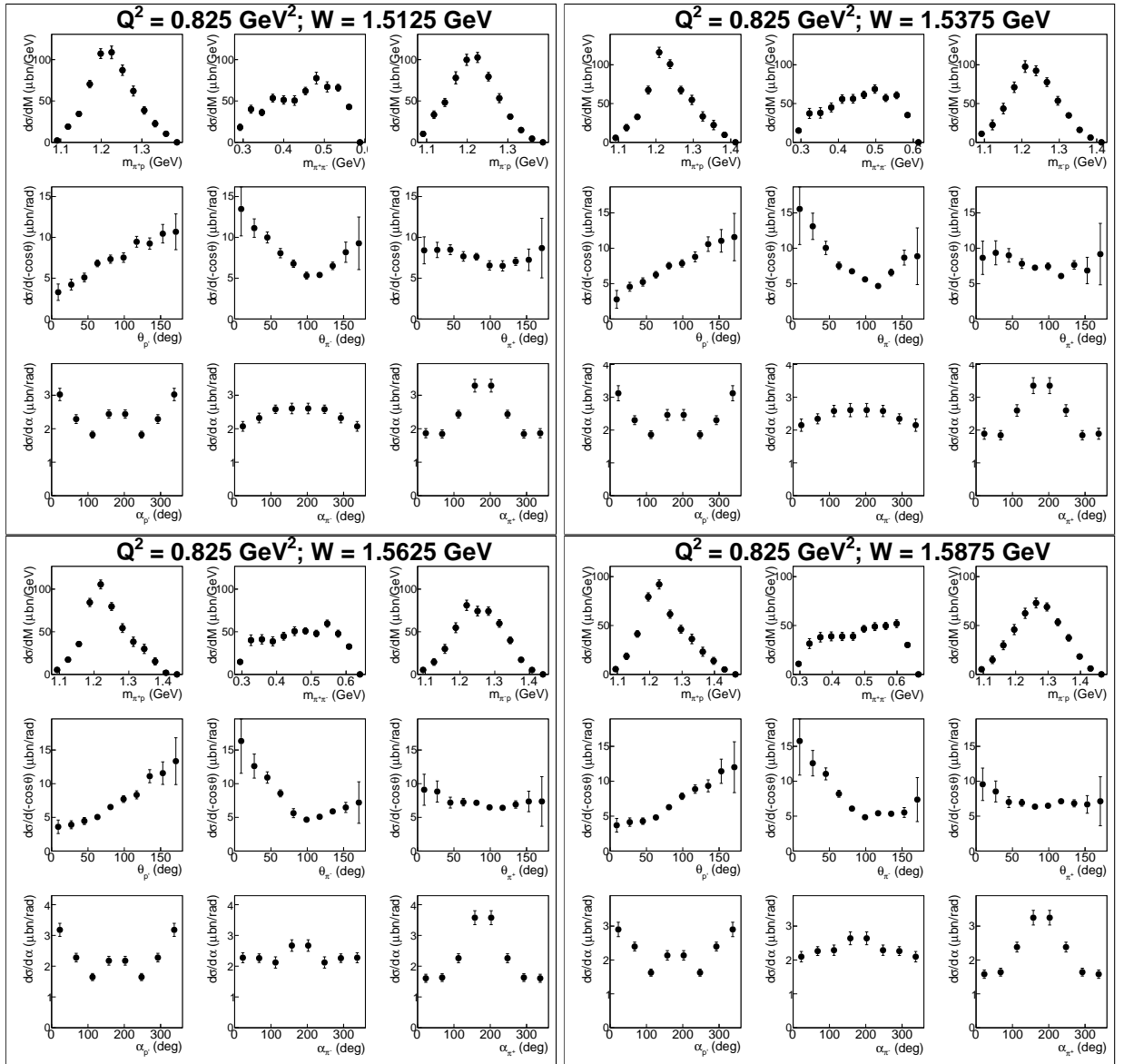


Figure A.38:

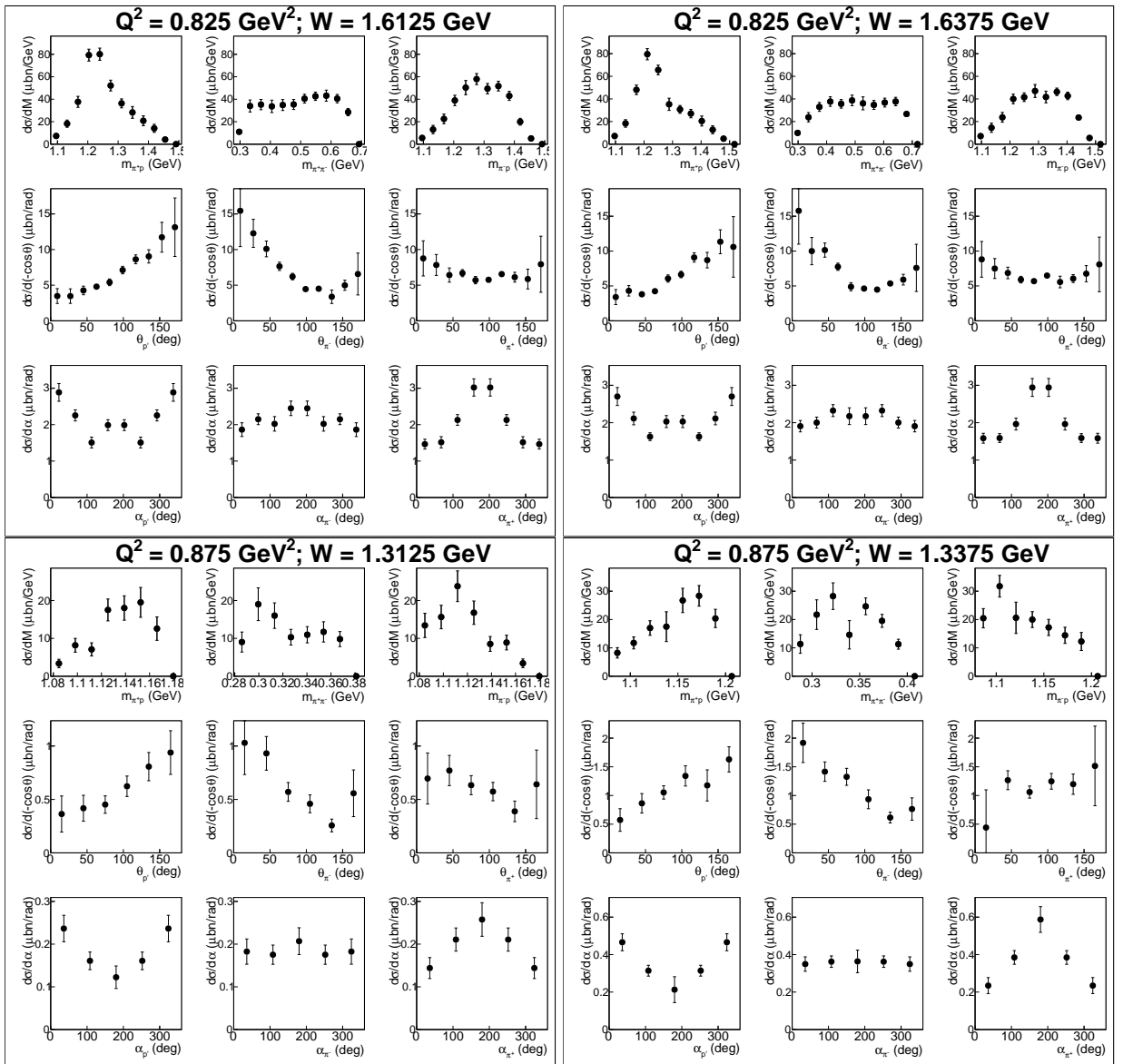


Figure A.39:

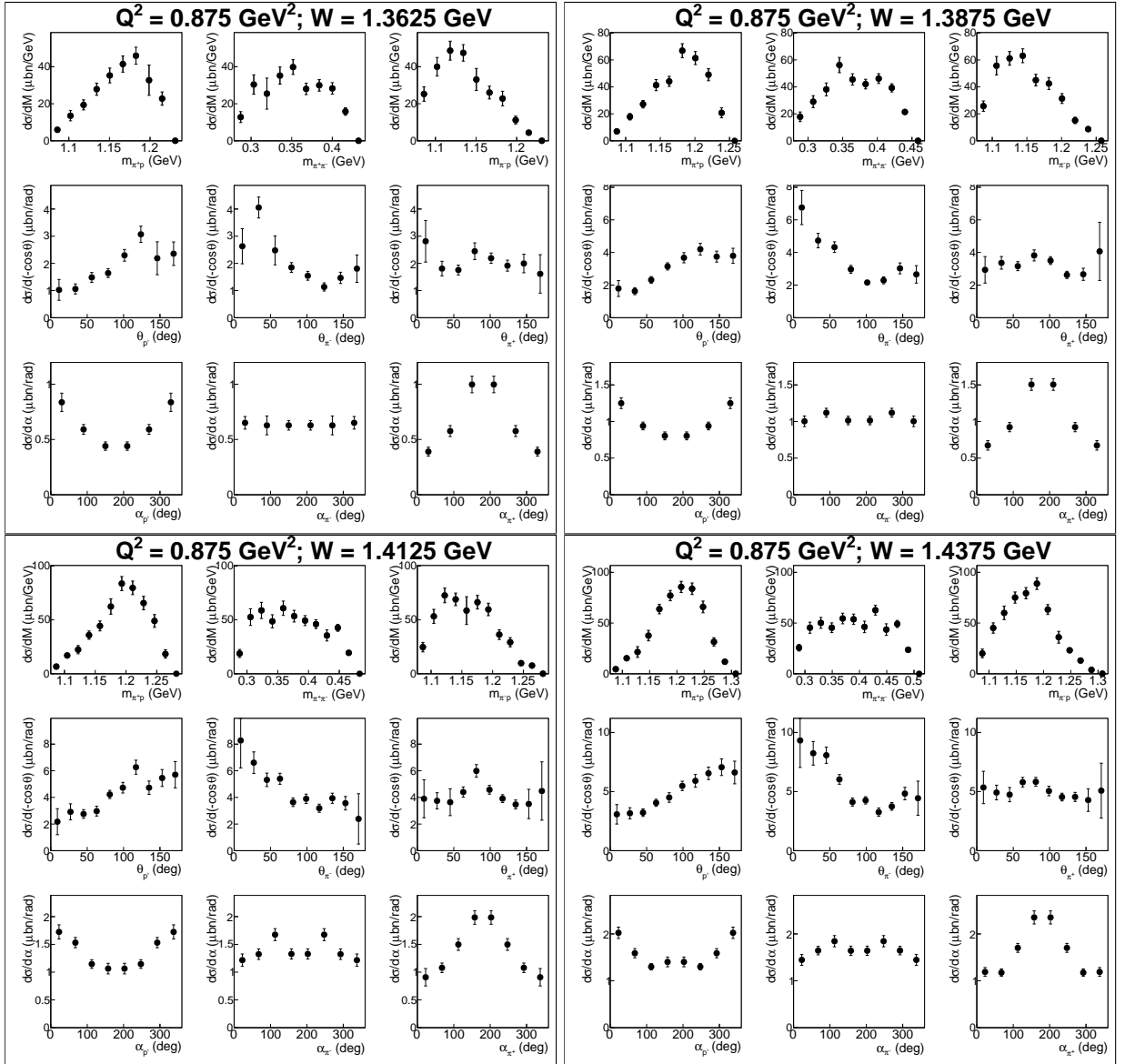


Figure A.40:

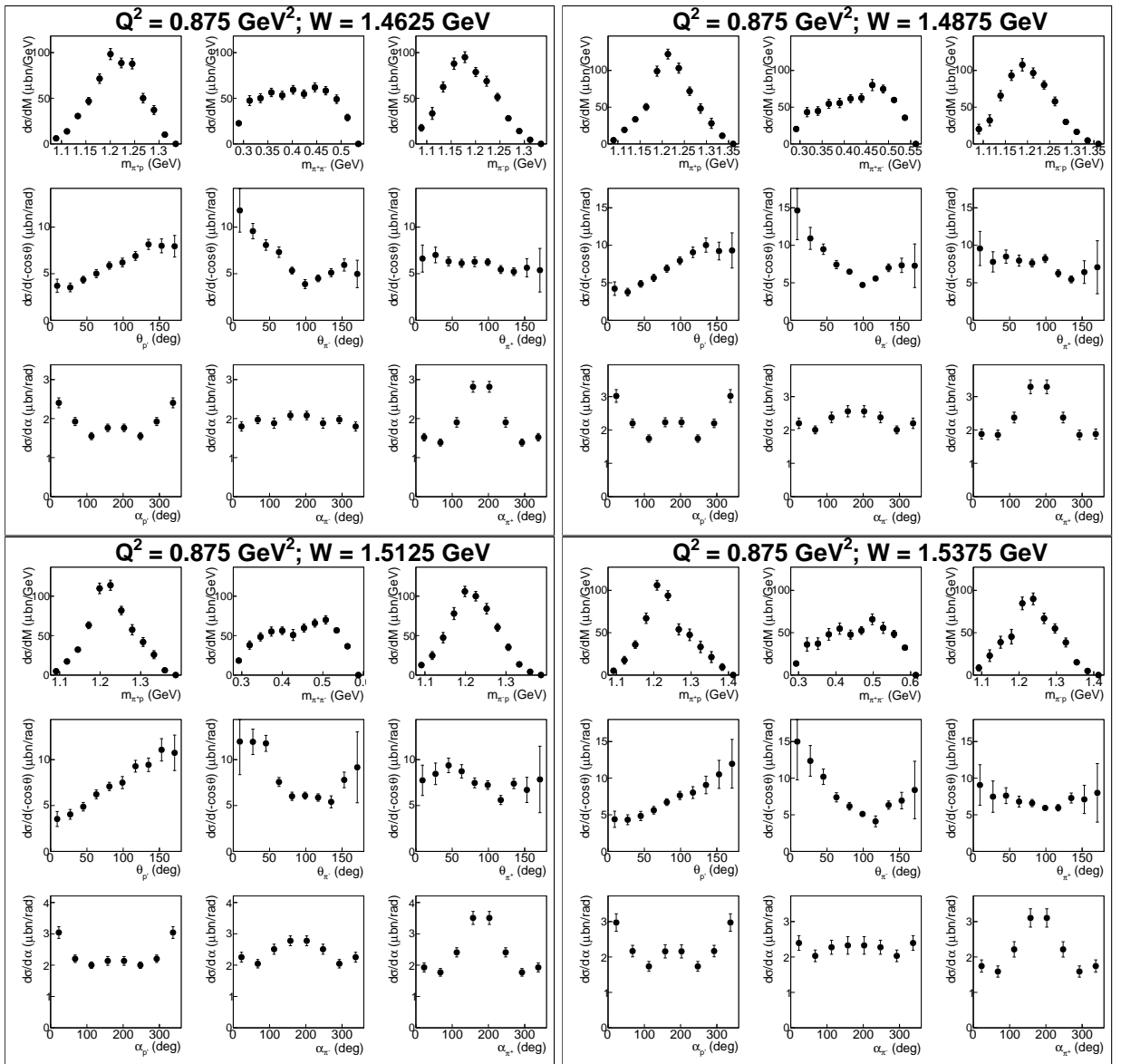


Figure A.41:

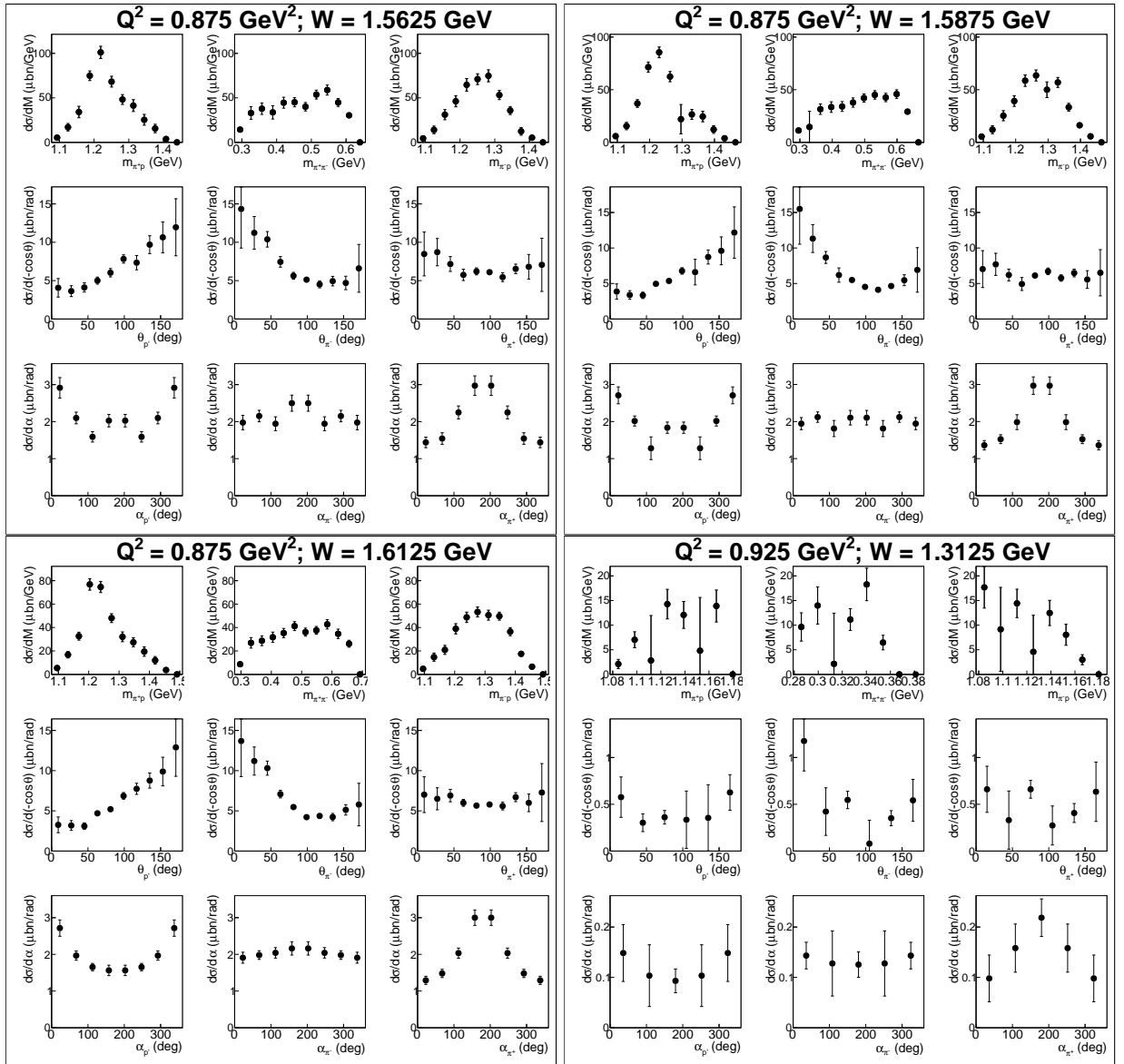


Figure A.42:

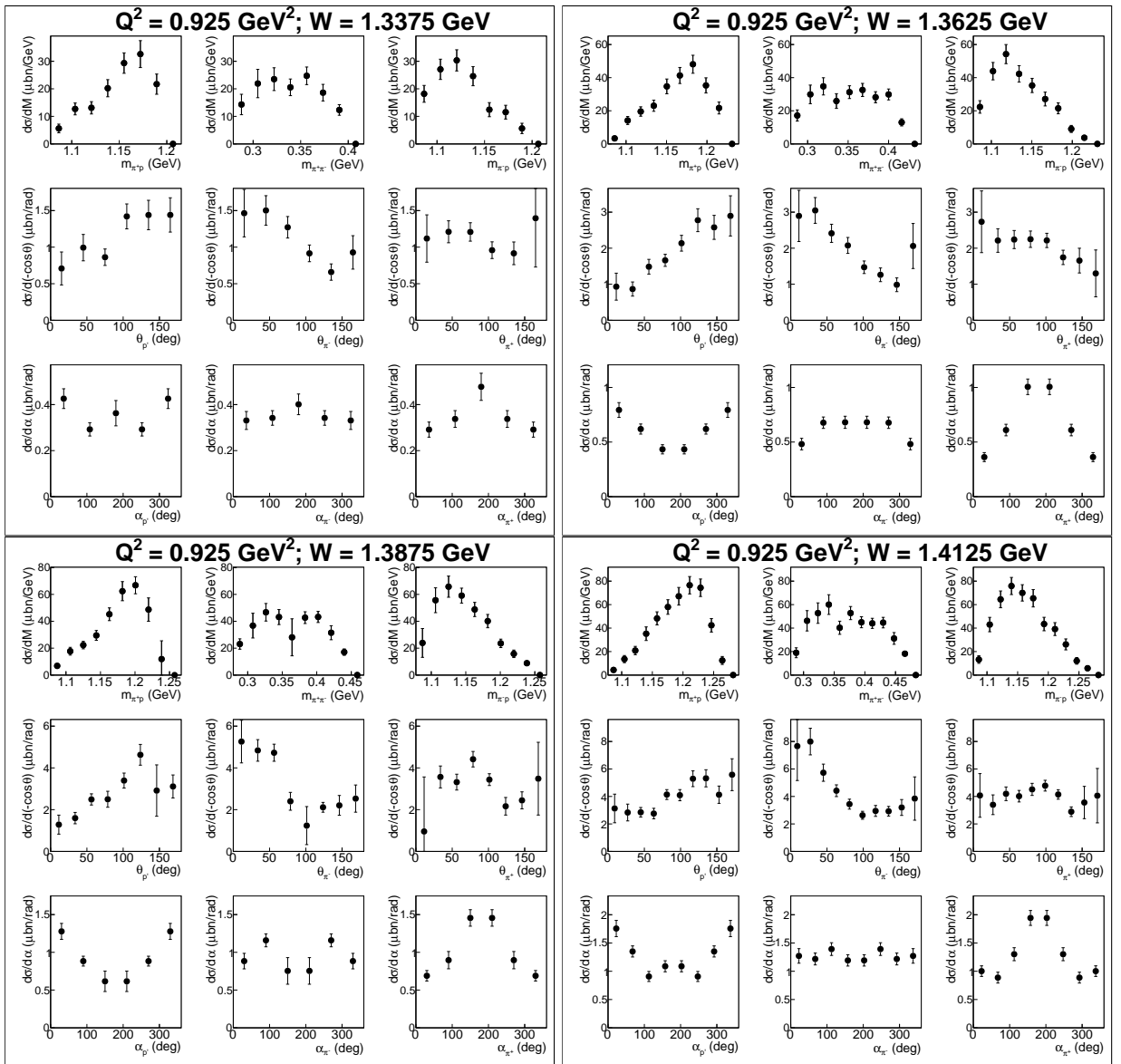


Figure A.43:

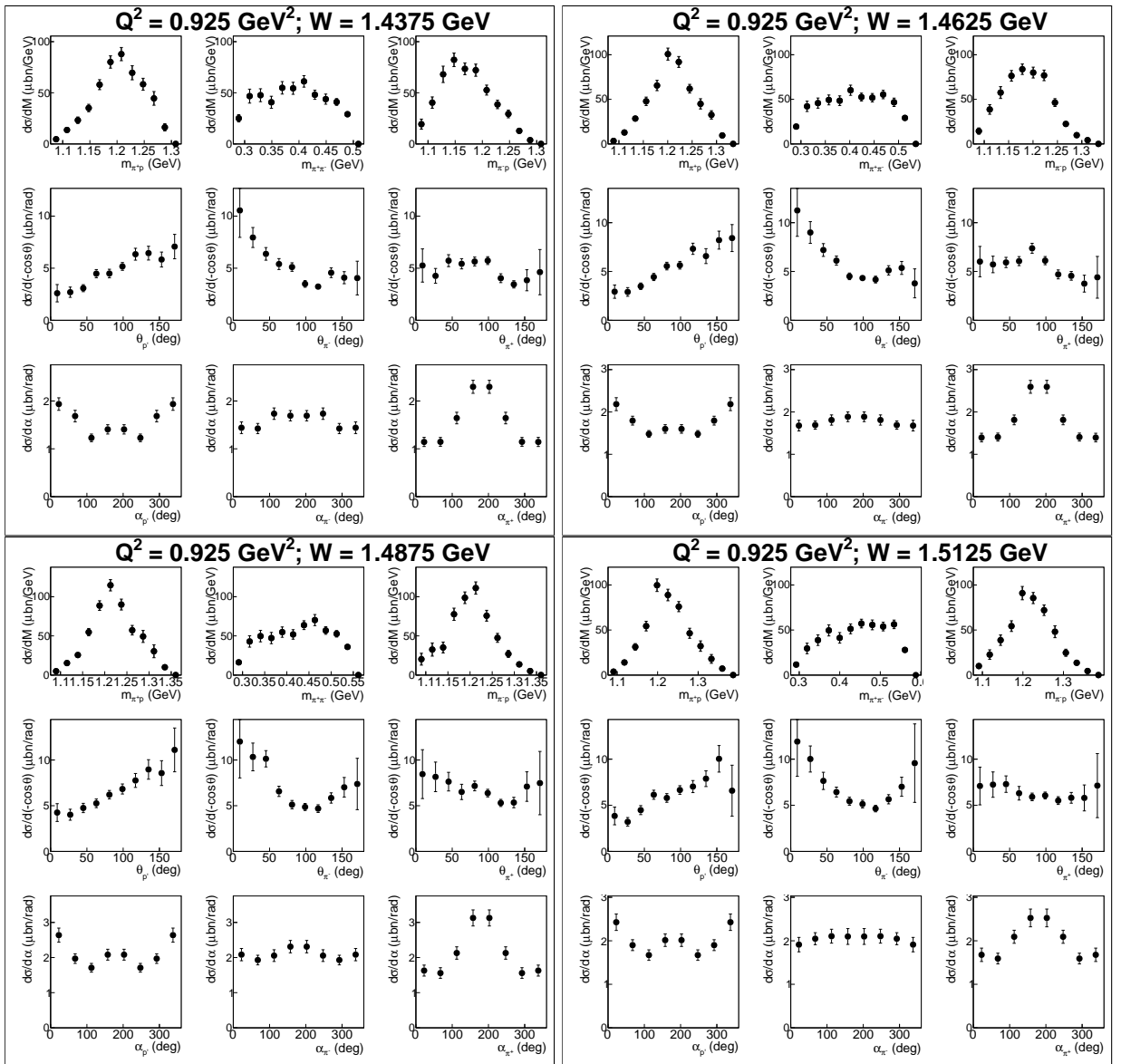


Figure A.44:

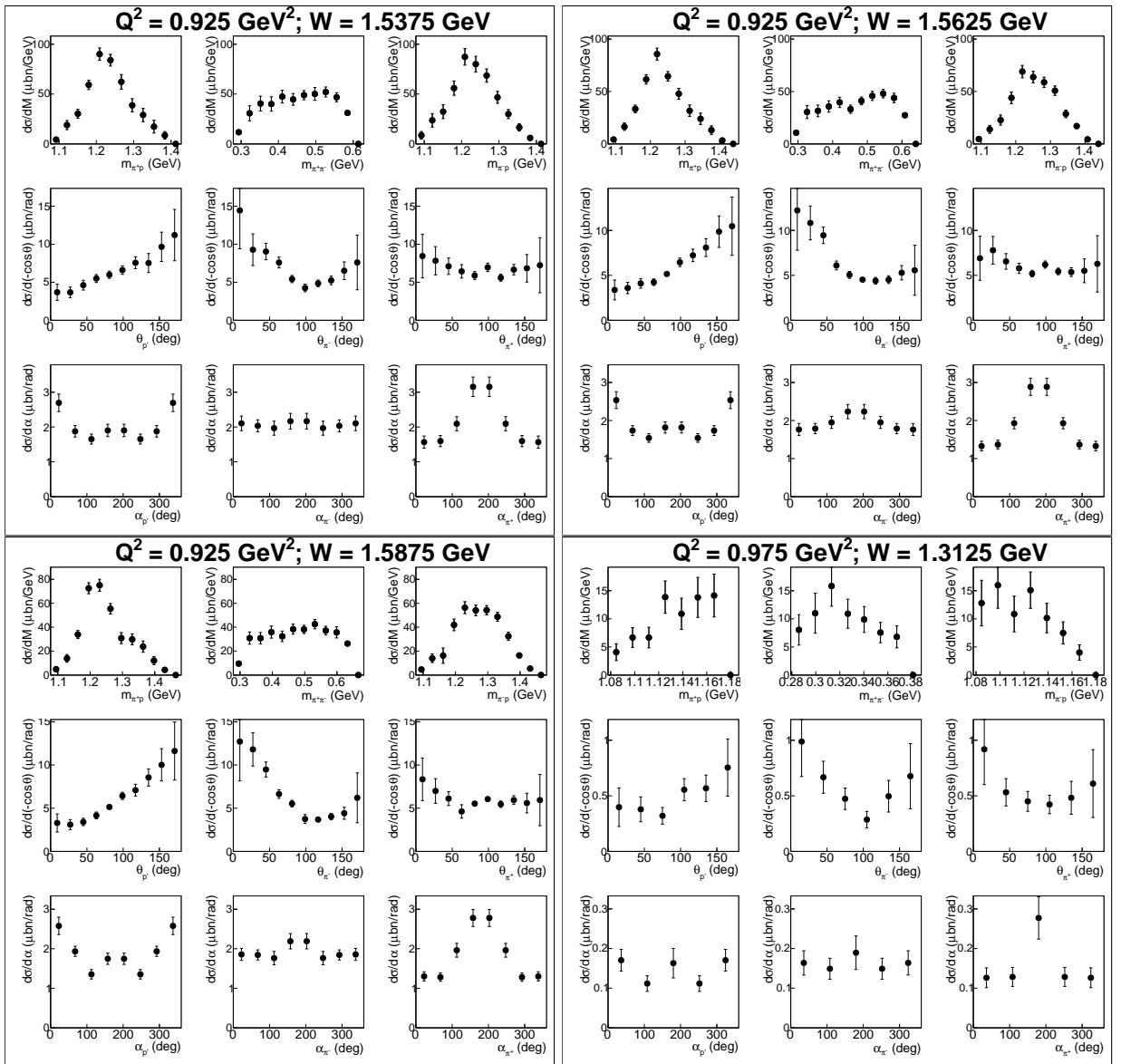


Figure A.45:

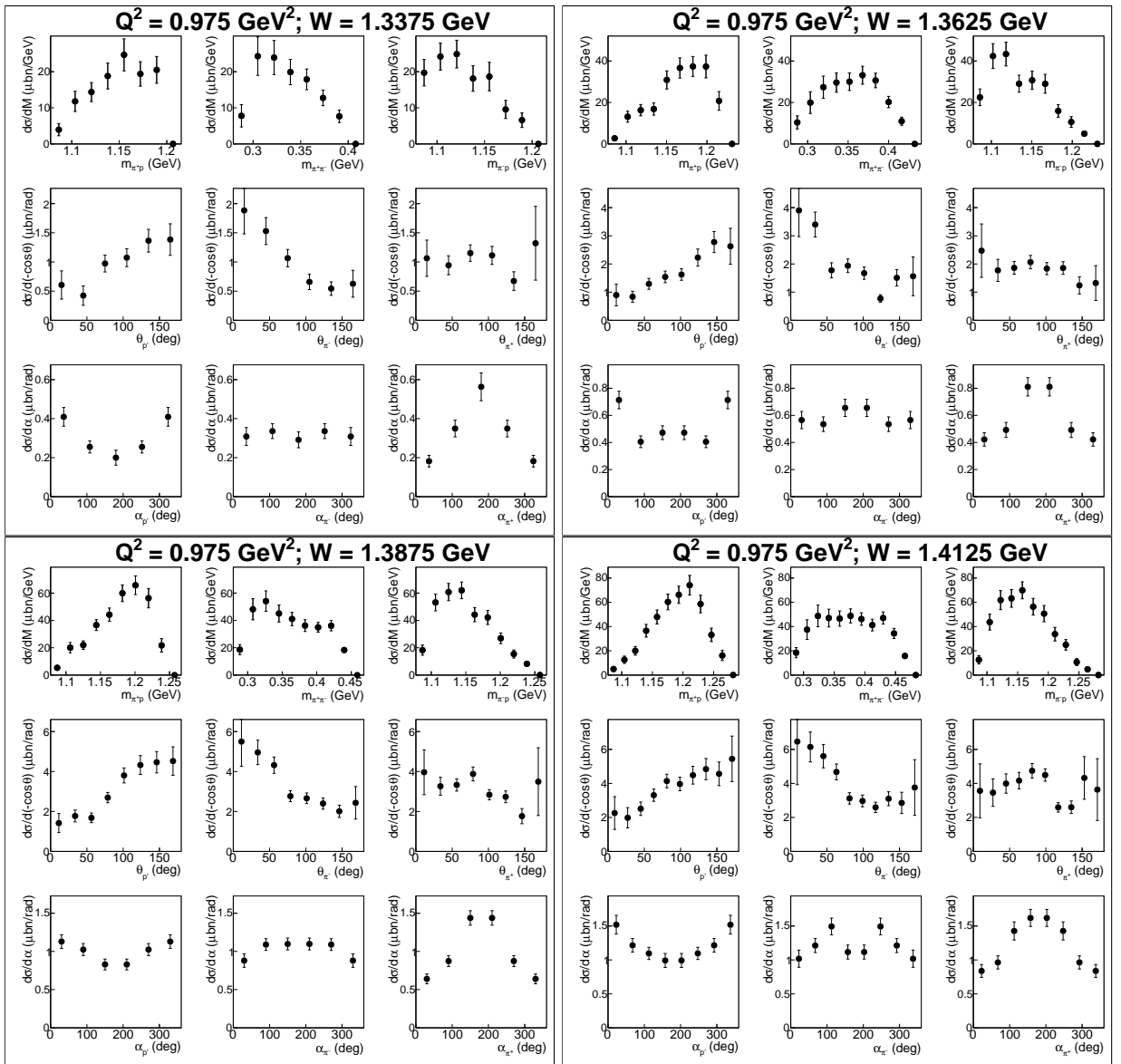


Figure A.46:

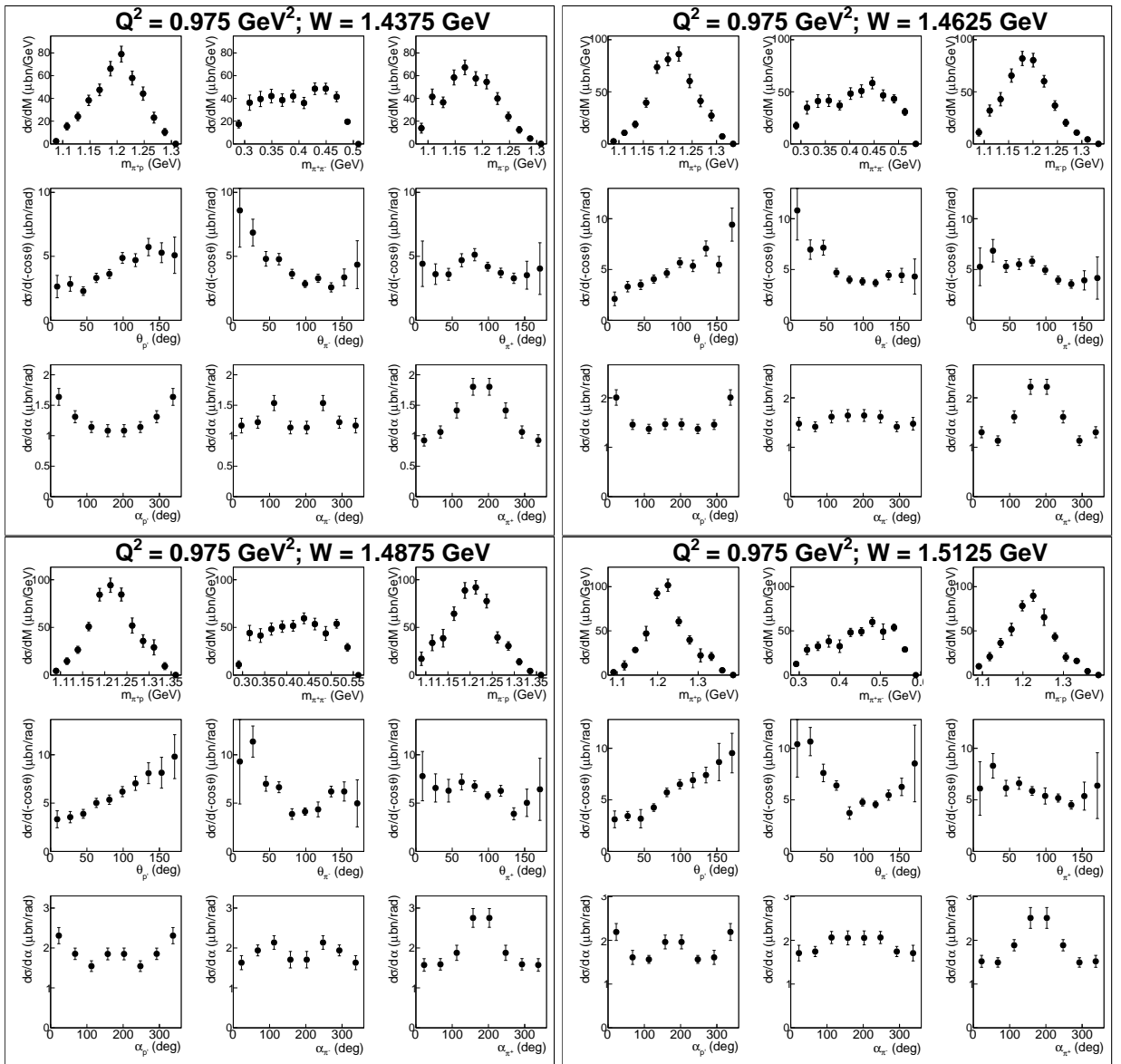


Figure A.47:

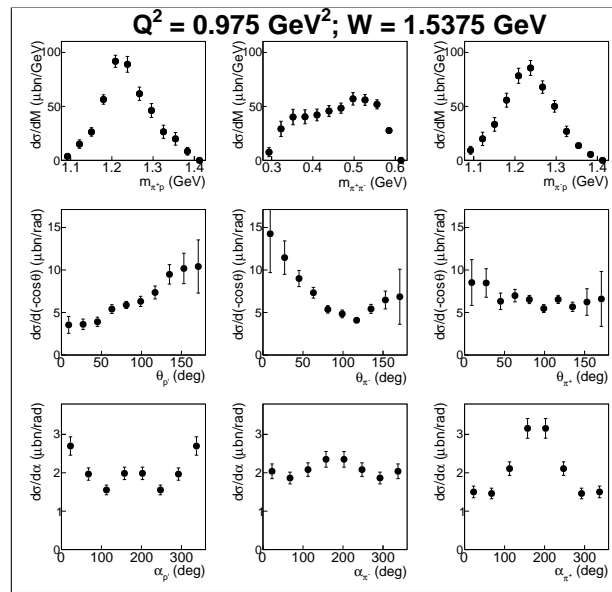


Figure A.48:

# Bibliography

- [1] M. Ripani *et al.*, “Measurement of  $e p \rightarrow e' \pi^+ \pi^-$  and baryon resonance analysis,” *Phys. Rev. Lett.*, vol. 91, p. 022002, 2003.
- [2] I. G. Aznauryan and V. D. Burkert, “Electroexcitation of nucleon resonances,” *Prog. Part. Nucl. Phys.*, vol. 67, pp. 1–54, 2012.
- [3] I. Aznauryan, V. D. Burkert, T. S. H. Lee, and V. I. Mokeev, “Results from the N\* program at JLab,” *J. Phys. Conf. Ser.*, vol. 299, p. 012008, 2011.
- [4] I. G. Aznauryan *et al.*, “Electroexcitation of nucleon resonances from CLAS data on single pion electroproduction,” *Phys. Rev.*, vol. C80, p. 055203, 2009.
- [5] K. Park *et al.*, “Measurements of  $ep \rightarrow e' \pi^+ n$  at  $W = 1.6 - 2.0$  GeV and extraction of nucleon resonance electrocouplings at CLAS,” *Phys. Rev.*, vol. C91, p. 045203, 2015.
- [6] G. V. Fedotov *et al.*, “Electroproduction of  $p \pi^+ \pi^-$  off protons at  $0.2 \leq Q^2 \leq 0.6$ -GeV $^2$  and  $1.3 \leq W \leq 1.57$ -GeV with CLAS,” *Phys. Rev.*, vol. C79, p. 015204, 2009.
- [7] V. I. Mokeev *et al.*, “Experimental Study of the  $P_{11}(1440)$  and  $D_{13}(1520)$  resonances from CLAS data on  $ep \rightarrow e' \pi^+ \pi^- p'$ ,” *Phys. Rev.*, vol. C86, p. 035203, 2012.
- [8] V. I. Mokeev *et al.*, “New Results from the Studies of the  $N(1440)1/2^+$ ,  $N(1520)3/2^-$ , and  $\Delta(1620)1/2^-$  Resonances in Exclusive  $ep \rightarrow e' p' \pi^+ \pi^-$  Electroproduction with the CLAS Detector,” *Phys. Rev.*, vol. C93, no. 2, p. 025206, 2016.

- [9] V. I. Mokeev, V. D. Burkert, T.-S. H. Lee, L. Elouadrhiri, G. V. Fedotov, and B. S. Ishkhanov, “Model Analysis of the p pi+ pi- Electroproduction Reaction on the Proton,” *Phys. Rev.*, vol. C80, p. 045212, 2009.
- [10] V. I. Mokeev and I. G. Aznauryan, “Studies of  $N^*$  structure from the CLAS meson electroproduction data,” *Int. J. Mod. Phys. Conf. Ser.*, vol. 26, p. 1460080, 2014.
- [11] I. V. Anikin, V. M. Braun, and N. Offen, “Electroproduction of the  $N^*(1535)$  nucleon resonance in QCD,” *Phys. Rev.*, vol. D92, no. 1, p. 014018, 2015.
- [12] V. M. Braun, S. Collins, B. Glie, M. Gckeler, A. Schfer, R. W. Schiel, W. Slodner, A. Sternbeck, and P. Wein, “Light-cone Distribution Amplitudes of the Nucleon and Negative Parity Nucleon Resonances from Lattice QCD,” *Phys. Rev.*, vol. D89, p. 094511, 2014.
- [13] J. Segovia, I. C. Cloet, C. D. Roberts, and S. M. Schmidt, “Nucleon and  $\Delta$  elastic and transition form factors,” *Few Body Syst.*, vol. 55, pp. 1185–1222, 2014.
- [14] D. Binosi, L. Chang, J. Papavassiliou, and C. D. Roberts, “Bridging a gap between continuum-QCD and ab initio predictions of hadron observables,” *Phys. Lett.*, vol. B742, pp. 183–188, 2015.
- [15] J. Segovia, B. El-Bennich, E. Rojas, I. C. Cloet, C. D. Roberts, S.-S. Xu, and H.-S. Zong, “Completing the picture of the Roper resonance,” *Phys. Rev. Lett.*, vol. 115, no. 17, p. 171801, 2015.
- [16] I. C. Cloet, C. D. Roberts, and A. W. Thomas, “Revealing dressed-quarks via the proton’s charge distribution,” *Phys. Rev. Lett.*, vol. 111, p. 101803, 2013.
- [17] I. C. Cloet and C. D. Roberts, “Explanation and Prediction of Observables using Continuum Strong QCD,” *Prog. Part. Nucl. Phys.*, vol. 77, pp. 1–69, 2014.

- [18] B. Julia-Diaz, T. S. H. Lee, A. Matsuyama, T. Sato, and L. C. Smith, “Dynamical coupled-channels effects on pion photoproduction,” *Phys. Rev.*, vol. C77, p. 045205, 2008.
- [19] E. Santopinto and M. M. Giannini, “Systematic study of longitudinal and transverse helicity amplitudes in the hypercentral constituent quark model,” *Phys. Rev.*, vol. C86, p. 065202, 2012.
- [20] I. G. Aznauryan and V. D. Burkert, “Extracting meson-baryon contributions to the electroexcitation of the  $N(1675)\frac{5}{2}^-$  nucleon resonance,” *Phys. Rev.*, vol. C92, no. 1, p. 015203, 2015.
- [21] D. S. Carman, “Nucleon Resonance Structure Studies Via Exclusive KY Electroproduction,” 2016.
- [22] V. I. Mokeev, I. Aznauryan, V. Burkert, and R. Gothe, “Recent results on the nucleon resonance spectrum and structure from the CLAS detector,” *EPJ Web Conf.*, vol. 113, p. 01013, 2016.
- [23] <http://clasweb.jlab.org/bos/browsebos.php>.
- [24] K. Egian *et al.*, “Determination of electron energy cut due to the CLAS EC threshoul,” *CLAS-NOTE-99-007*, 1999.
- [25] M. Osipenko, A. Vlassov, and M. Taiuti, “Matching between the electron cndidate track and Cherenkov counter hit,” *CLAS-NOTE-2004-020*, 2004.
- [26] P. K. Khetarpal, “NEAR THRESHOLD NEUTRAL PION ELECTROPRODUCTION AT HIGH MOMENTUM TRANSFERS ,” *Ph. D. Thesis*, 2010.
- [27] K. Park, V. Burkert, L. Elouadrhiri, and W. Kim, “Kinematics Corrections for CLAS,” *CLAS-Note 2003-012*, 2003.

- [28] M. Ripani *et al.*, “A Phenomenological description of  $\pi^-\Delta^{++}$  photoproduction and electroproduction in nucleon resonance region,” *Nucl. Phys.*, vol. A672, pp. 220–248, 2000.
- [29] I. G. Aznauryan, V. D. Burkert, G. V. Fedotov, B. S. Ishkhanov, and V. I. Mokeev, “Electroexcitation of nucleon resonances at  $Q^2 = 0.65$  (GeV/c) $^2$  from a combined analysis of single- and double-pion electroproduction data,” *Phys. Rev.*, vol. C72, p. 045201, 2005.
- [30] V. I. Mokeev, V. D. Burkert, L. Elouadrhiri, A. A. Boluchevsky, G. V. Fedotov, E. L. Isupov, B. S. Ishkhanov, and N. V. Shvedunov, “Phenomenological analysis of the clas data on double charged pion photo and electro-production,” in *Proceedings, 5th International Workshop on Physics of excited nucleons (NSTAR 2005)*, pp. 47–56, 2005.
- [31] L. W. Mo and Y.-S. Tsai, “Radiative Corrections to Elastic and Inelastic e p and mu p Scattering,” *Rev.Mod.Phys.*, vol. 41, pp. 205–235, 1969.
- [32] C. Wu *et al.*, “Photoproduction of  $\rho^0$  mesons and Delta-baryons in the reaction  $\gamma p \rightarrow p\pi^+\pi^-$  at energies up to  $s^{1/2} = 2.6$  GeV,” *Eur. Phys. J.*, vol. A23, pp. 317–344, 2005.
- [33] E. Byckling and K. Kajantie, *Particle Kinematics*. Jyvaskyla, Finland: University of Jyvaskyla, 1971.
- [34] B. Laforge and L. Schoeffel, “Elements of statistical methods in high-energy physics analyses,” *Nucl. Instrum. Meth.*, vol. A394, pp. 115–120, 1997.
- [35] I. Skorodumina and G. Fedotov, “new  $2\pi$  event generator ([https://clasweb.jlab.org/wiki/index.php/NEW\\_2PI\\_EVENT\\_GENERATOR](https://clasweb.jlab.org/wiki/index.php/NEW_2PI_EVENT_GENERATOR)),”
- [36] *PHENOMENOLOGICAL ANALYSIS OF THE CLAS DATA ON DOUBLE CHARGED PION PHOTO AND ELECTRO-PRODUCTION*, 10-15 Oct 2005 2005.
- [37] “Photoproduction of meson and baryon resonances at energies up to 5.8-GeV,” *Phys.Rev.*, vol. 175, pp. 1669–1696, 1968.

- [38] R. Erbe *et al.*, “Multipion and strange-particle photoproduction on protons at energies up to 5.8-GeV,” *Phys. Rev.*, vol. 188, pp. 2060–2077, 1969.
- [39] N. Markov, “Single  $\pi^0$  Electroproduction off the Proton in the Resonance region ([https://www.jlab.org/Hall-B/general/thesis/Markov\\_thesis.pdf](https://www.jlab.org/Hall-B/general/thesis/Markov_thesis.pdf)),” 2012.
- [40] E. Golovach, “Clas g11a experiment. clas analysis note. (under review),”
- [41] E. Isupov, “Double-pion electroproduction from clas e1-6 experiment clas analysis note.,”
- [42] P. E. Bosted, “An Empirical fit to the nucleon electromagnetic form-factors,” *Phys. Rev.*, vol. C51, pp. 409–411, 1995.